A MICROMACHINED MAGNETIC FIELD SENSOR FOR LOW POWER ELECTRONIC COMPASS APPLICATIONS

A Dissertation
Presented to
The Academic Faculty

By

Seungkeun Choi

In Partial Fulfillment
Of the Requirements for the Degree
Doctor of Philosophy in the
School of Electrical and Computer Engineering

Georgia Institute of Technology

May 2007

A MICROMACHINED MAGNETIC FIELD SENSOR FOR LOW POWER ELECTRONIC COMPASS APPLICATIONS

Approved by:

Dr. Mark G. Allen, Advisor
School of Electrical and Computer Engineering
Georgia Institute of Technology

Dr. J. Stevenson Kenney
School of Electrical and Computer Engineering
Georgia Institute of Technology

Dr. Oliver Brand
School of Electrical and Computer Engineering
Georgia Institute of Technology

Dr. Jennifer E. Michaels
School of Electrical and Computer Engineering
Georgia Institute of Technology

Dr. Peter J. Hesketh
School of Mechanical Engineering
Georgia Institute of Technology

Date Approved: April 9, 2007

DEDICATION

This dissertation is dedicated to my family

for their endless encouragement and patience.

ACKNOWLEDGEMENTS

My thanks and appreciation to Dr. Mark G. Allen for persevering with me as my advisor through out the time it took me to complete this research and write the dissertation. I have benefited from his thoughtful guidance and constant encouragement, for which I am extremely grateful. The members of my dissertation committee, Dr. Oliver Brand, Dr. J. Steve Kenney, Dr. Peter J. Hesketh, and Dr. Jeniffer E. Michaels, have generously given their time and expertise to better my work. I thank them for their contribution and their good-natured support.

I am grateful to my colleagues in Microsensors and Microactuators (MSMA) research group who shared their memories and experiences, especially Richard Shafer for his endless help for my research. My thanks must go also to all staff of the Microelectronic Research Center (MIRC), for their assistance.

I must express my thanks to all my friends whom I met here at Georgia Tech, especially Yongkyu Yoon for his encouragement and valuable discussions for my research.

Finally, I wish to express my deepest gratitude to my mother, my sister, brother-in-law, and my brother for their unfailing love and support. I appreciate my parents-in-law, my wife, Wooyoung, and my daughter, Shirin for their endless love and support.

TABLE OF CONTENTS

LIST OF TABLES

LIST OF FIGURES

LIST OF SYMBOLS AND ABBREVIATIONS

α	Static rotational angle
k_l	Linear stiffness coefficient
k_{nl}	Nonlinear stiffness coefficient
θ	Angle difference between external magnetic field and magnetization
φ	Oscillation angle
T_0	Maximum torque
ADC	Analog to Digital Converter
AMR	Anisotropic Magnetorresistance
ASIC	Application-Specific Integrated Circuit
CMOS	Complementary Metal-Oxide Semiconductor
FEM	Finite Element Method
GMR	Giant Magnetoresistance
GPS	Global Positioning Systems
ICP	Inductively Coupled Plasma
MEMS	Microelectromechanical Systems
MR	Magnetoresistive
PCB	Printed Circuit Board
RIE	Reactive-Ion Etching
SEM	Scanning Electron Microscope
SQUID	Superconducting Quantum Interference Device

SUMMARY

A micromachined magnetic field sensing system capable of measuring the direction of the Earth's magnetic field has been fabricated, measured, and characterized. The system is composed of a micromachined silicon resonator combined with a permanent magnet, excitation and sensing coils, and a magnetic feedback loop. Electromagnetic excitation of the mechanical resonator enables it to operate with very low power consumption and low excitation voltage. The interaction between an external magnetic field surrounding the sensor and the permanent magnet generates a rotating torque on the silicon resonator disc, changing the effective stiffness of the beams and therefore the resonant frequency of the sensor. By monitoring shifts of the resonant frequency while changing the orientation of the sensor with respect to the external magnetic field, the direction of the external magnetic field can be determined.

MEMS-based mechanically-resonant sensors, in which the sensor resonant frequency shifts in response to the measurand, are widely utilized. Such sensors are typically operated in their linear resonant regime. However, substantial improvements in resonant sensor performance (functionally defined as change in resonant frequency per unit measurand change) can be obtained by designing the sensors to operate far into their nonlinear regime. This effect is illustrated through the use of a magnetically-torqued, rotationally-resonant MEMS platform. Platform structural parameters such as beam width and number of beams are parametrically varied subject to the constraint of constant small-deflection resonant frequency. Nonlinear performance improvement characterization is performed both analytically as well as with Finite Element Method

(FEM) simulation, and confirmed with measurement results. These nonlinearity based sensitivity enhancement mechanisms are utilized in the device design.

The fabrication is based on a one-mask, single wafer silicon bulk micromachining process. The top side silicon wafer is etched by inductively-coupled-plasma (ICP) to form a movable resonant disc, a recess for a permanent magnet, and support beams. The permanent magnet is adhered to the center of the moving disc. The excitation and sensing coils and associated electronics are hybrid-assembled with the sensor. Micromachining fabrication technology enables the beam width of the mechanical resonator structure to have a very high aspect ratio of approximately 10:1. Furthermore, complementary metal-oxide-semiconductor (CMOS) compatibility is another advantage of the bulk silicon micromachining.

The complete magnetic sensing system consumes less than 200 microwatts of power in continuous operation, and is capable of sensing the direction of the Earth's magnetic field. Such low power consumption levels enable continuous magnetic field sensing for portable electronics and potentially wristwatch applications, thereby enabling personal navigation and motion sensing functionalities. A total system power consumption of 138 μW and a resonator actuation voltage of 4mVpp from the ±1.2V power supply have been demonstrated with capability of measuring the direction of the Earth's magnetic field. Sensitivities of 0.009, 0.086, and 0.196 [mHz/(Hz·degree)] for the Earth's magnetic field were measured for 3, 4, and 6 beam structures, respectively

CHAPTER 1

INTRODUCTION

There have been increasing demands for integration of a magnetic field sensor which can detect the direction of the Earth's magnetic field into complex electronic systems. Such an electronic compass system will find application in ultra low power mobile devices such as wristwatches and portable Global Positioning Systems (GPS). The objective of this research is to develop a small size, low power consumption, and low operation voltage magnetic field sensor that can detect the direction of the Earth's magnetic field. In this chapter, the research overview and motivations are presented.

1.1 Compass overview

The first magnetic device ever used is the magnetic compass, which provides an easy and inexpensive way to determine direction relative to the Earth's magnetic poles. It is one of the oldest navigation instruments and is still widely used by ship captains, pilots, and hikers. The simplest compass is nothing more than a magnetized needle supported by a low friction pivot that allows it to freely rotate upon interaction with an external magnetic field. In many applications, electronic devices are now replacing the magnetized needle type compass since it is not readily adaptable to digital output or interfacing with other electronic components and hence is difficult to integrate into more complex electronic systems.

1.2 Motivation and requirements for today's compass

A Global Position System (GPS) has been operated by the U.S Department of Defense (DoD) since the early 1970s. Initially, this system was targeted mainly for military purposes to track precise position information of military movements around the world. To meet this demand, the 24 satellites orbiting the globe transmit microwave signals continuously. A receiver can calculate precisely its time, three-dimensional position, and velocity of movement by receiving GPS signals from at least four different satellites simultaneously. Since 1991 an agreement between the DoD and the International Civil Aviation Organization has made it possible for the civilian community to use the GPS without any direct user charge.

Mobile devices tend to provide multi-functionality. A cell phone, for example, can provide several different functions such as making a phone call, sending and receiving an e-mail, taking a digital picture, and listening to digital music. Furthermore, cell phones will soon be equipped with GPS systems since the Federal Communications Commission (FCC) required last year that cellular companies equip all new cell phones with GPS tracking devices that can pinpoint a user's location within 300 feet. This new functionality of cell phones will enable law enforcement agencies to determine the origination of 911 emergency calls made on cell phones. However, people want the GPS system to provide not only the information of the location of a 911 call, but also the information for navigation. A GPS receiver can provide accurate information about its position and velocity, and from the velocity vector it can determine the direction in which it is moving. The direction of movement is not necessarily the same as the heading or direction in which the GPS receiver is pointing. A single-antenna GPS receiver cannot

determine heading, but a compass can. When GPS signals are not strong enough, a GPS-based navigation system might have to resort to dead reckoning. GPS systems with a built-in electronic compass will be a good solution for this kind of problem. In Japan, close to eight million cell phones, mostly from KDDI Corporation of Japan, offer users GPS functionality. The "KDDI au" handset with GPS functionality uses "Mobile Station Modem" (MSM) series chips from Qualcomm Inc. Qualcomm later acquired SnapTrack in 2000, which provides the main technology for navigation functionality on cellular phones. When the position is to be determined, a remote server, called the position determination entity (PDE) server, needs to receive the GPS information from the handset and returns the calculated position information to the handset so that the map data is displayed. It takes about 50 seconds to display the map data on the screen. Many users are dissatisfied with such a long waiting time. To resolve this issue, a new method, called the mobile station (MS) based approach, has been developed. The initial measurement is the same, but the subsequent measurement is completed by the handset alone, reducing the time required to display the map to only 1-3 seconds. Measurement time is shortened and users need to pay a communication charge for the initial measurement only. The handset with a built-in electronic compass with GPS functionality enabled this approach. The A5501T, A5502K, and A5503SA models supporting this service have been sold since December 2003 in Japan. The electronic compass will be invaluable in cases where people don't know where they are going even though the navigation software displays a map. LG Electronics of Korea released a new cell phone last year, called "Qiblah," for Islamic users in the Middle East. An electronic compass points toward Mecca when users input their location. Such phones enable Muslims to

more easily locate the direction of Mecca, which they must face during their daily prayers. Cellular phones are becoming increasingly sophisticated, with a variety of functions that result in high power consumption. However, phone size is getting smaller. Therefore, a single component in a handset device should be compact, and consume low power; these constraints extend to an electronic compass. A conventional wristwatch can be combined with a magnetic sensor to provide time information and direction information. The Suunto M9 Wristwatch incorporates watch, barometer, thermometer, altimeter, 3D compass and GPS altogether (see Figure 1.1 (a)). Another example is the Casio (PAG50-1V) Pathfinder Triple Sensor Tough Solar Watch (see Figure 1.1 (b)). It measures and displays direction as one of 16 points. Measuring range is 0° to 359° and measuring unit is 1°.

(a) Suunto M9 Wristwatch w/ GPS (b) Casio (PAG50) Pathfinder solar watch

Figure 1. 1. Wrist watches that provide directions.

For mobile electronic applications, there are several requirements for the magnetic field sensor along with sensitivity sufficient to measure the direction of the Earth's magnetic field: 1) low power consumption, 2) small size, 3) low operational voltage, and 4) CMOS compatible fabrication. Recent advances in the manufacturing process, a micromachining process, enable such a sensor to be built in a micro size with CMOS compatible processes. The potential for mass production is also one of the advantages of the micromachining process. The sensor needs to be built on the substrate whose mechanical and electrical properties are not changed over long period of time to avoid performance degradation.

1.3 Contributions and research overview

A micromachined magnetic field sensing system capable of measuring the direction of the Earth's magnetic field has been fabricated, measured, and characterized. The system is composed of a micromachined silicon resonator combined with a permanent magnet, excitation and sensing coils, and a magnetic feedback loop for the completion of the system. The fabricated resonant magnetic sensor demonstrated a capability of measuring the Earth's magnetic field with ultra-low power consumption and low voltage operation. A CMOS compatible fabrication process makes it suitable for further integration with other electronic components. External electronic circuitry provides a magnetic feedback loop such that the resonator always oscillates at its resonant frequency. It is also observed that sensitivity of the fabricated resonant magnetic sensor can be increased by maximizing nonlinearity. The overview of the research is shown in Figure 1.2.

A theoretical model has been developed to provide an analytical tool for understanding and predicting of the behavior of the mechanical resonator. It has been observed through the modeling that the nonlinearity needs to be maximized for the maximum sensitivity. Geometry parameters such as beam width and the number of beams are adjusted to produce best performance in terms of sensitivity subject to fabrication constraints, for example device thickness and aspect ratio. It suggests that the beam width should be narrow while the number of beams should be increased for a given resonant frequency. The results of the theoretical modeling are verified with Finite Element Method (FEM) simulation using ANSYS.

Based on the results of the modeling and simulations, mechanical resonators were fabricated and tested with combinations of different beam widths and numbers of beams. Two resonator actuation schemes were considered: electrostatic and magnetic. The resonator was driven electrostatically using an approximately 20 μm pitch comb drive and exhibited very low power consumption. A wafer fusion bonding process was used to provide an electrical isolation between exciting and detecting ports. To achieve low voltage drive, an all magnetic operation system has been implemented in which the mechanical resonator is excited and sensed electromagnetically through coils.

A complete magnetic sensing system consumes less than 200 microwatts of power in continuous operation, and is capable of sensing the Earth's magnetic field. Such low power consumption levels enable continuous magnetic field sensing for portable electronics and potentially wristwatch applications, thereby enabling personal navigation and motion sensing functionalities. A total system power consumption of 138 μW and a resonator actuation voltage of 4mVpp from the ±1.2V power supply have been

demonstrated with capability of measuring the direction of the Earth's magnetic field. Both three and four beam structures show higher performance as the beam width decreases. When the structures have the same linear stiffness coefficient, the structure with narrow beam width and more beams showed higher normalized performance than one with wider beam width and less beams at all the measured external magnetic fields, demonstrating the beneficial effects of nonlinear maximization.

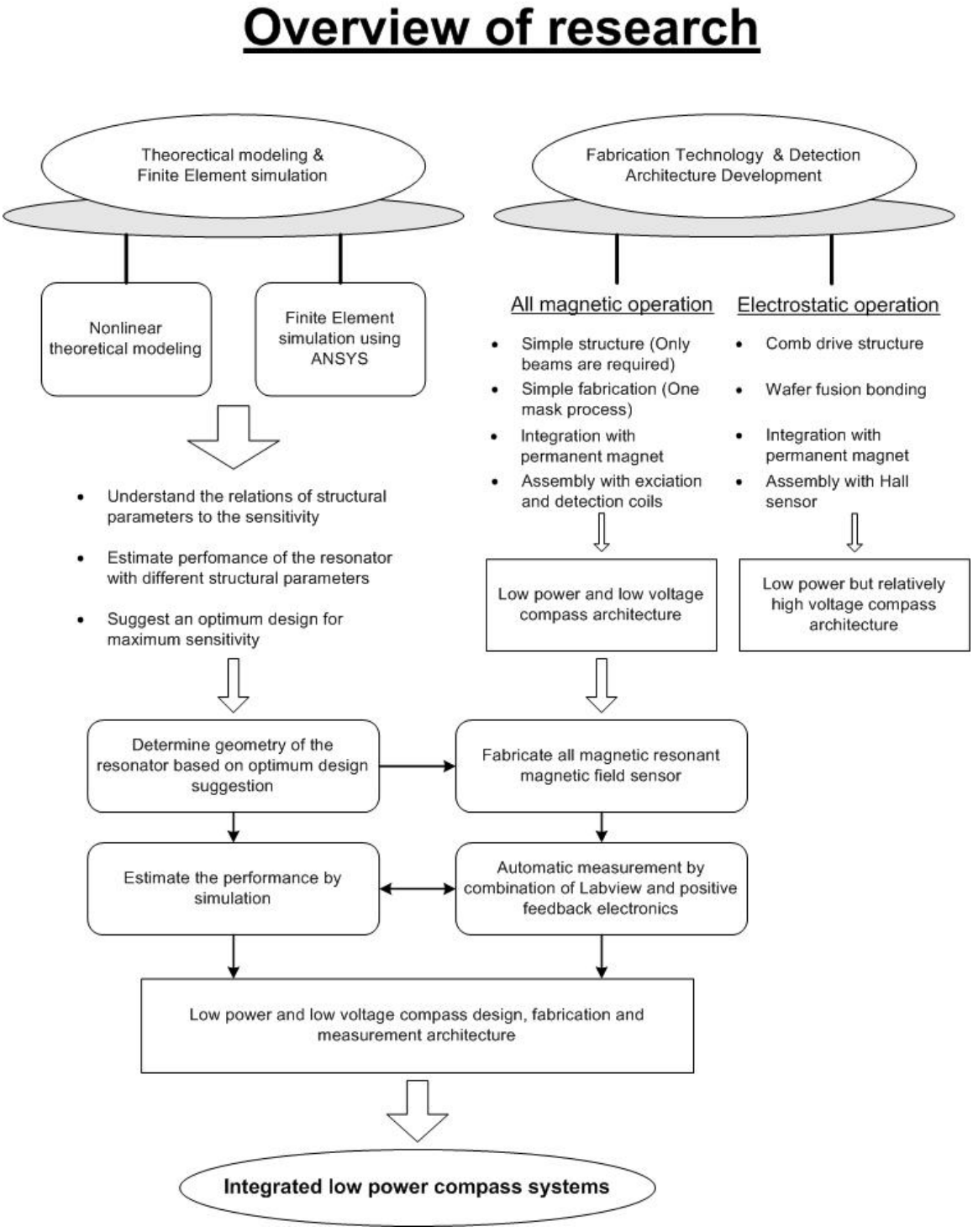

Figure 1. 2. Overview of research.

1.4 Outline of thesis

Research motivation and overviews are given in the first chapter. Because of the larger number of magnetic field measurement principles and techniques an overview of this area is presented in the second chapter. Theoretical modeling and FEM simulation is presented in the third chapter. Fabrication and measurement results are discussed in the fourth chapter. A complete system with electronic circuit is presented in the fifth chapter. Conclusions are given in the sixth chapter.

CHAPTER 2

REVIEW OF MAGNETIC FIELD SENSORS

Because of increasing demands on the integration of the magnetic field sensor with mobile electronic devices, such as a wristwatch and navigator, there have been extensive efforts to reduce power consumption, physical size, and manufacturing cost of magnetic sensors without degrading sensitivity. Thanks to the recent advanced MEMS technology, many sensors now can be fabricated in a small size with improved performance. This leads to the development of a micromachined resonant type magnetic sensor which can provide low power consumption, medium sensitivity, and small size adequate to the integration with other electronic components. In this chapter, magnetic field sensors are reviewed in terms of their sensitivity, power consumption, and physical size. The concept of the presented resonant magnetic sensor is given at the end of the chapter.

2.1 Overview of magnetic field sensors

The magnetic sensor is considered a transducer that converts a magnetic field into an electrical signal. Fifteen different categories of magnetic sensors are listed in Figure 2.1, which compares approximate sensitivity ranges [1, 2]. The sensitivity range for each concept highly depends on the readout electronics along with frequency response, physical size, and power applied to the sensors.

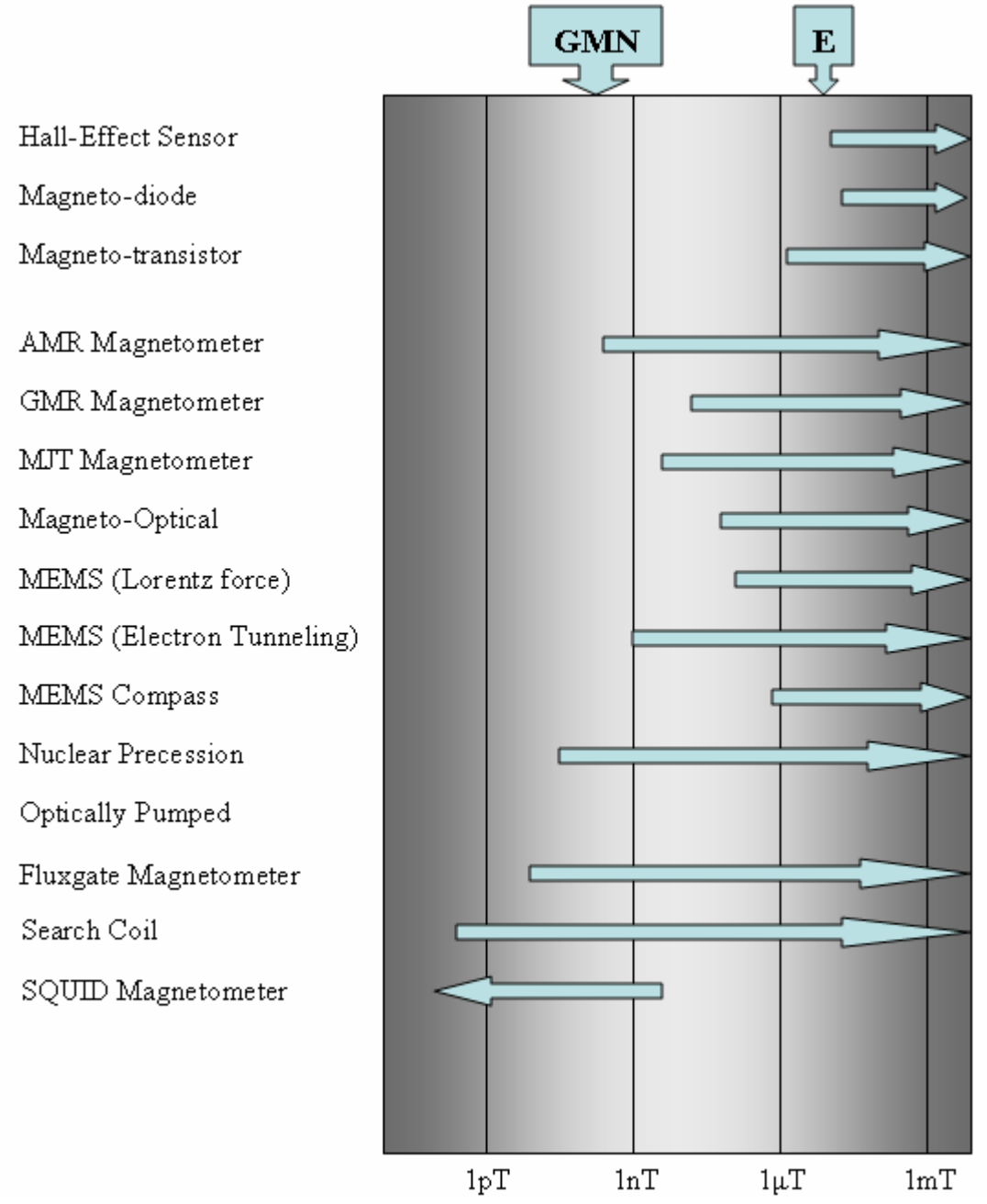

Figure 2. 1. Estimated sensitivity of different magnetic sensors. The symbols E and GMN are used to indicate the strength of the Earth's magnetic field and geomagnetic noise, respectively [2].

Table 2. 1 Features of magnetic field sensors [2, 3].

Magnetic sensors	Features
Search-coil sensors	• Wide sensitivity range from 20 fT to no upper limit. • Sensor itself consumes no power. Power consumption is limited by readout electronics. • Sensitivity scales down with area making miniaturization counter productive. • Static magnetic field can not be measured.
Hall-Effect sensors	• Inexpensive Hall-Effect sensors are generally made of silicon (~10^6 nT). For higher sensitivity, the III-V semiconductors (InSb) are used (~100 nT) [2]. • Lowering power consumption degrades sensitivity. • Typical power consumption of around 100 mW [2]. • Suffer from large offset and temperature dependence. Therefore, an offset reduction or compensation method should be used [4].
Fluxgate sensors	• Typical power consumption of 0.1 mW ~ 1 mW [5]. • Static magnetic field can be measured. • Sensitivity scales down rapidly as it is miniaturized.
Magnetoresistive (MR) sensors	• Sensitivity is around 10 nT. • The sensitivity scales down with power supplied due to a linear dependence on drive voltage [5]. • Typical power consumption of 0.5 mW [2]. • Deposition of the magnetic film is not easy [6]. • There is upper limit to their sensitivity range.
MEMS (Ferromagnetic magnetometer)[7]	• Measured magnetic fields as low as 100 μT. • Required a complex detection scheme to measure the small displacement of the magnetometer. • Power consumption is limited by electronic circuitry.
MEMS (thermal excitation, resonant) [8].	• Demonstrate the compass function. • Consumes about 5 mW for thermal actuation.
MEMS(all magnetic, resonant)	• Demonstrate measuring the Earth's magnetic field. • Power consumption is limited by electronic circuitry. • CMOS compatible silicon processing. • Very simple detection scheme using feedback loop.

Features of magnetic field sensors such as sensitivities and power consumptions are summarized in Table 2. 1.

Search-coil sensors have advantages of being high sensitive and low power, but their sensitivity scales down with area, making miniaturization counterproductive. When all of the linear dimensions of the search coil are divided by a scaling factor of s, the scaling effect for the sensitivity of the search coil is then to the inverse second power of the scaling factor (s^{-2}). Because search-coils can detect a time-varying magnetic field, it cannot detect a static magnetic field such as the Earth's magnetic field.

Semiconductor-based magnetic sensors, such as Hall-Effect sensors, magnetotransistors, and magnetodiodes, are very compact in size. The Hall-Effect sensor is widely used since its manufacturing is low-cost and CMOS compatible. However, these simple devices usually suffer from large offset, temperature dependence and some sort of offset reduction or compensation method should be used [9].

The most sensitive low-field sensor is the superconducting quantum interference device (SQUID) developed around 1962 [10]. It is based on Brian J. Josephson's work on the point-contact junction designed to measure extremely low currents [1]. The device has three superconducting components: the SQUID ring itself, the radio-frequency coil, and the large antenna loop. All three must be cooled to a superconducting state [1]. The SQUID itself can be very small, but the need for liquid-helium coolant makes the complete instrument bulky and heavy.

A fluxgate magnetometer typically consists of a ferromagnetic material wound with two coils, a drive and a sense coil. A MEMS-based fluxgate sensor can be very compact in size [11, 12]. However, its front-end circuitry tends to be complex to drive the core

into saturation and sense the output from the coil, and maintaining the saturation flux requires consumption of power. A core material should be selected carefully to have low coercivity and saturation values for low power consumption [2]. Its sensitivity scales down rapidly as it is miniaturized.

Magnetoresistive sensors (MR) feature a high sensitivity, low cost manufacturing, and compact size. However, their poor 1/f noise performance and linearity, combined with the narrow dynamic range of these sensors makes them unattractive and unsuitable for many low noise applications [13]. Furthermore, their sensitivity is degraded as the power consumption is reduced [3].

Recently Lorentz-force based resonant micromechanical magnetic sensors have been reported with good performance, but suffer from the sensitivity, which is scaled down with both dimension and power dissipation (*i.e.*, driving current) [8, 14]. Ferromagnetic micromechanical magnetometers developed by Jack W. Judy, *et al.* exhibited a high sensitivity without any scaling down effect with both dimension and power. However, the total system including detection component is not compact since they used a laser Doppler vibrometer (Polytec OFV-511) to measure the small displacement of the magnetometer [5]. Resonant magnetic field sensor with frequency output developed by Robert Sunier, *et al.* is fabricated using an industrial CMOS process, followed by a two-mask micromachining sequence to release the cantilever structure. A total actuation power around 5 mW was reported [8].

Each of the sensor approaches discussed above will be briefly described.

2.2 Search coil sensors

The search-coil magnetometer utilizes the voltage induced in the coil, which is proportional to the changing magnetic field in the coil. The sensitivity depends on the permeability of the core and the number of turns of the coil. The operation of the induction coil magnetometer can be explained with Faraday's law of induction (see Figure 2.2). A current is induced in a conducting loop when the magnetic flux linking the loop changes and a voltage proportional to the rate of change of the flux is generated between its leads. A flux through the coil will change if the coil is in a magnetic field that varies with time or if the coil is moved through a nonuniform field. A ferromagnetic core is placed inside the coil to capture the magnetic field. The sensitivity of the search-coil magnetometer is related to the permeability of the core materials, the area of coil, the number of coil turns, and the rate of change of the magnetic flux through the coil [1]. The higher inductance results in slow dissipation of the induced current and the lower resistance of the coil results in quick dissipation of the current. In practice, however, the electronic readout circuitry limits the frequency response of the sensor. The useful frequency range is typically from 1 Hz to 1 MHz. The ratio of the coil's inductance to its resistance sets the upper limit [1]. The application of the induction coil sensing will be given in the proposed research section.

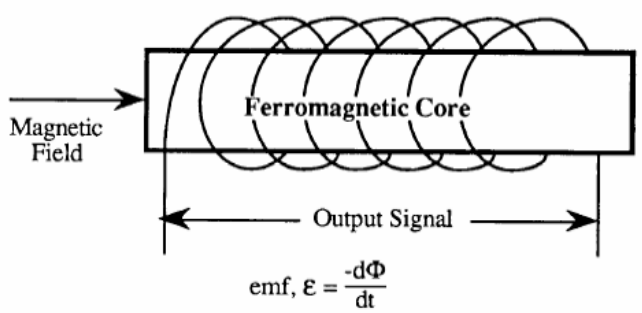

Figure 2. 2. Induction coil (search-coil) magnetometer based on Faraday's Law of Induction. When the flux density through the coil changes, a voltage appears between the coil's leads [1].

2.3 Hall-Effect sensors with magnetic flux concentrator

Hall-effect sensors utilize galvanomagnetic effects, which occur when a material carrying an electric current is exposed to a magnetic field [15]. Inexpensive Hall-effect sensors are generally made of silicon. More sensitive sensors can be made of the III-V semiconductors, which have higher electron mobility than silicon. Most commercially available Hall-effect magnetometers have sensing elements made of the III-V semiconductor indium antimonide (InSb). This type of sensor can detect either static or time-varying magnetic fields. The frequency limitation is about 1 MHz. Their power requirement is between 0.1 and 0.2W [2].

A detectable limit as low as 10 pT was reported for the combination of a Hall sensor and magnetic concentrators [16]. The characteristics of the Hall element can be improved by coupling them with the integrated magnetic concentrator [17]. The principle of the operation of the integrated magnetic concentrator is illustrated in Figure 2. 3.

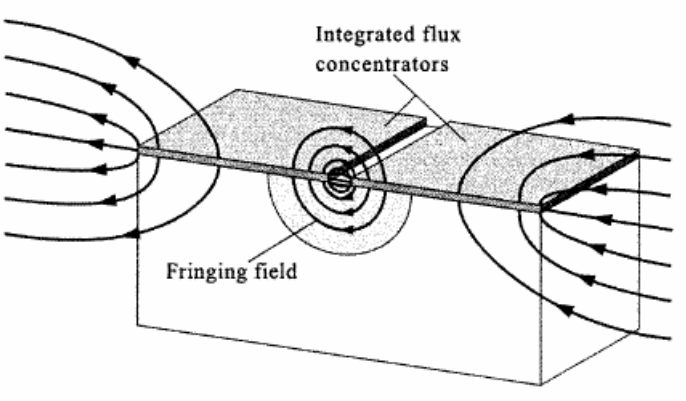

Figure 2. 3. Planar magnetic flux concentrator [18].

A high-permeability ferromagnetic layer is deposited on the chip's surface. In the middle of the chip, the ferromagnetic layer is etched and split into two pieces so that two ferromagnetic pieces are divided by a very narrow air gap. The magnetic concentrators now can capture the external magnetic field parallel with the chip's surface. In the vicinity of the air gap, the magnetic flux splits into two parts. One part keeps flowing in the horizontal direction. The other part is the fringing magnetic field created around the air gap. The simulation result shown in Figure 2. 4 shows that the fringing magnetic field has a strong vertical component near the edges of the magnetic concentrator [18]. Therefore, the magnetic concentrator will change the direction of the magnetic field from horizontal to vertical. This vertical component of the fringing magnetic field can be sensed by the Hall elements placed below the magnetic concentrator near the air gap [18]. Hence, two advantages result from the flux concentrator. It changes the direction of the magnetic field from horizontal to vertical so that the planar Hall element can be used to detect the external magnetic field parallel to the surface.

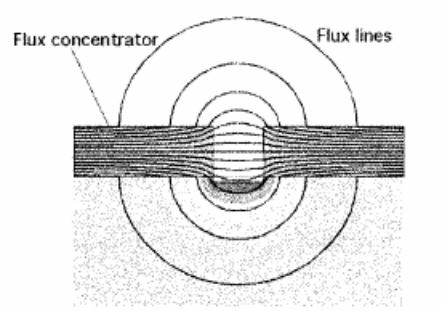

Figure 2. 4. Simulation of the fringing magnetic field around flux concentrator [18].

It also focuses the magnetic flux into a small area that can be considered an amplification of the magnetic field. The amplification factor depends on several factors [17]: the width of the air gap, the shape of the magnetic concentrator, the position where the fringing magnetic field is measured, etc. The maximum amplification is achieved when the gap distance is equal to the concentrator's thickness [17]. The nickel-iron alloys are good candidates for the ferromagnetic magnetic material because of their favorable magnetic and mechanical properties. In particular, the Ni (81%)-Fe (19%) composition permalloy shows a soft ferromagnetic behavior with low minimum coercive force and maximum permeability, while it has excellent stainless-steel-like mechanical properties and a very low magnetostriction [19]. It has been shown that for a given gap, the sensitivity of the Hall sensor is proportional to the length of the concentrators, while it can be doubled at best by increasing the width [20]. Therefore, long concentrators are preferred to wide ones. Various shapes of the flux concentrator are simulated to find optimum structure design as shown in Figure 2. 5 [21]. Among them, the amplification of the external magnetic flux is the biggest with the T-shaped flux concentrator [21].

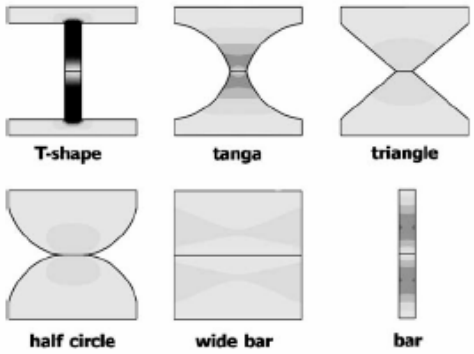

Figure 2. 5. Shapes of magnetic flux concentrators [21].

2.4 Fluxgate magnetic sensors

The fluxgate magnetometer is the most widely used sensor for compass-based navigation systems. Fluxgate type sensors can measure not only the absolute strength of a surrounding magnetic field, but also the difference in field strength between two different points within a magnetic field. The sensitivity range is from 10^{-2} to 10^{7} nT [2].

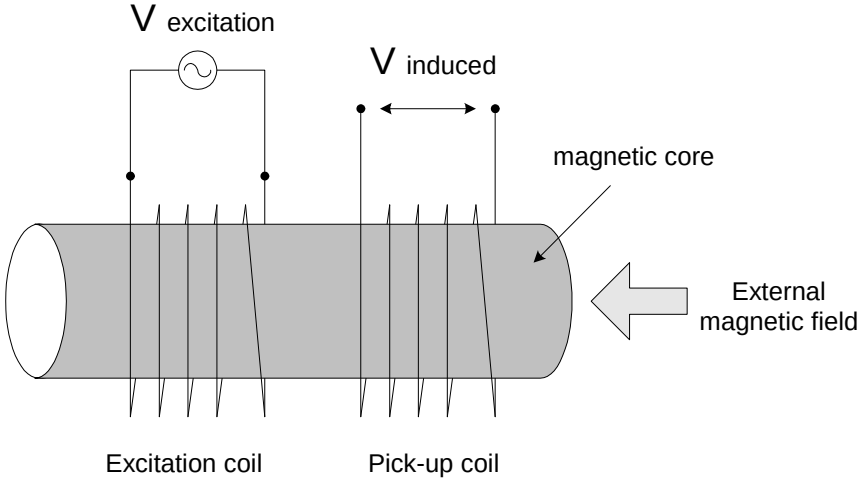

Figure 2. 6. The basic configuration of the fluxgate sensor [22].

The measurement principles of fluxgate sensors can be divided into second harmonic principle, pulse position principle, and pulse-height principle [23]. The so-called second harmonic device is the most common type, which consists of two coils, a primary and a secondary, wrapped around a common high-permeability ferromagnetic core. Figure 2. 6 shows the basic fluxgate sensor configuration. A drive signal applied to the primary coil (excitation coil in Figure 2. 6) is large enough to cause the core to oscillate between saturation points. Then a periodic pulse voltage is induced in the secondary coil (pick-up coil in Figure 2. 6). When a DC external magnetic field is applied, the phase of the induced pulse is changed. The second harmonic sensing principle utilizes the fact that the even harmonics, especially the second harmonic, are produced in the pick-up coil when the induced pulse phase is changed due to the external magnetic field. The fluxgate is the most sensitive among the magnetic sensors, which can be used at room temperature [24]. The main drawbacks of the conventional fluxgate sensors are their large size, high power consumption, and cost. There have been several efforts to build a small, fully integrated micro fluxgate sensor [15, 22, 25-36]. Kawahito *et al.* presented a fluxgate sensing element for a high-performance silicon-based integrated magnetic sensor [22]. The sensor core used is permalloy film formed by electrodeposition. They achieved sensitivity of 5.8 V/T at 100 kHz; it is difficult to achieve sensitivity of over 1 V/T (~ 400 V/AT = 0.4 V/T with 1 mA supply current for typical Hall sensors [23]) using silicon Hall elements. Liakopoulos *et al.* showed very good linear response over the range of –500 μT to +500 μT, with a system sensitivity of 8360 V/T at 100 kHz with amplifiers (418 V/T for 100 kHz without amplifiers) and a resolution of 60 μT by constructing three-dimensional planar solenoid coils for the excitation and sensing

elements [25]. They reported a power consumption of about 100 mW. Gottfried-Gottfried *et al.* combined a planar technology for the fluxgate with a CMOS-ASIC for readout and signal processing [26]. A sensitivity of 9200 V/T was achieved at 350 kHz. A printed circuit board (PCB) has also been used to realize fluxgate magnetic sensors [27, 28]. Dezuari *et al.* presented a hybrid PCB/magnetic metal foil technology to build a relatively inexpensive fluxgate sensor with sensitivity of 60 V/T at 30 kHz [27]. Most of the fluxgate sensors, however, have been developed to measure the absolute magnetic field intensity [22, 25, 26]. There has been research on building 2-D fluxgate sensors to measure the direction of the external magnetic field [27, 29-32, 37]. Dezuari *et al.* showed in their experiments the potential of the fluxgate device for application as a magnetic compass [27]. They applied the external field perpendicular and parallel to the detection coil and showed the dependence of the second harmonic output voltage on the orientation of the external field. Kawahito *et al*. presented a single-chip integrated micro-fluxgate sensor with a ΣΔ analog-to-digital converter (ADC) based on a CMOS process [29]. They reported a power consumption of 325 mW from a 5 V supply and an angular resolution of 4° at a magnetic induction of 50 μT. Kejik *et al*. developed a 2-D planar fluxgate sensor using similar orthogonal planar coils and a ferromagnetic ring-shaped amorphous metal core, mounted on a PCB substrate [37]. They reported a sensitivity of 55000 V/T at 8.4 kHz with a precision angle better than 1°. Chiesi *et al*. developed a two-axes parallel fluxgate magnetometer[30]. They reported a sensitivity of 3760 V/T at 125 kHz and a power consumption of 12.5 mW. The angle error on the Earth's magnetic field is ±1.5°. Hwang *et al*. presented a micro fluxgate sensor fabricated on silicon substrate [31]. They reported a sensitivity of 210 V/T at 1.2 MHz and estimated the power

consumption of ~14 mW. Drljaca *et al*. developed a single-core fully integrated CMOS fluxgate sensor[32]. They reported a sensitivity of 160 V/T at 250 kHz and a power consumption of 17 mW for the biasing, driving, and readout electronics. The performances for the 2-D fluxgate sensors reviewed so far are summarized in Table 2. 2.

Table 2. 2. The performance of the various 2-D fluxgate sensors.

	Power consumption [mW]	Sensitivity [V/T]	Angular resolution
Kawahito *et al*.[29]	325	-	4° at 50 μT
Kejik *et al.* [37]	-	55 @ 8.4 kHz	Better than 1° at 50 μT
Chiesi *et al.* [30]	12.5	3760 @ 125 kHz	1.5° at 19 μT
Hwang *et al.* [31]	14	210 @ 1.2 MHz	5.5° at terrestrial field
Drljaca *et al.* [32]	17	160 @ 250 kHz	-

2.5 Magnetoresistive (MR) sensors

A magnetoresistive (MR) effect is observed in soft ferromagnetic materials such as Co, Ni, and Fe and all metal materials. These type sensors use a change in resistance ΔR caused by an external magnetic field H.

Anisotropic magnetoresistance (AMR) and, recently giant magnetoresistance (GMR), sensors are the latest competitors of micro fluxgate sensors. The magnetoresistive sensors are made of a nickel-iron (Permalloy) thin film deposited on a silicon wafer and patterned as a resistive strip. One of the typical configurations is to connect four of these resistors as a Wheatstone bridge. In the presence of an external

magnetic field, the magnetoresistive characteristic of the Permalloy caused a resistance change in the bridge and a corresponding change in voltage output. The AMR sensors have high resolution and high bandwidth, but they saturate at a small magnetic field (less than 1 mT) and they may require a complex resetting procedure [33]. The AMR sensors are smaller, but less precise than the fluxgate sensors [34]. The GMR magnetic sensors also have high resolution and high bandwidth but have a high hysteresis and can be destroyed by a low magnetic field [33]. Commercialized magnetoresistors show generally a resolution of 10 nT with a sensor size of several milimeters, but their drawback is the limited precision resulting from the large temperature coefficient of sensitivity (typically 600 ppm/°C, compared to 30 ppm/°C for fluxgate) [35]. Both magnetoresistors and fluxgates need to periodically saturate their cores to remove offset caused by residual DC magnetization. As a result, similar electronic circuits are adopted for both applications and there are no major differences in power consumption [35]. There are commercially available AMR sensors such as the Honeywell AMR type HMC1051 and the Phillips AMR type KMZ52. The power consumptions are around 130 mW for the KMZ52 and more than 100 mW for the HMC1051 [38, 39]. Table 2. 3 summarizes the performance of other sensors of these companies.

Table 2. 3. Characteristics of some AMR sensors [33].

	HMC 1021	KMZ10A
Power Consumption	~ 100 mW	~ 130 mW
Sensitivity	50 mV/mT	64 mV/mT
Resolution at DC field	3 μT	30 μT

2.6 MEMS-based magnetic sensors

Resonant magnetic sensors also have been developed for high-sensitivity applications. A silicon substrate is generally used since it shows the excellent mechanical properties of single-crystal silicon, such as high modulus, extremely low dislocation rate, good resistance to fatigue, and low thermal expansion coefficient. Furthermore, a magnetic sensor built on a silicon substrate is easily combined with CMOS circuitry. Donzier *et al*. realized a silicon beam resonant magnetic field sensor [36]. The excitation of the resonator was achieved by the Lorentz force generated by an alternating current flowing through a coil deposited on the surface of the beam. The vibration amplitude is transformed into an electrical signal by a piezoresistive gauge bridge diffused in the silicon resonator. Kadar implemented a torsional resonant magnetic field sensor [6]. The excitation of the resonator is achieved by the external magnetic field and the current flowing through a coil on the surface of the silicon device. The detection of the torsional movement was done by converting the changes of the sensing capacitors into the electrical signal output using charge amplifiers. Judy *et al.* developed a ferromagnetic micromechanical magnetometer that integrates electroplated cobalt-based magnetic materials with surface micromachined polysilicon structures [7]. Their prototype devices measured a magnetic field as low as 100 μT. It was further developed by Yang *et al.* By optically measuring the small displacement, it detected magnetic fields as low as 500 nT. However, the total system they used was not compact due to a laser Doppler vibrometer (Polytec OFV-511) [5]. Recently, a CMOS integrated resonant magnetic field sensor with frequency output was reported [8]. It exploits the Lorentz force developed on a mechanical resonator, a cantilever structure which is embedded as the frequency-

determining element in an electrical oscillator. It consumes around 5 mW for the thermal actuation.

A low power resonant micro-machined compass (see Figure 2. 7) was fabricated and demonstrated as a magnetic compass by Leichle [40]. He built the resonant comb drive structure using an epoxy (SU-8) and glued the permanent magnet (NdFeB) onto the surface of the epoxy structure. The interaction between an external magnetic field and the permanent magnet causes a shift of the fundamental resonant frequency (f_c) of the device. As a result, the amplitude of the direction of the external magnetic field can be determined from this shift of the resonant frequency. A small AC signal was superimposed on the relatively high DC signal to actuate the comb drive resonator electrostatically. He reported a minimum resolution of 45° at 30 μT or less, at an excitation voltage of 10 V. The power consumed to actuate the resonator was on the order of 20 nW [40]. However, the SU8 structure is not compatible with some of the silicon based CMOS processes [41]. Furthermore, the mechanical properties of SU8 are not good in terms of quality factor and thermal coefficient. To overcome these drawbacks (not CMOS compatible, poor mechanical properties of SU8 structure), a silicon-based resonant magnetic sensor is designed, fabricated, and measured with low power consumption and low operation voltage (see section 2. 8). The device is also characterized to maximize the sensitivity at given physical dimension by maximizing nonlinearity.

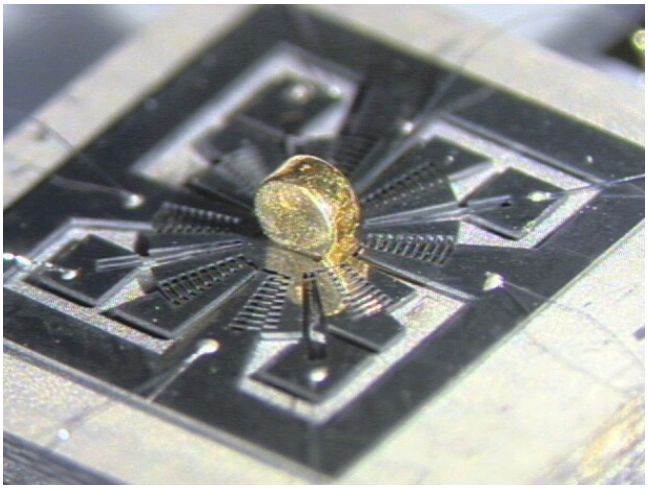

Figure 2. 7. Photograph of a fabricated resonator incorporating a permanent magnet [41].

2.7 MEMS-based mechanical resonator

Micromachined mechanical resonators are widely used as key sensing elements as is shown in the previous subsection. Micromechanical oscillators have been considered as an attractive replacement for quartz crystal oscillators as timing references since they are not only CMOS compatible, but also can be small. Much research has been done on replacing the quartz crystal with MEMS resonators [42-48]. The resonant frequency of the MEMS resonator can be extracted by configuring it within a positive oscillation feedback loop. Figure 2. 8 shows a typical schematic for the micro-resonator oscillator. If we connect the output terminal to the frequency counter, we can find the resonant frequency of the resonator. The MEMS resonator can be described by an electrical equivalent circuit composed of series LCR circuits[42]. The equivalent circuit for a two-port micromechanical resonator is presented in Figure 2. 9. The parasitic feedthrough

capacitor (C_0) couples the drive voltage over to the port where the motional current is sensed [42]. This parasitic capacitor is one of the main sources of phase shift in the feedback loop used in the oscillation circuit. To bias and excite the device, a direct current (DC)-bias voltage V_p is applied to the resonator, while an AC excitation voltage is applied to one drive electrode. The polarization voltage (V_p) has two purposes. The first function is to avoid having the microstructure moving at twice the frequency of the applied drive voltage. The second function of the polarization voltage is to amplify the output motional current resulting from the microstructure motion [43]. A motional output current i_0 arises at the output port when the device is in oscillation, creating a time-varying capacitance between the micro-resonator and the electrodes.

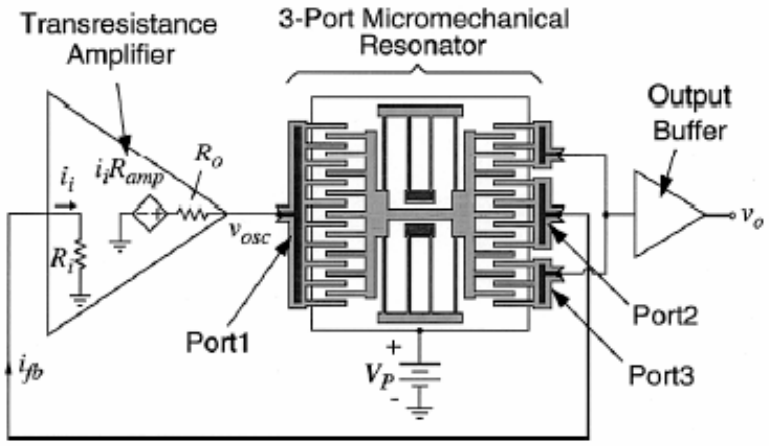

Figure 2. 8. System-level schematic for the micro resonator [47].

The motional current is proportional to the DC-bias V_p and the time-varying capacitance is given by:

$$i_0 = V_p \frac{\partial C}{\partial t} = V_p \frac{\partial C}{\partial x} \frac{\partial x}{\partial t} \tag{2. 1}$$

where x is the displacement of the beam and $\partial C / \partial x$ is the change in capacitance per unit displacement. For the interdigitated-comb drive resonator, the capacitors vary linearly with displacement. Thus, $\partial C / \partial x$ is a constant, given approximately by the expression:

$$\frac{\partial C}{\partial x} \cong \frac{\alpha \cdot N \cdot \varepsilon \cdot h}{d} \tag{2. 2}$$

where N is the number of finger gaps, h is the film thickness, and d is the gap between electrode and resonator fingers [44]. α is a constant that models additional capacitance resulting from fringing electric field. For comb geometries, α = 1.2 [45]. At a given resonant frequency, *i.e.*, given $\partial x / \partial t$, the output current is proportional to the DC bias voltage (V_p), the number of the comb fingers and the thickness of the structure. The smaller the gap (d) is, the larger the output current (i_0) is. For the frequency-selective element, the series resistance, also called motional resistance, is of most interest. The larger R_x needs more gain, and thus more power dissipation, from the amplifier sustaining oscillation [46].

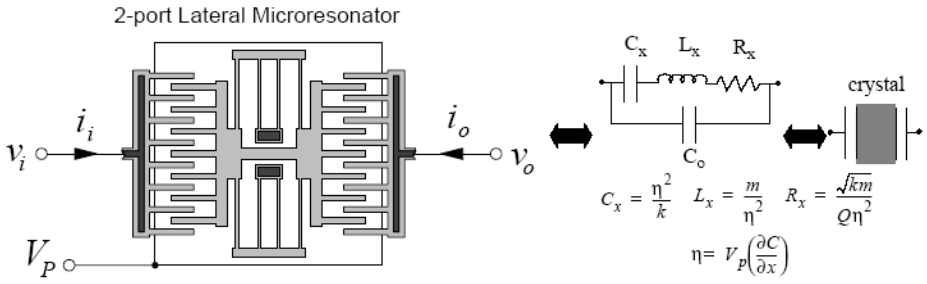

Figure 2. 9. Equivalent circuit for a two-port micro resonator composed of LCR. In the equations, k is the system spring constant and $(\partial C/\partial x)_n$ is the change in capacitance per displacement at port n of the micro resonator [42].

2.8 A low power micromachined resonant compass

This dissertation presents a complete magnetic sensing system that consumes less than 200 microwatts of power in continuous operation, and is capable of sensing the Earth's magnetic field. Such low power consumption levels enable continuous magnetic field sensing for portable electronics and potentially wristwatch applications, thereby enabling personal navigation and motion sensing functionalities. The system is composed of a micromachined silicon resonator combined with a permanent magnet, excitation and sensing coils, and a magnetic feedback loop for the completion of the system. A total system power consumption of 138 μW and a resonator actuation voltage of 4mVpp from the ±1.2V power supply have been demonstrated with a sensitivity of 0.11 Hz/degree for the Earth's magnetic field. The power consumption level is at least 1-2 orders of magnitude smaller than previously reported values (a few mW range) for Earth magnetic field sensors in the literature [2, 32, 49, 50]. It can be operated continuously more than 3000 hours with a standard wristwatch battery (CR2025; 3V, 140 mAh).

The resonant structure consists of a permanent magnet torsionally supported on a resonant disc. The interaction between an external magnetic field H such as the Earth's magnetic field and the magnetization of the permanent magnet M generates a torque which changes the stiffness of the beam, resulting in a change of the resonant frequency of the sensor (Figure 2. 10). The resonator with electromagnetic sensing and excitation coils is hybrid integrated with self-oscillation electronics and gives a resonant frequency shift as a function of the strength and orientation changes of the external magnetic field H.

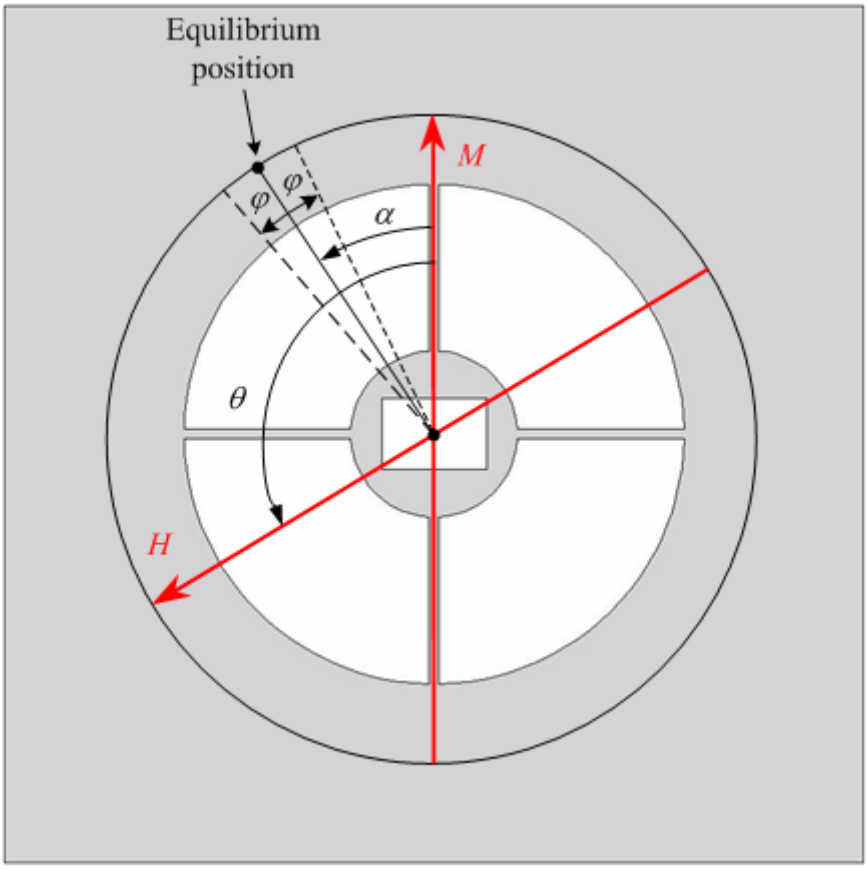

Figure 2. 10. Principles of operation. M is the magnetization direction of the magnet, H is the direction of the external magnetic field, α is the rotational angle of the permanent magnet, φ is the small oscillation angle, θ is the angle between the H and the M .

The fabrication is based on a two-mask, single wafer silicon bulk micromachining process. A recess is inductively-coupled-plasma (ICP) etched into the bottom side silicon wafer to reduce the thickness of the resonator structure (Figure 2. 11 (a)). The top side silicon wafer is etched by ICP to form a movable resonant disc, a recess for a permanent magnet, and support beams (Figure 2. 11 (b)). The permanent magnet is adhered to the center of the moving disc (Figure 2. 11 (c,d)). Figure 2. 11 (e,f) show SEM images of the fabricated device which has 4 beams that are 17 μm wide, 2mm long, and 110 μm thick.

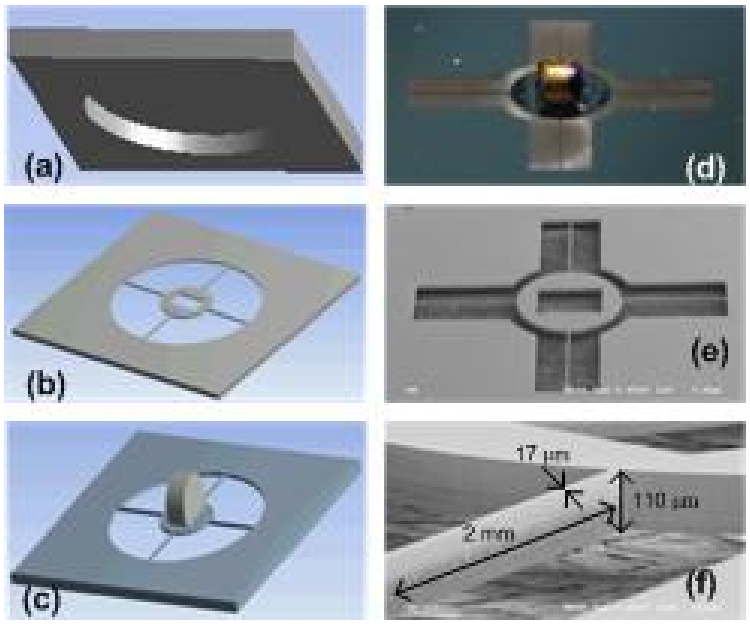

Figure 2. 11. Schematic views of the fabrication processes (a,b,c) and fabricated structures (d,e,f); (a) Bottom recess etch, (b) RIE deep silicon etch, (c) assembly of the magnet, (d) complete image after assembly of magnet, (e,f) SEM images of the fabricated resonator

The excitation and sensing coils and associated electronics are hybrid-assembled with the sensor (Figure 2. 12). The resonance frequency is automated for data-acquisition for every second with a device rotation of 1 rpm. A driving voltage of 4mVpp and a power consumption of 9.64 μW are measured for the excitation of the resonant sensor. Sensitivity of 0.11Hz/degree is obtained for the Earth's magnetic field, and of 0.24, and 0.54 Hz/degree are achieved for the applied fields of 0.195 mT and 0.39 mT respectively.

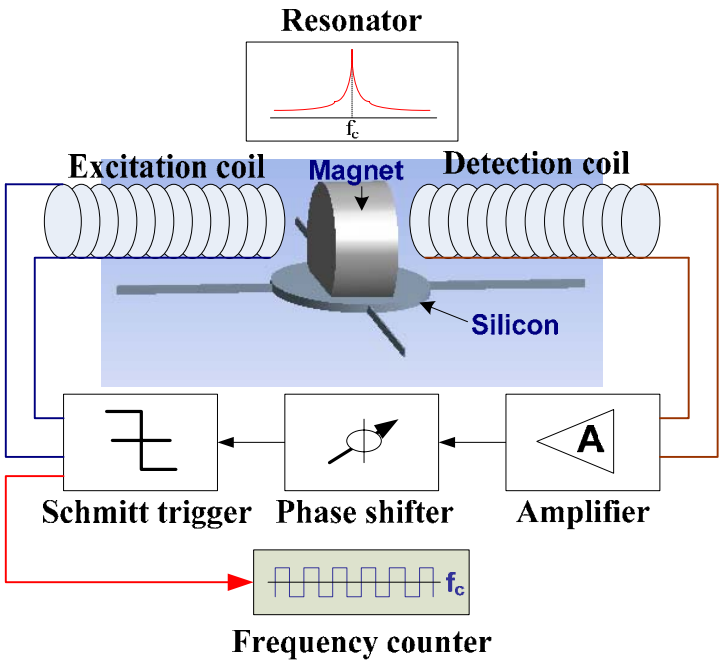

Figure 2. 12. The completed sensing systems with electromagnetic excitation and sensing coils and electronic circuitry.

2.9 Conclusions

The sensors reviewed so far exhibit variable sizes, performance, complexity of configurations, and applications. However, such sensors are not the best candidates for mobile electronic components such as cellular phone applications and wristwatch applications, which require ultra-low-power consumption. A wristwatch consumes approximately 4.5 μW with a 309 battery (voltage of 1.55 V and typical capacity of 80 mAh). Therefore, the compass should consume the same order of power consumption as the wristwatch. Search-coil magnetometers have the advantage of being low power (all power is consumed by sense electronics), but their sensitivity scales down with area. Fluxgate magnetometers have a high sensitivity, but it scales down rapidly as it is miniaturized. Although Hall-Effect sensors are very compact, the sensitivity and power consumption of these magnetometers are not competitive. MEMS-based resonant magnetic sensor shows very high sensitivity and possible low power operation.

The goal of this research is to develop a low power consumption compact magnetic sensor which is capable of measuring the Earth's magnetic field. A micromachined resonator is used as a frequency selective element in the entire oscillating structure for high sensitivity and the search-coil actuation and detection schemes are combined with it for low power consumption and low voltage operation. The silicon substrate enhances the performance of the sensor in terms of better mechanical properties such as consistent thermal coefficient, stiffness, and good quality factor. The CMOS compatibility is also an advantage of silicon-based sensors compared to the previously demonstrated epoxy-based structure.

CHAPTER 3

THEORETICAL MODELING AND CHARACTERIZATIONS

In this chapter a theoretical model for the mechanical resonator is provided. An optimized design is suggested based on the theoretical model and fabrication constraints. Furthermore, sensitivity is characterized as a function of beam width and number of beams.

3.1 Theoretical modeling

Theoretical modeling is carried out to gain a fundamental understanding of a mechanical resonator and the sensitivity characteristics of the micromachined resonant magnetic sensor. A thorough understanding of both the linear and nonlinear models is necessary for successful design and fabrication of the micromachined resonant magnetic sensor.

3.1.1 Linear modeling

The resonator can be simplified to a torsional vibratory system with one degree of freedom, shown in Figure 3.1.

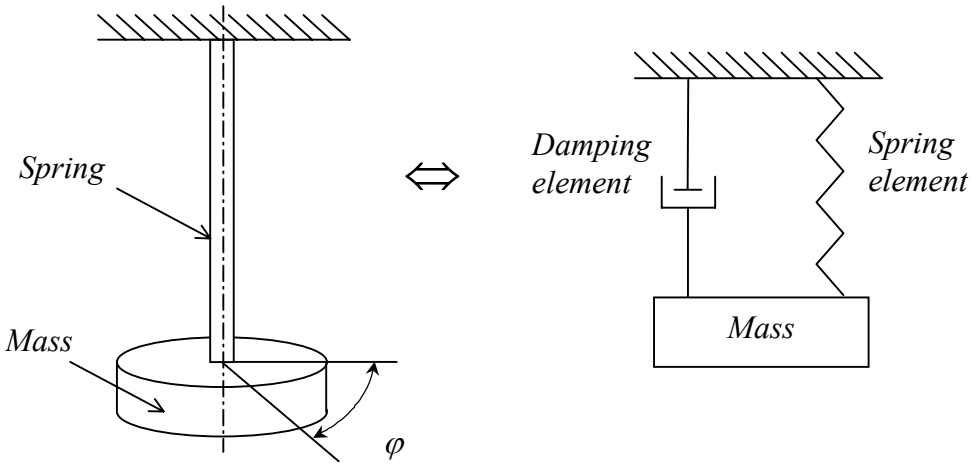

Figure 3. 1. Schematic of a single degree of freedom torsional vibratory system (left) and its equivalent mechanical model [41].

The governing equation describing the motion of the resonator is obtained by summing the moments acting on the resonator disk [51]. At small oscillation, this equation is:

$$I\,\ddot{\varphi} + c\,\dot{\varphi} + k_l\varphi = T(t) \tag{3. 1}$$

where I is the mass moment of inertia of the system, k_l is the linear torsional stiffness coefficient of the beams, c is the damping constant and T is an external applied torque. Assuming negligible damping, and no external torque, Equation (3.1) becomes:

$$I\,\ddot{\varphi} + k_l\varphi = 0 \tag{3. 2}$$

The fundamental resonant frequency of this system, f_0, is:

$$f_0 = \frac{1}{2\pi}\sqrt{\frac{k_l}{I}} \tag{3. 3}$$

For small rotational angle of the cylindrical mass, the torsional stiffness coefficient of one beam, k_l, can be approximated to its stiffness coefficient under lateral load, k_{ll},

times the squared radius of the center silicon disk, r_{si}, (Figure 3. 2). The relationship between the torque applied and the angle of rotation can be expressed as,

$$T = k_l \cdot \varphi = P \times r_{si} = k_{ll}\delta \times r_{si} \approx k_{ll} r_{si}^{\,2} \varphi \tag{3. 4}$$

$$\Rightarrow\ k_l \approx k_{ll} r_{si}^{\,2} \tag{3. 5}$$

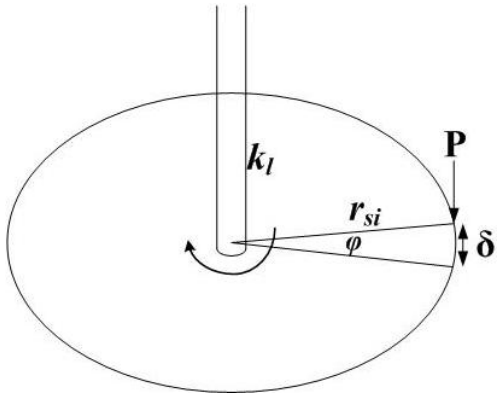

Figure 3. 2. A torsional stiffness approximation from the lateral stiffness coefficient.

The stiffness coefficient of a one beam with one end guided and one end fixed is given by Roark's formulas for stress and strain [52]:

$$k_{ll} = \frac{12EI_b}{l_b^{\,3}} \tag{3. 6}$$

where l_b is the length of the beam, and I_b is the moment of inertia of the section of the beam with respect to the neutral axis:

$$I_b = \frac{t_b \cdot w_b^3}{12} \tag{3. 7}$$

where t_b is the thickness and w_b is the width of the beam, respectively. Hence,

$$k_l = k_{ll} \cdot r_{si}^{\ 2} = \frac{E \cdot t_b \cdot w_b^3}{l_b^3} \cdot r_{si}^{\ 2} \tag{3. 8}$$

The mass moment of inertia of the resonator is obtained by adding the mass moments of inertia of the silicon central disc and the mass moment of inertia of the cylindrical permanent magnet. The expression of the mass moment of inertia is obtained from [53]:

$$I = \pi \rho_{si} t_{si} \left(\frac{r_{si}^4}{2} \right) + \left(\frac{\pi \rho_m r_m^{\ 2} t_m^{\ 3}}{12} + \frac{\pi \rho_m r_m^{\ 4} t_m}{4} \right) \tag{3. 9}$$

where t_{si}, ρ_{si}, and r_{si} are the thickness, density, and radius respectively of the central disc of the silicon resonator and t_m, ρ_m, and r_m are the thickness, density, and radius respectively of the permanent magnet.

The resonant frequency of the resonator is obtained by substituting Equation (3. 8) and Equation (3. 9) into Equation (3. 2), and is finally given below:

$$f_0 = \frac{1}{2\pi} \sqrt{\frac{\frac{E \cdot t_b \cdot w_b^3}{l_b^3} \cdot r_{si}^{\ 2}}{\pi \rho_{si} t_{si} \left(\frac{r_{si}^4}{2} \right) + \left(\frac{\pi \rho_m r_m^{\ 2} t_m^{\ 3}}{12} + \frac{\pi \rho_m r_m^{\ 4} t_m}{4} \right)}} \tag{3. 10}$$

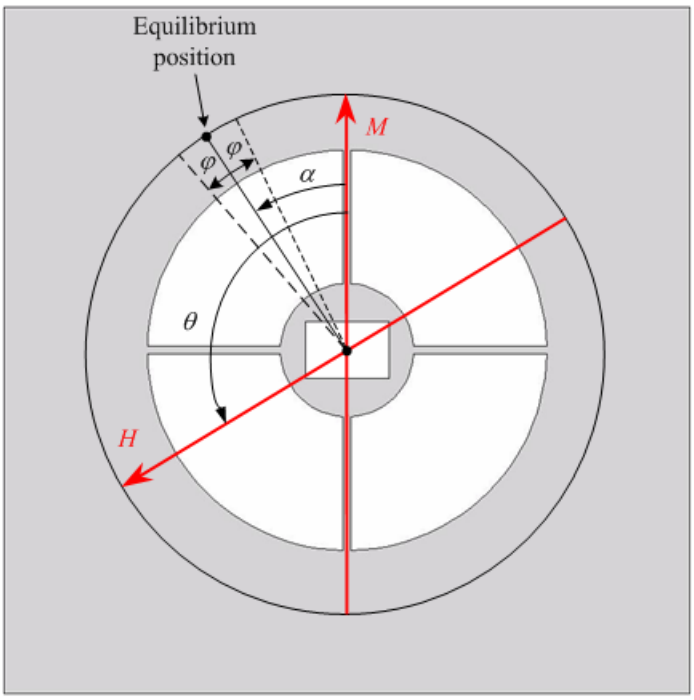

Figure 3. 3. Schematic drawing of the device including the definition of the angles.

Although the idealization of Figure 3. 1 is useful in gaining understanding of resonator performance, it is unrealistic to fabricate using standard micromachining approaches. Instead, consider the planar resonator shown in Figure 3. 3. φ is the angle of oscillation, and θ is the angle between the direction of the magnetization, M, (which is fixed with respect to the geometry of the magnet) and the external magnetic field, H. When the direction of magnetization is parallel to the external field, the magnetic torque is zero and the static resonator does not experience any rotation. However, when the resonator is oscillating the torque increases as the rotational resonator is pulled away from its equilibrium position. Assuming small oscillation and negligible damping, the Equation (3. 1) now can be expressed as:

$$I\ddot{\varphi} + k_l\varphi - T_0 \sin(\theta - \varphi) = 0 \tag{3. 11}$$

For simplicity, T_0, is the amplitude of the magnetic torque, and is given by Equation (3. 12) for a permanent magnet of volume V and magnetization M. When the direction of magnetization is parallel to the external field, the expression of the resonant frequency is given by Equation (3. 13):

$$T_0 = \mu_0 MVH \tag{3. 12}$$

$$f_0 = \frac{1}{2\pi}\sqrt{\frac{k_l + T_0 \cos\theta}{I}} \tag{3. 13}$$

where θ is 0° or 180°.

3.1.2 Nonlinear modeling

When the magnetization and the magnetic field are not perfectly aligned (θ is not 0° or 180°), the silicon center disc rotates by an angle α due to the magnetic torque (see Figure 3. 3). This angle is determined by solving the equilibrium equation stating that the sum of the torques acting on the system has to be zero:

$$k_l\alpha - T_0 \sin(\theta - \alpha) = 0 \tag{3. 14}$$

where k_l is the torsional linear stiffness coefficient of beams. In the case of large rotation angles, the beams are subject to large deflections and their load-deflection behavior is no longer linear. A cubic term multiplied by a torsional nonlinear stiffness coefficient, k_{nl}, has to be added to the equilibrium equation:

$$k_l\alpha + k_{nl}\alpha^3 - T_0 \sin(\theta - \alpha) = 0 \tag{3. 15}$$

Nonlinear effects have to be taken into account whenever the deflection (approximated to the product of the angle of deflection, α, and the radius of the silicon center disc, r_{si}) is comparable to or larger than the width of one beam, w_b. The beams tend to get stiffer as the angular deviation increases. Hence, the resonator oscillating around the new equilibrium position, α, exhibits a higher resonant frequency. The expression of the fundamental resonant frequency of the sensor is obtained by solving the differential equation satisfied by the angle of vibration, φ:

$$I\ddot{\varphi} + k_l(\alpha + \varphi) + k_{nl}(\alpha + \varphi)^3 = T_0 \sin(\theta - (\alpha + \varphi)) \tag{3. 16}$$

For small oscillation angles of φ, Equation (3. 16) becomes:

$$I\ddot{\varphi} + \left(k_l + 3k_{nl}\alpha^2 + T_0 \cos(\theta - \alpha)\right)\varphi = T_0 \sin(\theta - \alpha) - k_l\alpha - k_{nl}\alpha^3 \tag{3. 17}$$

Hence, the resonant frequency of the system is:

$$f_0 = \frac{1}{2\pi}\sqrt{\frac{k_l + 3k_{nl}\alpha^2 + T_0 \cos(\theta - \alpha)}{I}} \tag{3. 18}$$

To solve this equation k_l, k_{nl}, and the relationship between θ and α have to be determined. The k_l, and k_{nl} can be approximated by the nonlinear equations of the beam that has one end clamped and one end guided subject to large deflection [54] although the limits of this approximation will be verified by finite elements. The deflection δ for a concentrated load P at the end of a beam of length l_b, thickness t_b, second moment of inertia I_b, and elastic modulus E, can be found by simultaneously solving the following equations (Figure 3. 4):

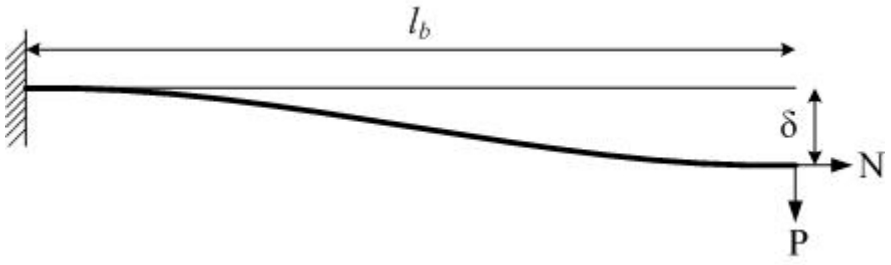

Figure 3. 4. Beam with large deflection [54].

$$P = \frac{E \cdot t_b \cdot w_b^4}{3 \cdot {l_b}^3} \sqrt{\frac{2}{3}} u^3 \left(\frac{3}{2} - \frac{1}{2} \tanh^2 u - \frac{3}{2} \frac{\tanh u}{u} \right)^{-\frac{1}{2}} \tag{3. 19}$$

$$\delta = w_b \sqrt{\frac{2}{3}} (u - \tanh u) \left(\frac{3}{2} - \frac{1}{2} \tanh^2 u - \frac{3}{2} \frac{\tanh u}{u} \right)^{-\frac{1}{2}} \tag{3. 20}$$

$$u = \sqrt{\frac{N}{EI_b}} \left(\frac{l_b}{2} \right) \tag{3. 21}$$

where N is the normal force that develops in the beam as the result of the applied force. The numerical values for applied force (P) and the resultant deflection (δ) are calculated at a given u (Equation 3. 21) thereby generating the relationship between the deflection and the force. The numerical values used for the theoretical modeling are summarized in Table 3. 1. A cylindrically shaped permanent magnet is used throughout modeling and measurement (Figure 3. 5). This relationship of the force and the deflection is plotted in Figure 3. 6 using Microsoft EXCEL.

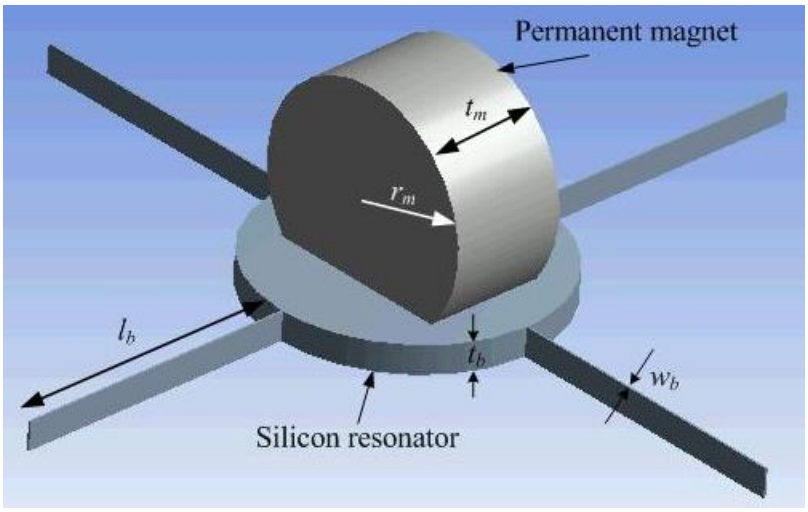

Figure 3. 5. A silicon resonator structure with permanent magnet.

Table 3. 1. Parameters used for theoretical modeling.

Young's modulus (E_{si})	165 GPa	Young's modulus (E_{magnet})	152 GPa
Density of silicon	2330 kg/m^3	Density of magnet	7440 kg/m^3
Beam thickness (t_b)	200 μm	Magnet radius (r_m)	800 μm
Beam width (w_b)	20 μm	Magnet thickness (t_m)	800 μm
Beam length (l_b)	2 mm	Number of beams	4
Center disc radius (r_{si})	1 mm	Mass moment of inertia	$3.285 \cdot 10^{-12}$

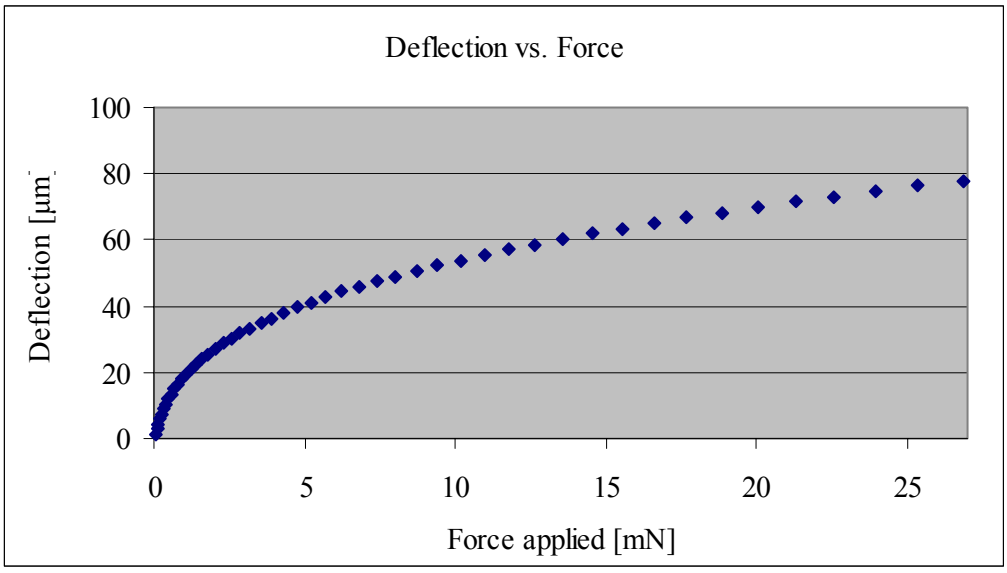

Figure 3. 6. The deflection to force graph which takes the nonlinearity of the beams into account.

The functional relationship between deflection and force is described using the following equation:

$$P = k_{\delta,l}\delta + k_{\delta,nl}\delta^3 \tag{3. 22}$$

where $k_{\delta,l}$ and $k_{\delta,nl}$ are lateral linear and nonlinear stiffness coefficients, respectively.

The Equation (3. 22) is modified further to find the stiffness coefficients easily as,

$$\frac{P}{\delta} = k_{\delta,nl}\delta^2 + k_{\delta,l} \tag{3. 23}$$

Now, the nonlinear stiffness coefficient is the slope of the new curve and the linear stiffness coefficient is the intercept of the curve with the y axis (Figure 3. 7). The numerical values of $k_{\delta,l}$ and $k_{\delta,nl}$ are found to be 33.19 N/m and 5.13×10^{10} N/m, respectively from Figure 3. 7.

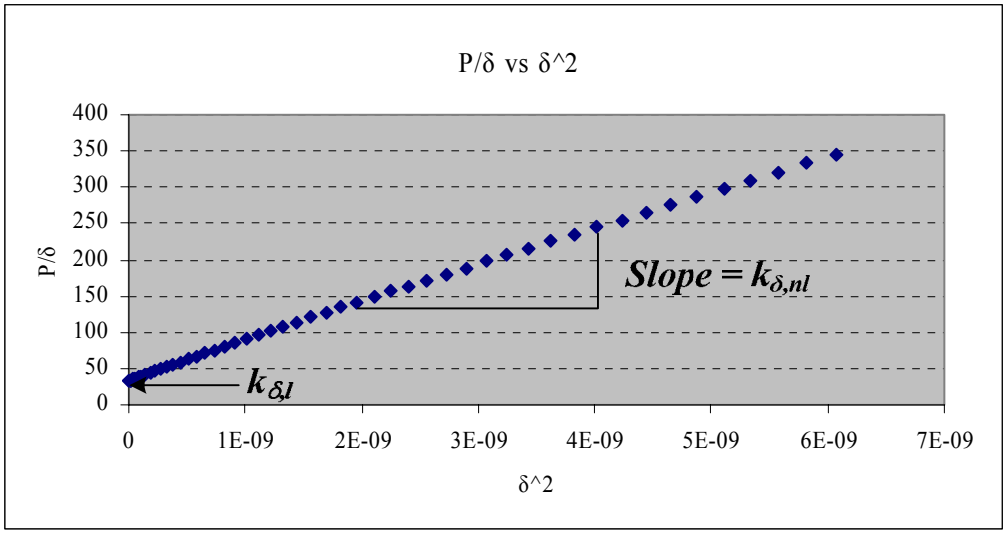

Figure 3. 7. P/δ vs. δ^2 curve. $k_{\delta,nl}$ and $k_{\delta,l}$ cab be easily calculated from this curve.

Numerical values of the torsional linear and nonlinear stiffness coefficients are obtained by considering the torque and force relationship (Figure 3. 2):

$$T = k_l\alpha + k_{nl}\alpha^3 = P \cdot r_{si} = k_{\delta,l} \cdot r_{si} \cdot \delta + k_{\delta,nl} \cdot r_{si} \cdot \delta^3 \quad (3.\ 24)$$

$$= k_{\delta,l} \cdot r_{si}^2 \cdot \alpha + k_{\delta,nl} \cdot r_{si}^4 \cdot \alpha^3 \quad (3.\ 25)$$

Therefore, the torsional linear (k_l) and nonlinear stiffness (k_{nl}) coefficients of the resonator with the number of beams (N_b) are,

$$k_l = N_b k_{\delta,l} r_{si}^2 \quad \text{and} \quad k_{nl} = N_b k_{\delta,nl} r_{si}^4 \quad (3.\ 26)$$

Hence, the numerical values of the torsional linear and nonlinear torsional stiffness coefficients of the single beam were calculated to be 3.32×10^{-5} Nm and 5.13×10^{-2} Nm, respectively. The k_l and k_{nl} of the resonator are calculated by multiplying the number of beams by these numbers (Equation 3. 26). As expected, the value of the linear stiffness

coefficient of one of the beams acquired from this model is very close to the value given by Equation (3. 8) of 3.3×10^{-5} Nm.

As shown in Equation (3. 15), the deviation angle α is a function of the stiffness coefficients of the beams, the magnitude of the magnetic torque and the angle formed by the direction of the magnetization and the magnetic field. The nonlinear Equation (3. 15) is numerically solved using MATLAB. The linear and nonlinear torsional stiffness of 132.13×10^{-6} Nm and 18.7×10^{-2} Nm are used along with the structural dimensions listed in Table 3. 1.

Figure 3. 8 shows the plot of α (in degree) as a function of θ (in degree). The graph shows that the larger the equilibrium angle (α), the greater the magnitude of the external magnetic field. The graph also shows that the shape of the curve is very close to the *sine* function of theta (θ). Assuming the magnitude of alpha is small compared to θ and k_{nl}, the Equation (3. 15) can be written as the Equation (3. 27). Figure 3. 9 show the approximation of the α-curve into the arbitrary *sine* functions.

$$k_l\alpha \cong T_0 \sin\theta$$

$$\Rightarrow \quad \alpha \approx U \sin\theta \tag{3. 27}$$

where U is an arbitrary number.

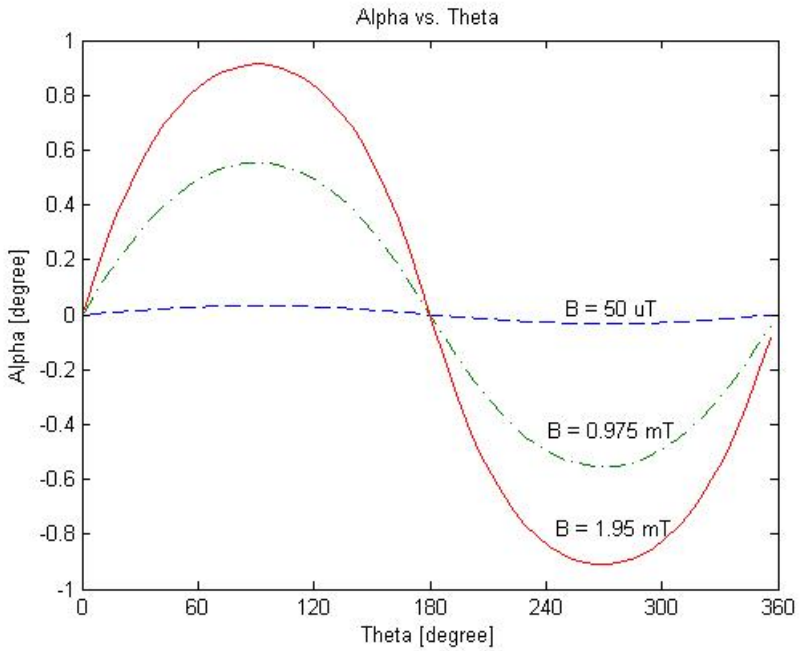

Figure 3. 8. Variation of the equilibrium angle according to the direction of the external magnetic field with 50 μT, 0.975 mT, and 1.95 mT respectively. Torques associated with these fields are calculated from Equation (3. 12).

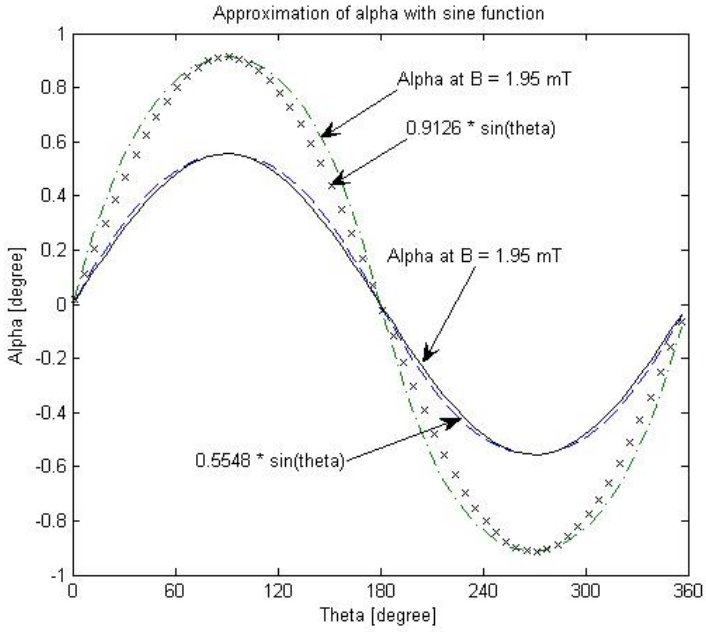

Figure 3. 9. An approximation of the α with arbitrary *sine* function.

Once the k_l, k_{nl}, and α are found, the resonant frequency is calculated using Equation (3. 18). The change of resonant frequency of the magnetic field sensor according to the direction of the external magnetic field is shown in Figure 3. 10. The resulting frequency curve is matched with the shape of α^2 as shown in Figure 3. 9. Therefore the sensitivity is mainly determined by the product of k_{nl} and α^2 as shown in Equation (3. 18).

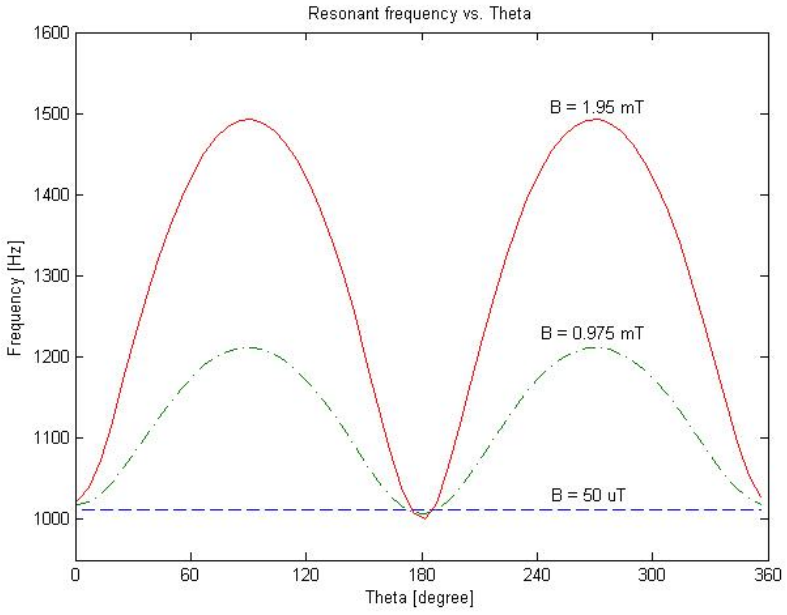

Figure 3. 10. Variation of the resonant frequency according to the direction of the magnetic field.

In order to maximize the sensitivity, defined with units as Hz/degree, it is required to maximize not only k_{nl}, but also α at a given torque (Equation 3. 18). Equation (3. 27) shows that the k_l needs to be minimized to maximize an α at a given torque. Therefore,

minimizing k_l and maximizing k_{nl} is suggested to achieve the maximum sensitivity. Minimizing the k_l can be achieved by either increasing the length of the beam or reducing the width of the beam. In both cases, the mechanical resonator is becoming more brittle to shocks and vibrations and can be easily broken. There is another concern with minimizing k_l. Lowering the value of k_l results in lower resonant frequencies which make the electrical measurements difficult due to low frequency noise.

3.2 Characterization using theory

In this section, the sensitivity of the resonator is characterized by varying the width of the beam and the number of beams. This characterization gives a path toward an optimum design to achieve the maximum sensitivity.

3.2.1 Beam width characterization

In this section, the sensitivity of the resonator is characterized by varying the width of the beams. The sensitivity is defined as the amount the resonant frequency changes over unit angle (θ) difference. Three different beam widths of 10, 20 and 30 μm are used for this characterization. All other parameters are listed in Table 3. 1. The simulation follows the steps illustrated in Figure 3. 11. The graphs of the deflection *vs* force are plotted using Equations (3. 19 ~ 3. 23) which correspond to the 10, 20, and 30 μm in beam width, respectively (Figure 3. 12). The lateral stiffness of the beams, $k_{\delta,l}$ and $k_{\delta,nl}$, are calculated from Figure 3. 13. The torsional stiffness of the beams, k_l and k_{nl}, are found using Equations (3. 24 ~ 3. 26). Once the k_l and k_{nl} are determined, α is calculated as a

function of θ using Equation (3. 15). The resonant frequency can be determined using Equation (3. 18).

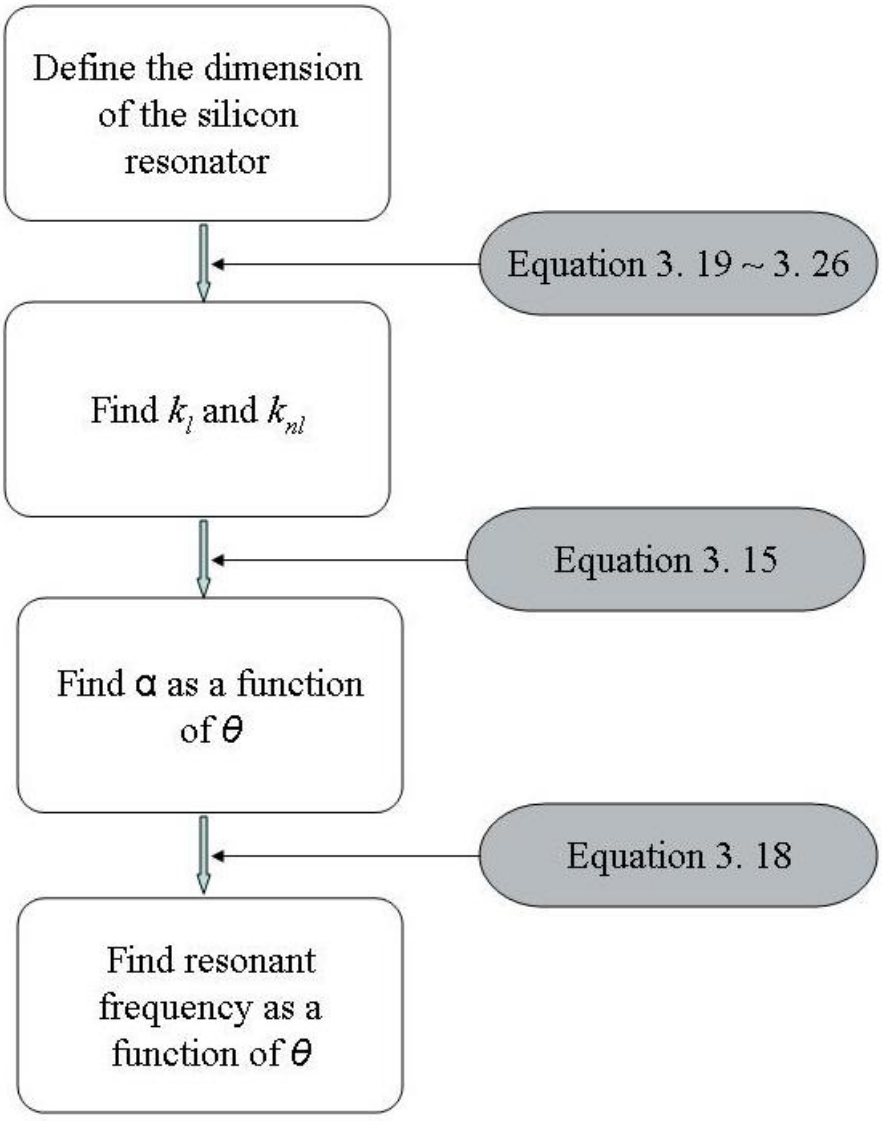

Figure 3. 11. The numerical simulation sequences.

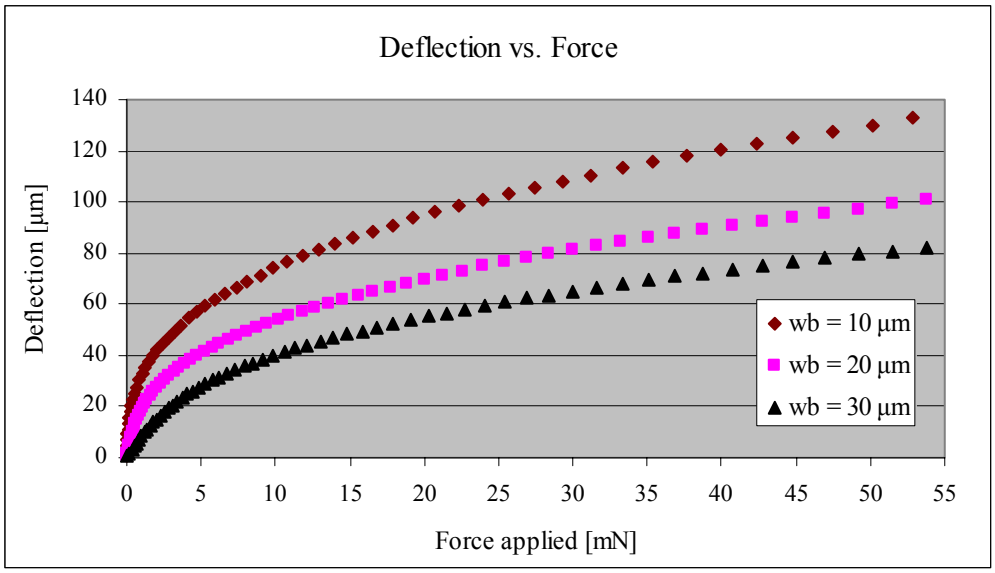

Figure 3. 12. Deflection to force curves calculated for 10, 20 and 30 µm in beam width.

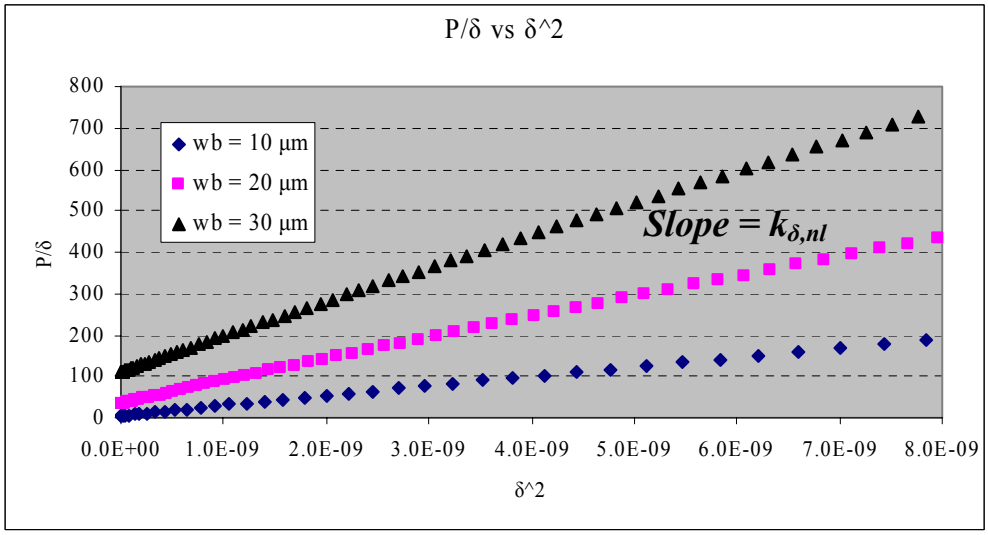

Figure 3. 13. P/δ vs. δ^2 curves for the three different beam widths. A $k_{\delta,l}$ is the cross section of the curves with y axis and $k_{\delta,nl}$ is the slope of the curves. The total system stiffness is calculated using Equation (3. 26).

Table 3. 2. Simulation results with varying beam width. Note that the number of beams is already considered for calculating the k_l and k_{nl} (Equation 3. 26). All other parameters are listed in Table 3. 1.

Beam width	k_l [10^{-6} Nm]	k_{nl} [10^{-2} Nm]	Resonant frequency *at* $\theta=0°$. f_c [Hz]	$\Delta f_c/(f_c \cdot$ degree) [10^{-3} Hz/(Hz·degree)]		
				50 μT	0.975 mT	1.95 mT
10 μm	16.56	9.12	358.3	1.5	21.5	27.8
20 μm	132.13	18.70	1009.4	0.0112	2.0	4.88
30 μm	445.48	31.60	1853.5	0.00094	0.11	0.44

The numerical values of the k_l and k_{nl} are listed in Table 3. 2 along with resonant frequencies and the normalized sensitivities evaluated at 50 μT, 0.975 mT, and 1.95 mT of the external magnetic field for the three different beam widths, respectively. As the beam width increases, both the linear and nonlinear stiffness increase as well. The increasing rate of the nonlinear stiffness, k_{nl}, is not as high as compared to the rate of linear stiffness, k_l. The resonant frequency evaluated at $\theta = 0°$ also increases as the linear stiffness increases. A normalized sensitivity is the sensitivity whose value is divided by the resonant frequency at $\theta = 0°$.

As shown in Equation (3. 18), the resonant frequency is determined by four terms, i.e., k_l, $3k_{nl}\cdot\alpha^2$, $T_0\cdot cos(\theta - \alpha)$, and the second moment of inertia, I. Among them, $k_{nl}\cdot\alpha^2$ and $T_0\cdot cos(\theta - \alpha)$ play key roles in determining not only the shape of the resonant frequency, but also the sensitivity. If the $k_{nl}\cdot\alpha^2$ is larger than $T_0\cdot cos(\theta - \alpha)$, then the resonant frequency curve is similar in shape to the *sine* squared function (section 3.2.1.1) as shown

in Equation (3. 27). However, if the $T_0 \cdot cos(\theta-\alpha)$ is larger than $k_{nl} \cdot \alpha^2$, then the resonant frequency curve follows the shape of the *cosine* function (section 3.2.1.2). The magnitude of the $k_{nl} \cdot \alpha^2$ term can be adjusted by changing the structural dimensions (for example, changing the beam width).

3.2.1.1 CASE 1: $k_{nl} \cdot \alpha^2$ is larger than $T_0 \cdot cos(\theta - \alpha)$

The simulation results for this case are listed in Table 3. 2 (gray background). The numerical values of the $3k_{nl} \cdot \alpha^2$ and $T_0 \cdot cos(\theta - \alpha)$ for the 10 μm beam width are plotted in Figure 3. 14 (a – c) which show larger magnitude for the $3k_{nl} \cdot \alpha^2$ term as compared to the $T_0 \cdot cos(\theta - \alpha)$ term at all external magnetic field values of 50 μT, 0.975 mT, and 1.95 mT, respectively. The comparison results for the 10 μm and 20 μm beam width are plotted in Figure 3. 14 (d – g) which show larger magnitude for the $3k_{nl} \cdot \alpha^2$ term compared to $T_0 \cdot cos(\theta - \alpha)$ term at the external magnetic field values of 0.975 mT and 1.95 mT, respectively. The magnitudes of the term $3k_{nl} \cdot \alpha^2$ are larger than the term $T_0 \cdot cos(\theta - \alpha)$ by at least one order of magnitude (Figure 3. 14 (a) – (g)). In this case, the resonant frequency is determined mostly by $3k_{nl} \cdot \alpha^2$ term. Even though the nonlinear stiffness increases as the beam width increases, the product of the k_{nl} and α^2 decrease as the beam width increases since the decreasing rate of the α^2 is faster than the increasing rate of the k_{nl} (Figure 3. 15). Therefore, the normalized sensitivity decreases as the beam width increases which means that the normalized sensitivity is highest for a 10 μm beam width. The resonant frequency curve is similar in shape to the *sine* squared function as shown in the previous section (Figure 3. 16 (a) – (f)). The normalized sensitivity increases with a

larger external magnetic field since the equilibrium angle, α, becomes larger with increasing external magnetic field at a given k_l and k_{nl} (Table 3. 2).

The condition for $k_{nl} \cdot \alpha^2$ to be larger than $T_0 \cdot cos(\theta - \alpha)$ can be achieved by making either k_{nl} or α sufficiently large enough such that $k_{nl}\ \alpha^2$ is an order of magnitude larger than $T_0 \cdot cos(\theta - \alpha)$. Increasing k_{nl} is not favorable since it is accompanied with increase in k_l which results in a decreased α (Table 3. 2). Therefore, increasing α is favorable since the $k_{nl} \cdot \alpha^2$ is proportional to the square of the α while it is proportional to just k_{nl}. The equilibrium angle, α, increases when either k_l decreases or T_0 increases (Equation 3. 15). The numerical value of T_0 is determined by the volume and the magnetization of the permanent magnet and also by the applied external magnetic field (Equation 3. 12). So in order to increase the torque T_0, it is required to increase either the volume or the magnetization of the permanent magnet at a given external magnetic field. The calculated values of the T_0 are 7.55 x 10^{-10}, 1.47 x 10^{-6}, and 2.94 x 10^{-6} for 50 μT, 0.975 mT, and 1.95 mT of the external magnetic fields, respectively.

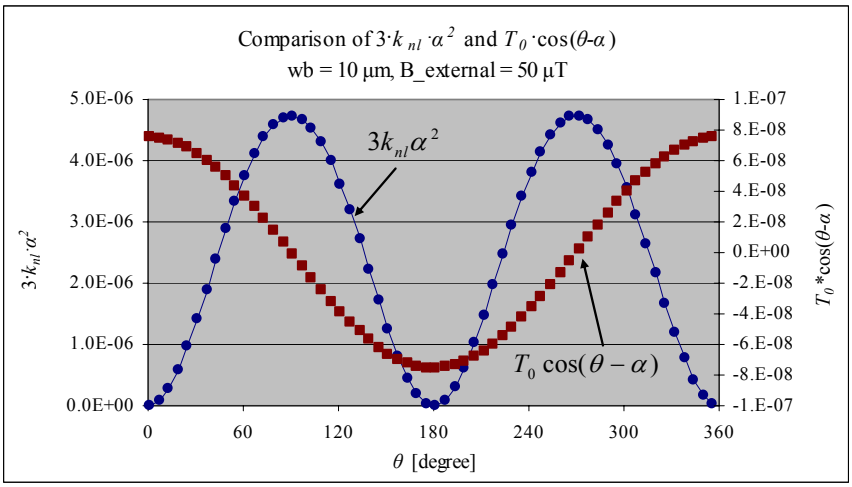

(a) Beam width is 10μm, External magnetic field is 50 μT.

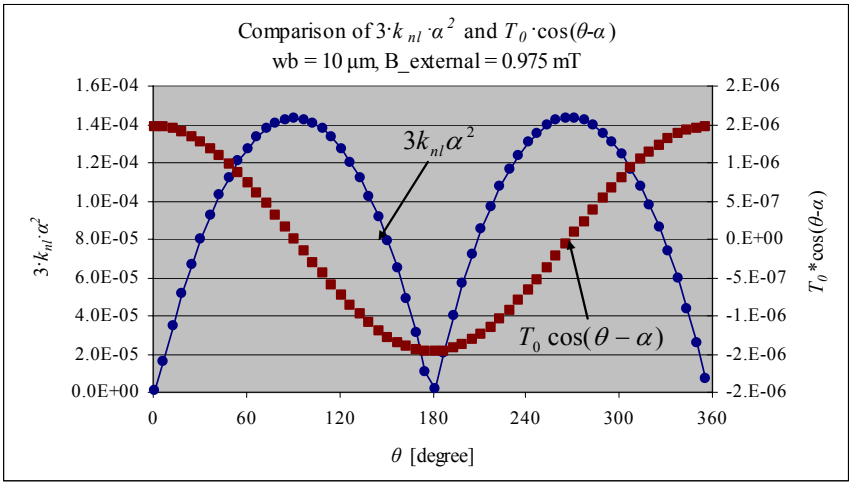

(b) Beam width is 10μm, External magnetic field is 0.975 μm.

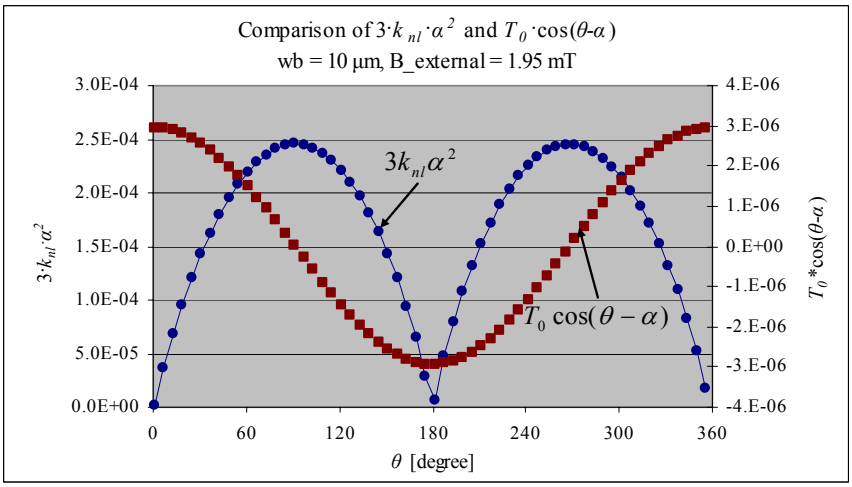

(c) Beam width is 10μm, External magnetic field is 1.95 mT.

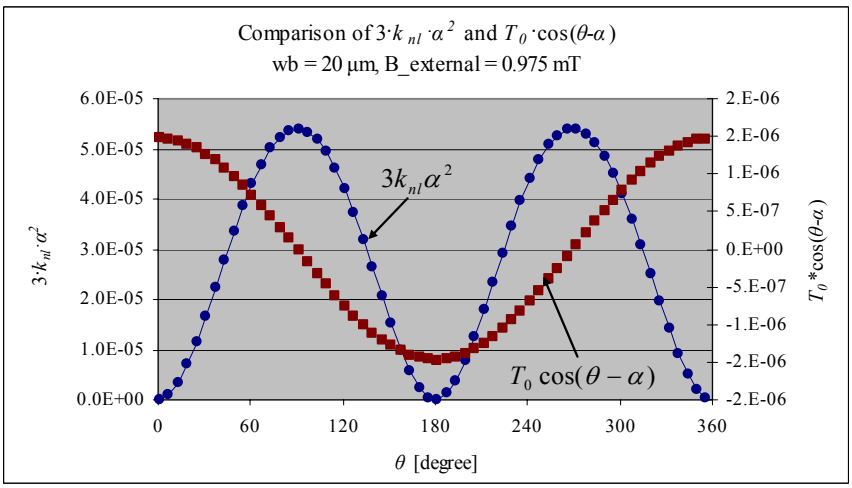

(d) Beam width is 20μm, External magnetic field is 0.975 mT.

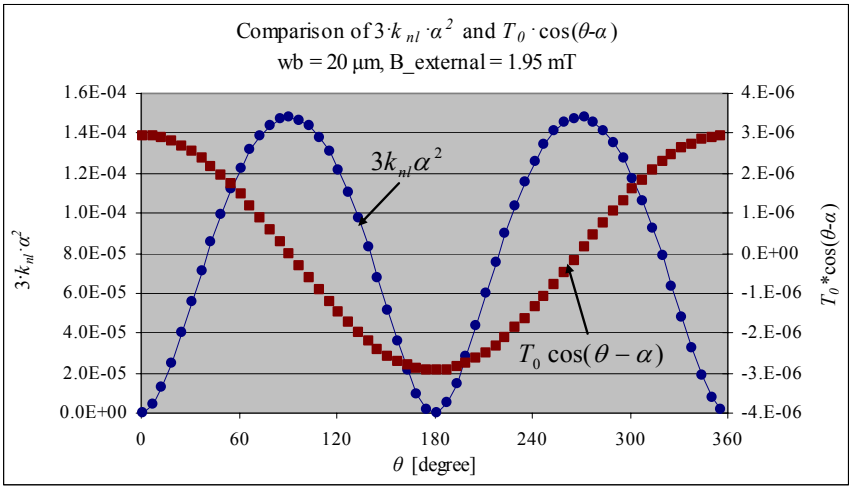

(e) Beam width is 20μm, External magnetic field is 1.95 mT.

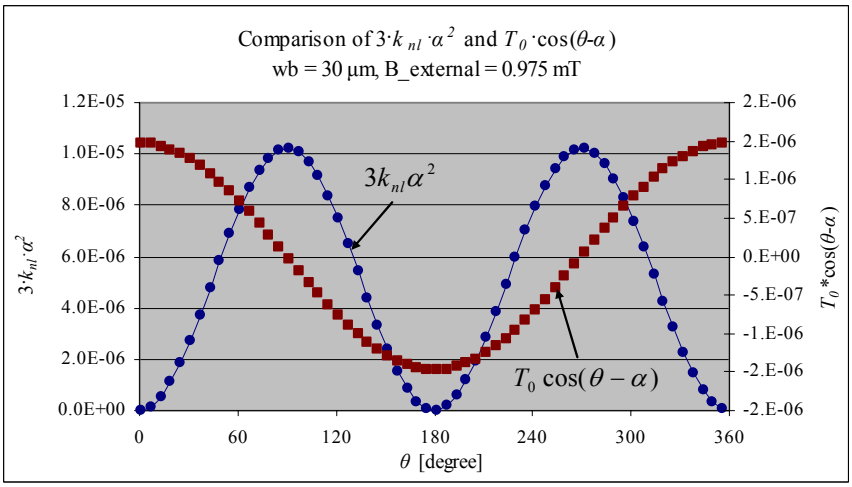

(f) Beam width is 30μm, External magnetic field is 1.95 mT.

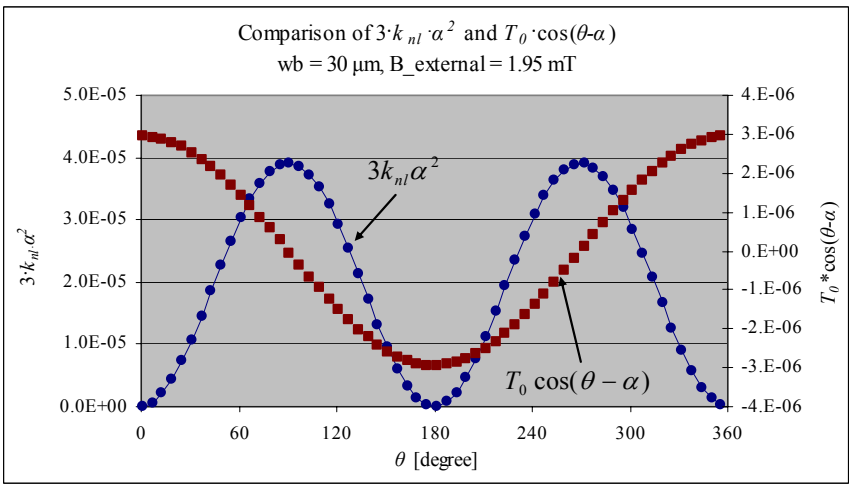

(g) Beam width is 30μm, External magnetic field is 1.95 mT.

Figure 3. 14. Comparisons of the $3k_{nl}\alpha^2$ and $T_0\cos(\theta-\alpha)$.

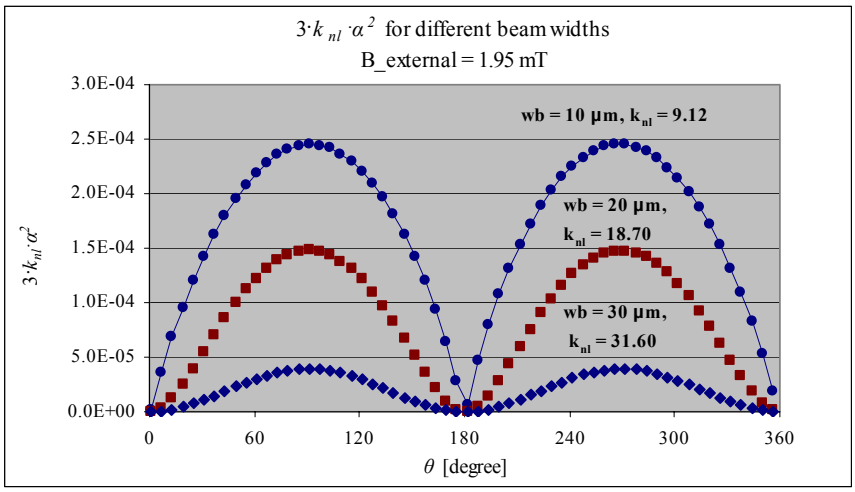

Figure 3. 15. $k_{nl}\cdot\alpha^2$ as a function of the θ for the 10, 20, and 30 µm beam widths. Note that the k_{nl} increases while the $k_{nl}\cdot\alpha^2$ decreases as the beam width increases

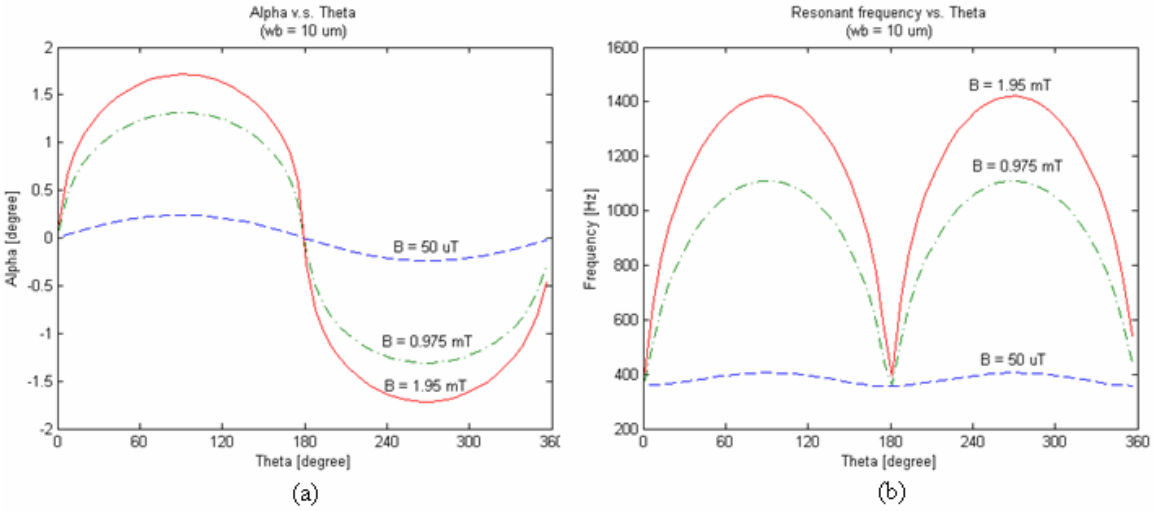

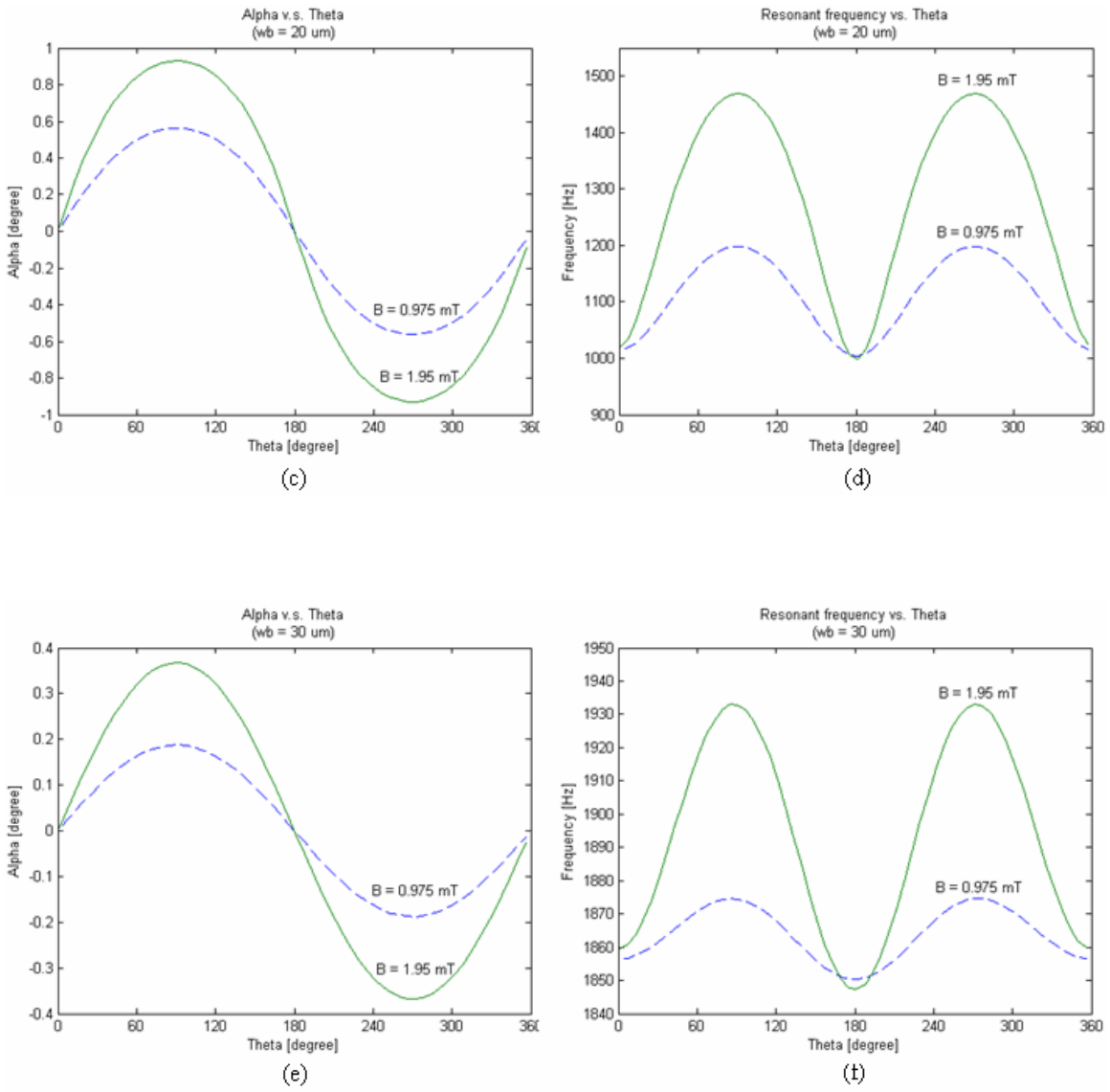

Figure 3. 16. An equilibrium angle ((a), (d), (e)) and the resonant frequency ((b), (d), (f)) as a function of θ. (a, b) Beam width 10 μm, (c, d) beam width 20 μm, (e, f) beam width 30 μm.

3.2.1.2 CASE 2: $k_{nl}\cdot\alpha^2$ is comparable to $T_0\cdot\cos(\theta - \alpha)$

The simulation result corresponding to this case is given in Table 3. 2 (20 μm beam width evaluated at 50 μT). The magnitudes of the $3k_{nl}\cdot\alpha^2$ and $T_0\cdot\cos(\theta - \alpha)$ are in the same order as shown in Figure 3. 17. The resulting resonant frequency profile is in transition from a *cosine* to a *sine* squared shape (Figure 3.18).

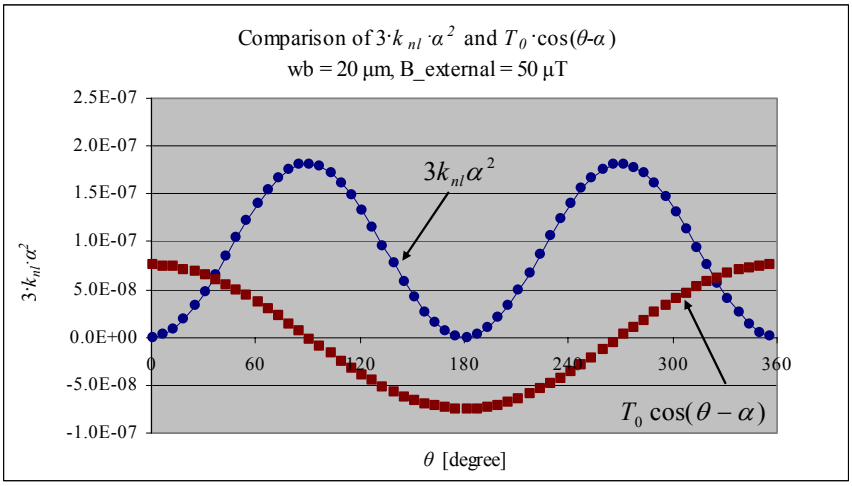

Figure 3. 17. Comparisons of the $3k_{nl}\alpha^2$ and $T_0\cdot\cos(\theta-\alpha)$ for the beam width of 20 μm evaluated at 50 μT. Note that the$3k_{nl}\alpha^2$ is comparable to $T_0\cdot\cos(\theta-\alpha)$ in magnitude.

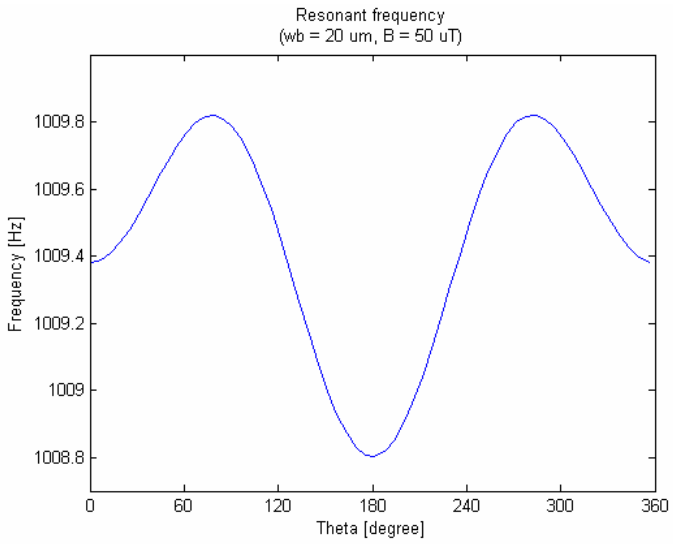

Figure 3. 18. Resonant frequency as a function of theta. Note that the profile of the resonant frequency is in transition from *cosine* to the *sine* squared function in shape.

3.2.1.3 CASE 3: $T_0 \cdot cos(\theta - \alpha)$ is larger than $k_{nl} \cdot \alpha^2$

The simulation result corresponding to this case is given in Table 3. 2 (30 μm beam width evaluated at 50 μT). The magnitude of the $3k_{nl} \cdot \alpha^2$ and $T_0 \cdot cos(\theta - \alpha)$ is compared in Figure 3. 19 which shows the term $T_0 \cdot cos(\theta - \alpha)$ being larger than $3k_{nl} \cdot \alpha^2$ by at least one order of magnitude. In this case, the resonant frequency profile is determined mostly by the $T_0 \cdot cos(\theta - \alpha)$. The numerical value of α is the only parameter in the term $T_0 \cdot cos(\theta - \alpha)$ which is affected by the beam width variation. It is negligible in this case since the rotating torque from a field with a value 50 μT is too small to generate a value of α that is comparable with the value of θ. Therefore, $T_0 \cdot cos(\theta - \alpha)$ is almost identical for the different beam widths (Figure 3. 20). The resonant frequency can be modeled using k_l, T_0, and I whose expression is identical to the Equation (3. 13) of the linear modeling section (Equation 3. 28):

$$f_0 = \frac{1}{2\pi}\sqrt{\frac{k_l + 3k_{nl}\alpha^2 + T_0\cos(\theta-\alpha)}{I}}$$

$$\Rightarrow \quad f_0 \cong \frac{1}{2\pi}\sqrt{\frac{k_l + T_0\cos(\theta)}{I}} \qquad (3.\ 28)$$

The resonant frequency curve is similar in shape to a *cosine* function (Figure 3. 21 (a, b)). The normalized sensitivity is very small comparing to the first case (Table 3. 2).

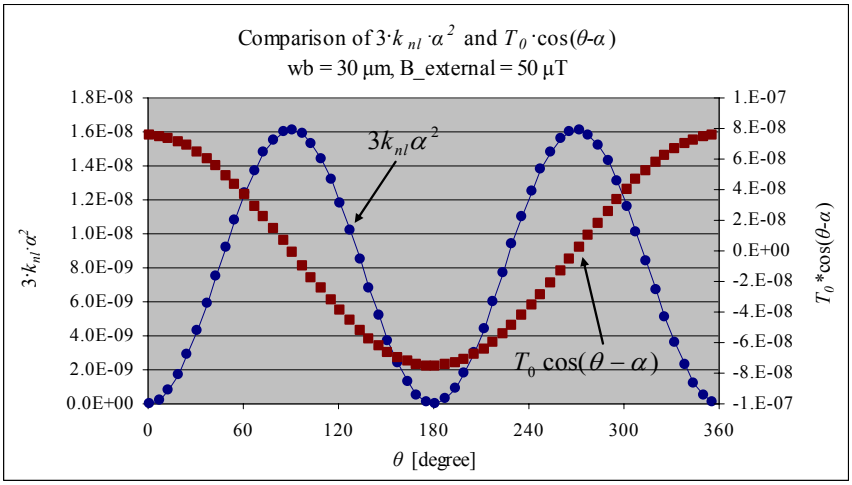

Figure 3. 19. Comparisons of the $3k_{nl}\alpha^2$ and $T_0\cdot\cos(\theta-\alpha)$. The beam width is 30μm and an external magnetic field is 50 μT. Note that the $T_0\cdot\cos(\theta-\alpha)$ is larger than $3k_{nl}\alpha^2$ in magnitude at least by more than one order.

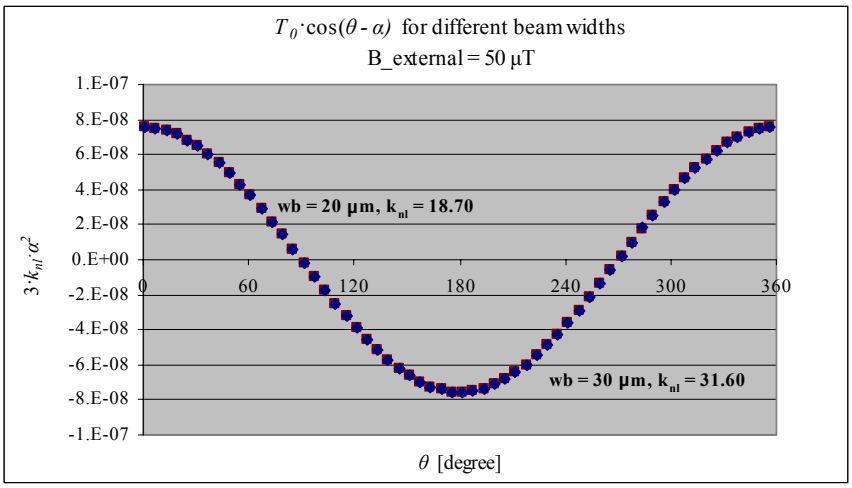

Figure 3. 20 $T_0 \cdot cos(\theta-\alpha)$ as a function of the θ for the 20 and 30 μm beam widths calculated at the external magnetic field of the 50 μT. Note that the $T_0 \cdot cos(\theta-\alpha)$ is identical for both beams.

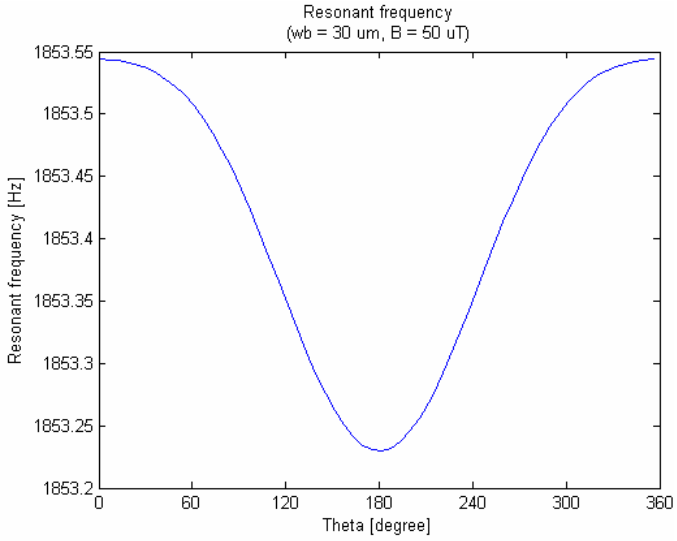

Figure 3. 21. Resonant frequency as a function of theta. A beam width is 30 μm and an external magnetic field is 50 μT. Note that the profile of the resonant frequency is similar to a *cosine* function in shape.

The condition for $T_0 \cdot cos(\theta - \alpha)$ to be larger than $k_{nl} \cdot \alpha^2$ can be achieved by making either k_{nl} or α sufficiently small enough such that the term $k_{nl}\ \alpha^2$ is an order of magnitude smaller than the term $T_0 \cdot cos(\theta - \alpha)$. As was stated in case 1, value of $k_{nl}\ \alpha^2$ is more sensitive to the magnitude of α than to that of k_{nl}. The numerical value of α can be reduced either by decreasing the applied torque at a given beam width, or by increasing beam width at a given torque, *i.e*., given external magnetic field (Equation 3. 15). By decreasing the applied external magnetic field from 0.975 mT to 50 μT, the resonant frequency is more dependent on the value of $T_0 \cdot cos(\theta - \alpha)$ rather than $k_{nl}\ \alpha^2$. By increasing the beam width from 10 μm to 30 μm at an external magnetic field of 50 μT, the profile of the resonant frequency changes from a *sine* squared function to a *cosine* function which shows the same results as in the case of decreasing the applied external magnetic field at the same beam width.

The dependence of the resonant frequency on either $k_{nl}\ \alpha^2$ or $T_0 \cdot cos(\theta - \alpha)$ is simulated by changing the beam width from 10 μm to 100 μm at the external magnetic field of 1. 95 mT (Table 3. 3). To investigate the transition, the maximum value of the $3 \cdot k_{nl} \cdot \alpha^2$ is calculated to compare it with the magnitude of the $T_0 \cdot cos(\theta - \alpha)$. The numerical value of the $T_0 \cdot cos(\theta - \alpha)$ depends on externally applied torque, but not the beam width variations as was discussed in previous sections. As shown in Table 3. 3, the nonlinear stiffness (k_{nl}) increases as the beam width increases, but the maximum value of the $3 \cdot k_{nl} \cdot \alpha^2$ decreases as the beam width increases since the value of the α is getting smaller with wider beam widths. In this simulation, $T_0 \cdot cos(\theta - \alpha)$ is the dominant term starting from 40 μm beam widths in determining both the sensitivity and the shape of the resonant frequency curve.

Figure 3. 22 shows the shapes of $k_{nl}\cdot\alpha^2$ and $T_0\cdot cos(\theta-\alpha)$ as a function of theta (θ) when the beam width is 100 μm, and the external magnetic field is 1.95 mT. $T_0\cdot cos(\theta-\alpha)$ is one order of magnitude larger than $k_{nl}\cdot\alpha^2$. Therefore the resonant frequency curve mostly depends on the $T_0\cdot cos(\theta-\alpha)$ (Figure 3. 23).

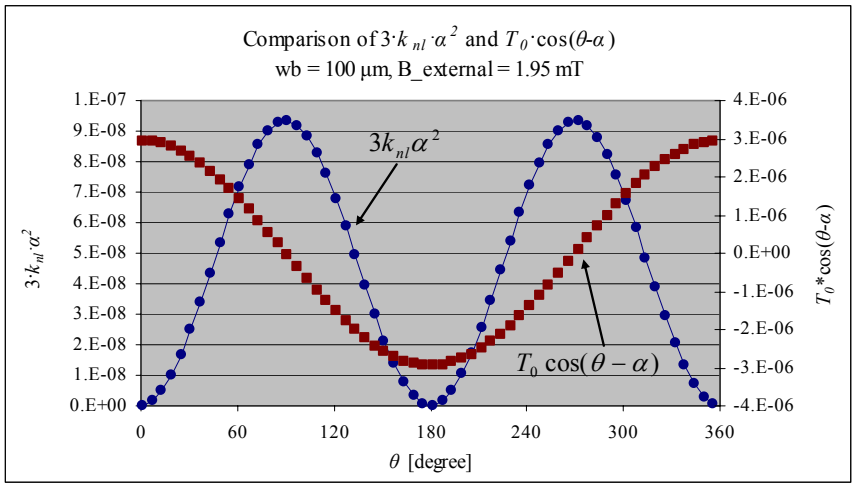

Figure 3. 22. Magnitude comparison of the $k_{nl}\cdot\alpha^2$ and $T_0\cdot cos(\theta-\alpha)$ for the 100 μm beam width and the external magnetic field of 1.95 mT.

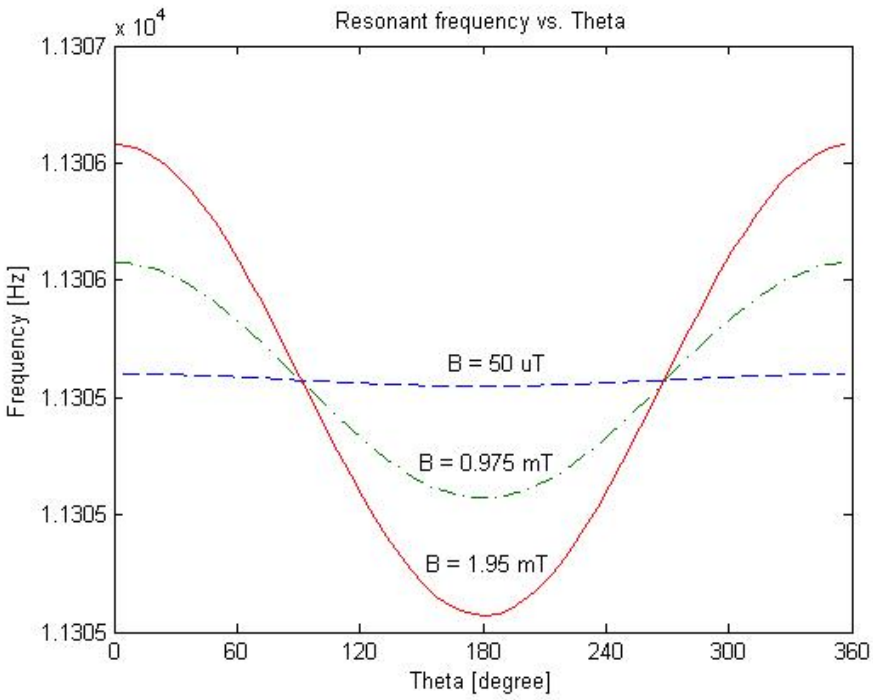

Figure 3. 23. Resonant frequency vs. theta curve. Note that the beam width is 100um and other dimensions are listed in Table 3. 1.

Table 3. 3. Comparison of the magnitudes of the $k_{nl}\cdot\alpha^2$ and $T_0\cdot cos(\theta-\alpha)$ at 1.95 mT.

Beam width [μm]	k_l (x 10^{-6})	k_{nl} (x 10^{-2})	Max($3\cdot k_{nl}\cdot\alpha^2$) (x 10^{-6})	$T_0\cdot\cos(\theta-\alpha)$ (x 10^{-6})	Sensitivity $\Delta f_c/(f_c\cdot$ degree)
10	16.56	9.12	244	2.94	$27.8\cdot10^{-3}$
20	132.13	18.70	147.8	2.94	$4.88\cdot10^{-3}$
30	445.48	31.60	39.09	2.94	$4.4\cdot10^{-4}$
40	1054.76	39.24	9.12	2.94	$3.36\cdot10^{-5}$
50	2063.8	49.2	3.00	2.94	$7.93\cdot10^{-6}$
60	3563.4	59.2	1.21	2.94	$4.59\cdot10^{-6}$
70	5655.24	68.8	0.56	2.94	$2.89\cdot10^{-6}$
80	8450.88	78.8	0.29	2.94	$1.93\cdot10^{-6}$
90	12026.48	88.4	0.16	2.94	$1.36\cdot10^{-6}$
100	16576	98.4	0.09	2.94	$9.87\cdot10^{-7}$

3.2.2 Beam width and number of beams characterization

In the previous sub-sections, the sensitivity is characterized in terms of the variation in beam widths while the number of beams is kept constant at 4. It is recommended that the linear torsional stiffness, k_l, should be minimized to achieve maximum sensitivity. In this sub-section, the resonator is characterized to maximize the sensitivity at a given linear torsional stiffness by changing both the number of beams and the width of the beams simultaneously.

Comparing cases 1, 2, and 3 from the previous sub-sections, the sensitivity is maximized when the numerical value of the $k_{nl}\cdot\alpha^2$ is larger than that of the $T_0\cdot cos(\theta-\alpha)$.

This can be achieved by minimizing the linear torsional stiffness, k_l, thereby maximizing the equilibrium angle, α, at a given torque (Equation 3. 15, section 3. 2. 1. 1). The sensitivity will be further maximized if k_{nl} is maximized at a given k_l. This is achieved by narrowing down the beam width so that each beam undergoes more stress at a given deflection. The number of beams needs to be adjusted to maintain the same linear torsional stiffness. For example, the narrow width of beams, the more number of beams.

Three different geometries are used for this characterization in terms of the different combinations of the number of beams and the width of the beams (Figure 3. 24). The combinations are 20, 15.88, and 12.61 μm in beam width for 4, 8, and 16 beams, respectively.

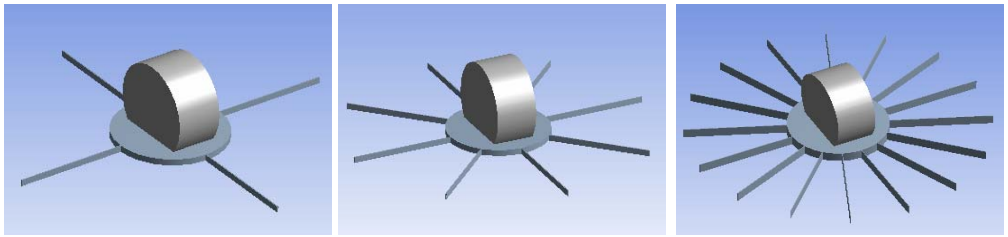

(a) (b) (c)

Figure 3. 24. Three different resonator geometries. (a) 3 beams, (b) 4 beams, and (c) 16 beams.

The deflection *vs* force curves are plotted for the three structures in Figure 3. 25 using the Equation (3. 19 – 3. 21). They are re-plotted in Figure 3. 26 to find the lateral linear and nonlinear stiffness coefficients of $k_{\delta,l}$ and $k_{\delta,nl}$. The torsional linear and

nonlinear stiffness coefficients of k_l and k_{nl} are calculated by multiplying the number of beams with the radius of the silicon center disk with $k_{\delta,l}$ and $k_{\delta,nl}$. (Equation 3. 26). The cross section of the curve with the y axis is corresponding to the $k_{\delta,l}$ while the slope of the curve is corresponding to the $k_{\delta,nl}$ (Figure 3. 26). Even though the lateral nonlinear stiffness coefficient, $k_{\delta,nl}$, decreases as the number of beams increase (Figure 3. 26), the numerical value of the converted k_{nl} increases as the number of beams increases in this simulation (Table 3. 4). The simulation results and the parameters are summarized in Table 3. 4.

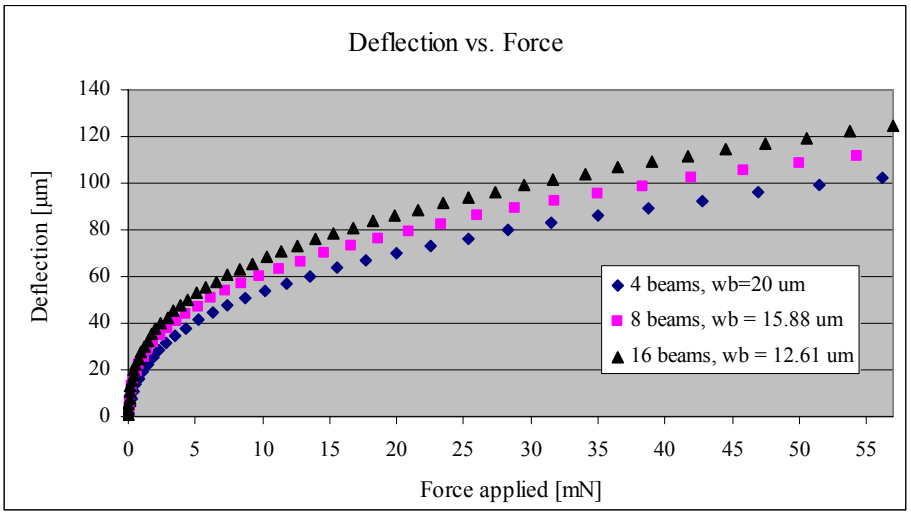

Figure 3. 25. Deflection *vs.* force curves for 4, 8, and 16 beam structures with 20, 15.88, and 12.61 µm in beam width, respectively.

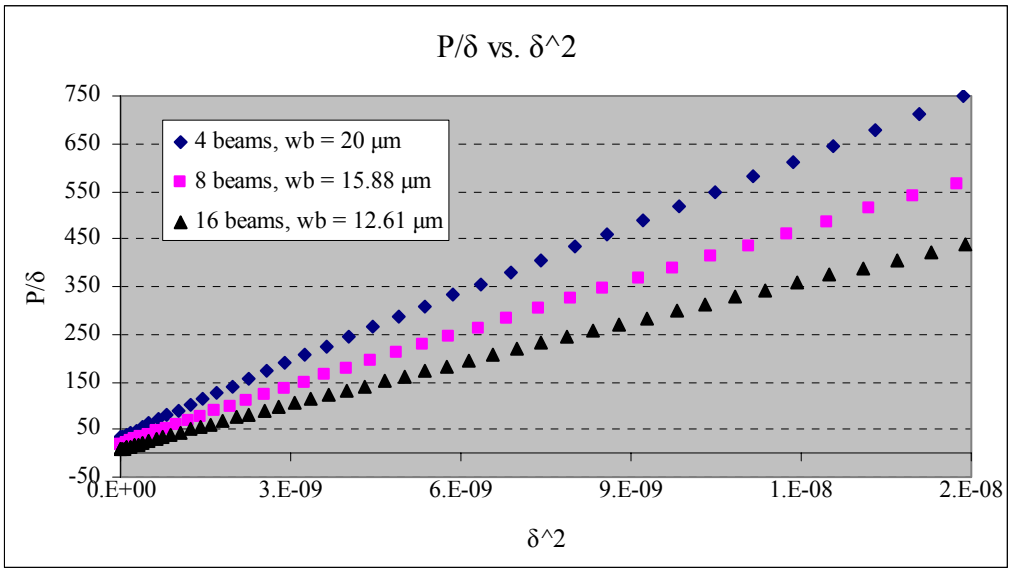

Figure 3. 26. *P/δ vs.* δ^2 curves to calculate the $k_{\delta,l}$ and $k_{\delta,nl}$. The cross section of the straight line with the y axis is the $k_{\delta,l}$, and the slope of the line is the $k_{\delta,nl}$.

Table 3. 4. Characterization of the beam width and the number of beams. Note that the number of beams is already considered for calculation of k_l and k_{nl}.

Number of beams	Width of beam [μm]	k_l [10^{-6} Nm]	k_{nl} [10^{-2} Nm]	Resonant frequency *at* $\theta=0°$. f_c [Hz]	Sensitivity $\Delta f_c/(f_c \cdot$ degree) [10^{-3} Hz/(Hz·degree)]		
					50 μT	0.975 mT	1.95 mT
4	20	132.13	18.7	1009.38	0.0112	2.001	4.879
8	15.88	132.28	29.1	1009.95	0.0153	2.756	6.157
16	12.61	132.47	46.2	1010.68	0.022	3.727	7.659

As shown in Table 3. 4, the torsional linear stiffness coefficients, k_l, are set to be very close for the three designs by reducing the beam width for the designs with more beams. The four beam structure with a 20 μm beam width shows the lowest k_l while the sixteen beam structure with a 12.61 μm beam width shows the highest numerical value for k_l. The resonant frequency of the four beam structure is lowest as expected due to its lowest linear stiffness coefficient. The torsional nonlinear stiffness coefficient, k_{nl}, increases as more beams are used. The numerical value of the α is inversely proportional to k_l. Therefore, it decreases as more beams are used at a given torque in this simulation. Figure 3. 27 (a) shows that the four beam structure has the highest magnitude of α while the sixteen beam structure has the lowest for a given value of θ. However, the sixteen beam structure shows the highest magnitude for $k_{nl} \cdot \alpha^2$ while the four beam structure shows the lowest value for a given θ since the magnitude of the k_{nl} is highest at the sixteen beam structure and eight, and four beam structure in that order (Figure 3. 27 (b)). The resonant frequencies are evaluated at 50 μT, 0.975 mT, and 1.95 mT for three structures (Figure 3. 28 (a-c)). In this characterization, the concept of increasing sensitivity by increasing the nonlinear stiffness coefficient at a given linear stiffness is demonstrated. Increasing the nonlinear stiffness coefficient at a given linear stiffness coefficient is achieved by using thinner beams as more beams are used. The sensitivity is maximized in this way while keeping the linear stiffness the same (Table 3. 4). The value of the linear stiffness decreases as the beam width is reduced which causes following problems: 1) a brittle mechanical structure which is susceptible to environmental shocks, 2) complicated electronic measurement system to remove low frequency noise. The number of beams and the beam width characterization performed in this section shows

one way of avoiding these problems caused by using thinner beams. The weakness of this structure with thin beams is compensated by increasing the number of beams, thereby maintaining the same level of the mechanical stability. The fundamental natural frequency is not lowered for the same reason, *i.e.*, more beams with narrower beam width.

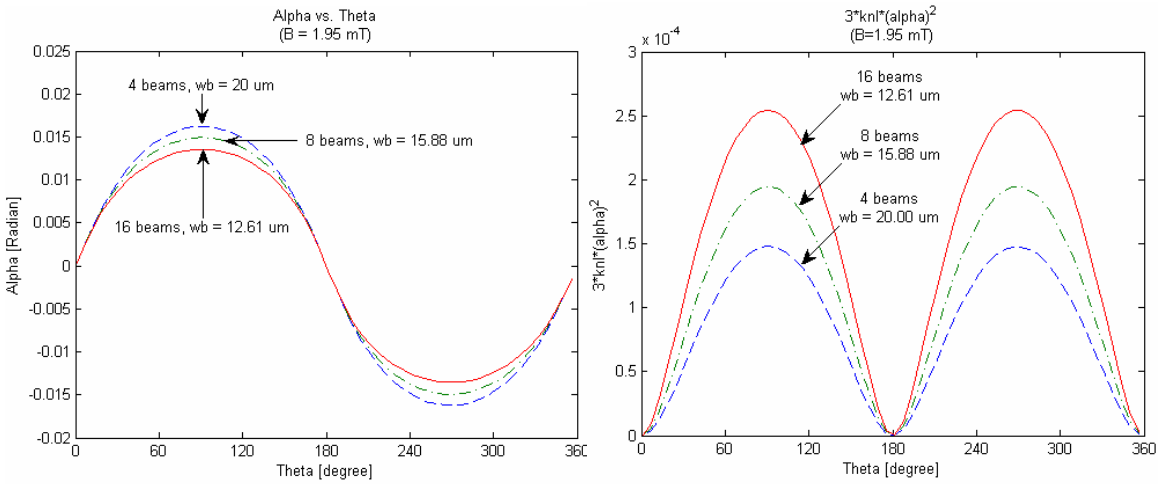

(a) (b)

Figure 3. 27. The equilibrium angle and torsional nonlinear stiffness coefficient comparison for the 4, 8, and 16 beam structures evaluated at the external magnetic field of 1.95 mT. (a) Comparison of the equilibrium angle. (b) Comparison of the $k_{nl} \cdot \alpha^2$.

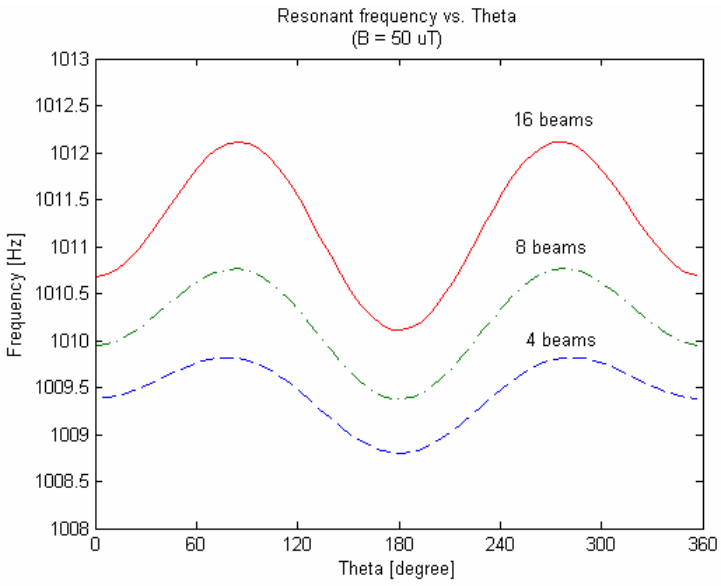

(a) Resonant frequencies at 50 μT.

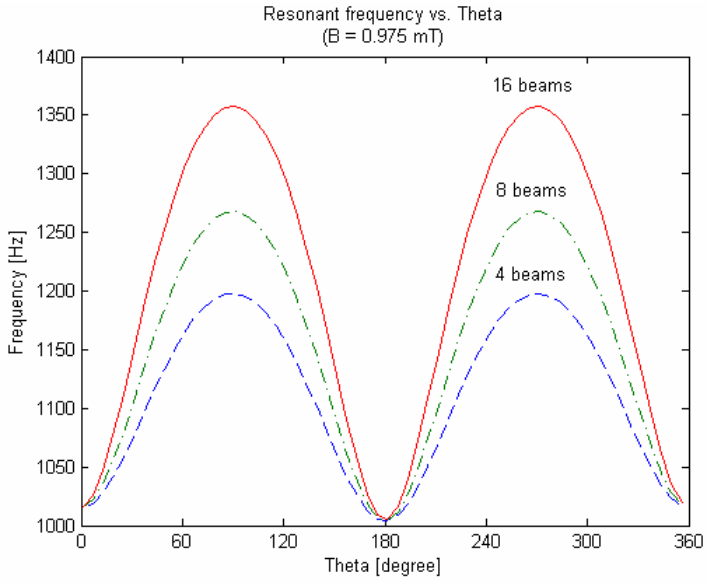

(b) Resonant frequencies at 0.975 mT.

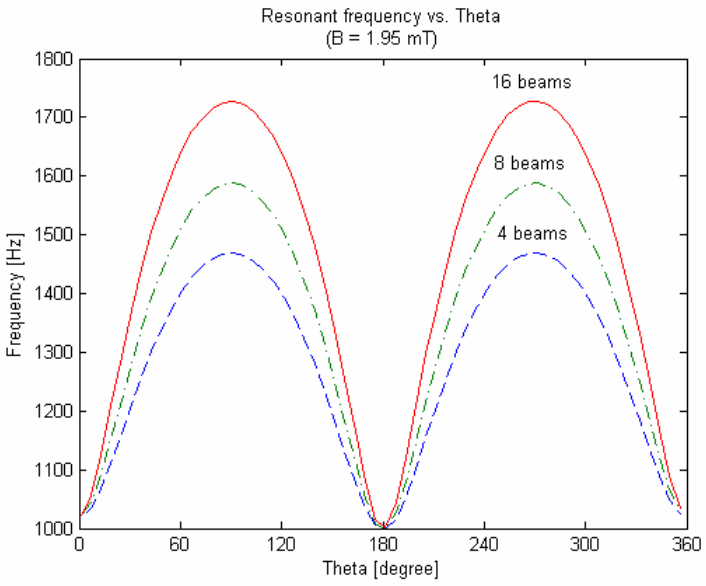

(c) Resonant frequencies at 1.95 mT

Figure 3. 28. Resonant frequencies for three different designs. (a) B = 50 μT, (b) B = 0.975 mT, and (c) B = 1.95 mT.

3.3 Characterization using Finite Element Method (FEM)

Finite Element Method (FEM) is used not only to provide verification of the theoretical modeling, but also to estimate the performance of the fabricated device. In this section, ANSYS (version 9.0, an academic edition) is used to perform the FEM simulation. The same characterizations are performed in this section which is corresponding to what are characterized in the Section 3. 1. The first characterization is about the performance of the resonator when the beam width changes while the number of beams is remained same. The second characterization is about the performance of the

resonator when both the beam width and the number of beams change while the linear stiffness coefficient is remained same.

The sequence of the simulation is shown in Figure 3. 29. Comparing to Figure 3. 11, the way to find k_l and k_{nl} is changed from the large deflection equations (Equations 3. 19 – 3. 21) to the FEM simulation using ANSYS.

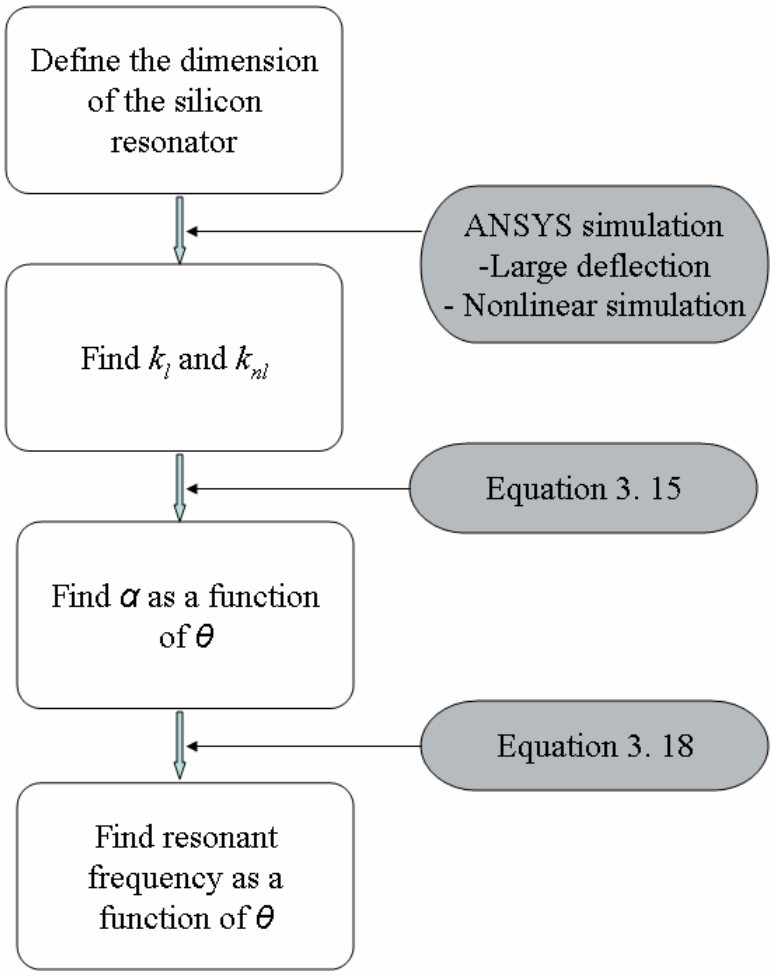

Figure 3. 29. Flowchart of the characterization using ANSYS.

A torque is applied as a form of force as shown in Figure 3. 30. The rotational angle is monitored and the torque-angle relation is plotted to find k_l and k_{nl}. The resonant frequency is calculated from the Equation (3. 18).

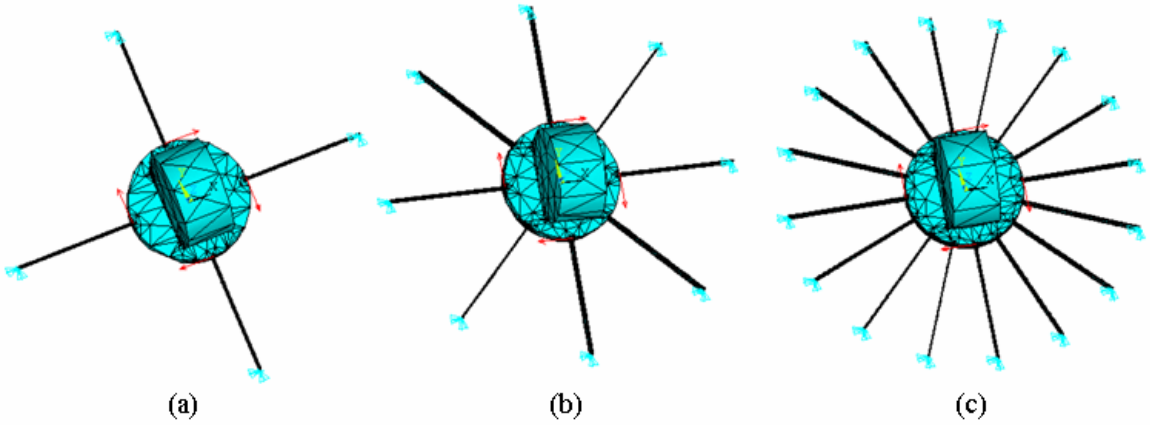

Figure 3. 30. Resonator model for the ANSYS simulation. The ends of the beam are confined and the torque is applied in the form of four forces on the center disk.

There are three different geometries in terms of the number of beams, i.e., four, eight, and sixteen, as shown in Figure 3. 30. Four beams structure is simulated with increasing beam width to characterize the effect of the beam width variations on the sensitivity of the resonator. The widths of the eight and sixteen beam structure are determined such that their linear stiffness coefficients are all equal to each other and to one of the four beam structures. Thereby the effect of the different number of beams whose linear stiffness is all the same is characterized. The dimensions of the resonator are

summarized in Table 3. 5. The primary resonant mode shapes are shown in Figure 3. 31 for the four, eight, and sixteen beam structures.

Table 3. 5. Structural dimensions used for the ANSYS simulation.

Number of beams	Beam width [μm]	Resonant frequency [Hz]	Mass moment of inertia [x 10^{-12}]
4	10	758.73	3.146
4	20	2103.20	3.327
4	30	3884.06	3.533
8	15.908	2106.45	3.345
16	12.675	2106.89	3.390

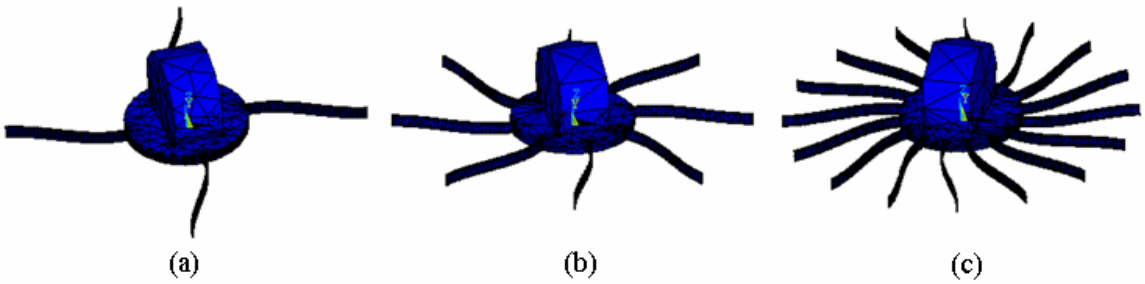

Figure 3. 31. The primary resonant mode shape for the resonators. (a) Four beam structure, (b) eight beam structure, and (c) sixteen beam structure.

3.3.1 Beam width characterization

The effect of the increasing or decreasing beam width at a given number of beams is characterized. The number of beams is four and the widths of beams are increasing from 10 μm to 30 μm by the 10 μm increment. All other parameters are listed in Table 3. 1. A nonlinear large deflection simulation is performed using ANSYS. A torque load is applied in the form of force in the ANSYS CLASSIC version as shown in Figure 3. 30. The rotational deflection, *i.e*., rotational angle, is recorded as the applied torque increases. The simulation follows the steps illustrated in Figure 3. 29. The graphs of the rotational angle, α, to applied torque are plotted for the four beam resonator structures of the 10, 20, and 30 μm in beam width, respectively (Figure 3. 32). The torque is related to the rotational angle, α, as

$$T = k_l \alpha + k_{nl} \alpha^3 \tag{3. 29}$$

$$\frac{T}{\alpha} = k_{nl} \alpha^2 + k_l \tag{3. 30}$$

The torsional linear stiffness, k_l, is the cross section value of the straight line whose slope is the torsional nonlinear stiffness, k_{nl}, in Figure 3. 33. Once the k_l and k_{nl} are determined, α is calculated as a function of θ using Equation (3. 15). The resonant frequency can be determined using Equation (3. 18).

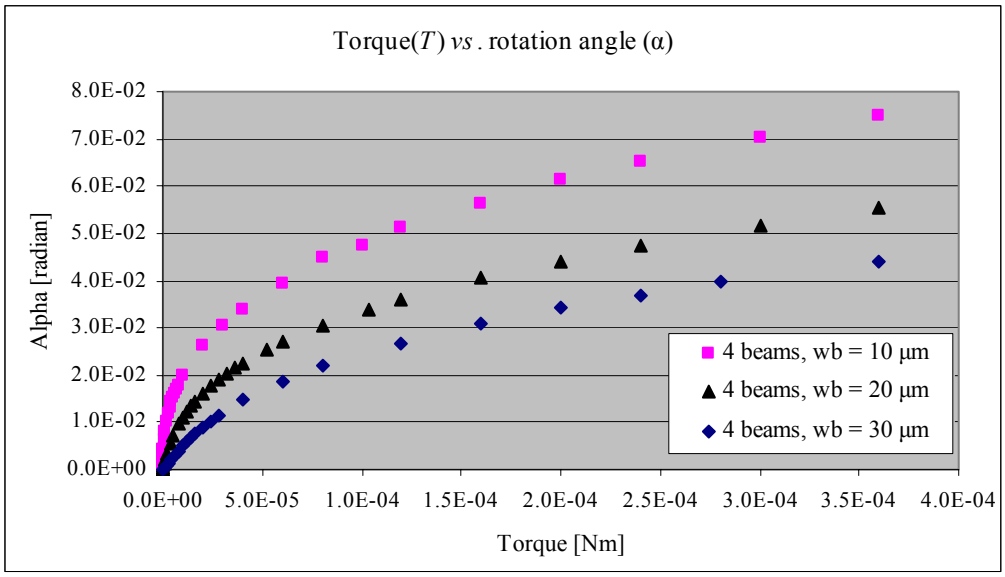

Figure 3. 32. A torque to rotational angle curves corresponding to the 10, 20, and 30 μm in beam width with four beams.

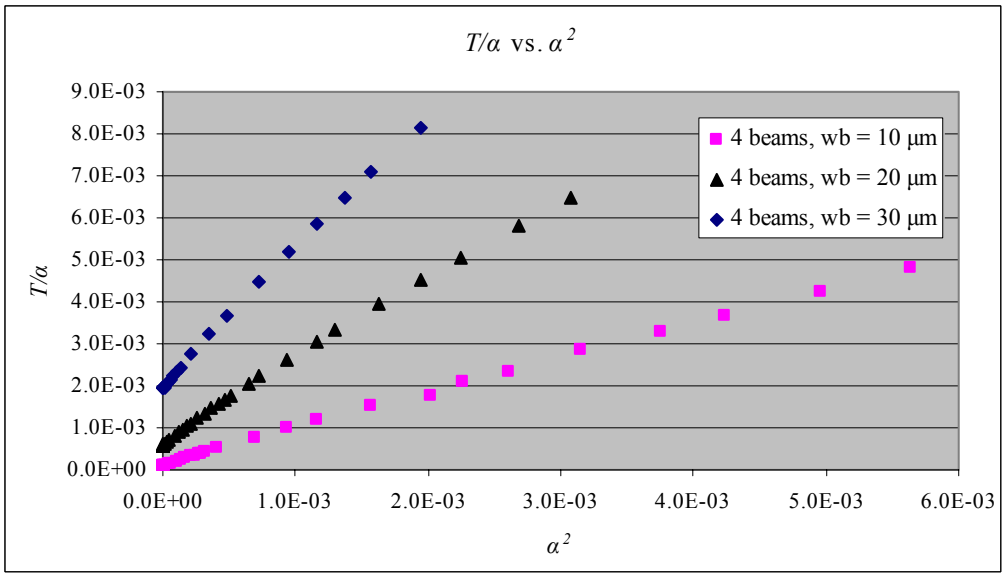

Figure 3. 33. T/α vs. α^2 curves for the three different beam widths. A k_l is the cross section of the curves with y axis and k_{nl} is the slope of the curves.

As the beam width increases, both the numerical values of the k_l and k_{nl} are increasing. The higher linear stiffness coefficient results in the higher resonant frequency and the small rotational angle at a given torque. The higher nonlinearity stiffness coefficient, k_{nl}, boosts up the value of the $k_{nl} \cdot \alpha^2$ in the Equation (3. 18). The shape of the resonant frequency curves depends on the relative magnitude of the two terms, $k_{nl} \cdot \alpha^2$ and $T_0 \cdot cos(\theta - \alpha)$ as is shown in the section 3. 2. 1. When the external magnetic field of 50 μT is used for simulation, the magnitude of the $k_{nl} \cdot \alpha^2$ is larger than the $T_0 \cdot cos(\theta - \alpha)$ for 10 μm, comparable for 20 μm, and smaller for 30 μm in beam width. Therefore, the shape of the resonant curves move from the *sine squared* function to *cosine* function as the beam width increase (Figure 3. 34 (a–c)).

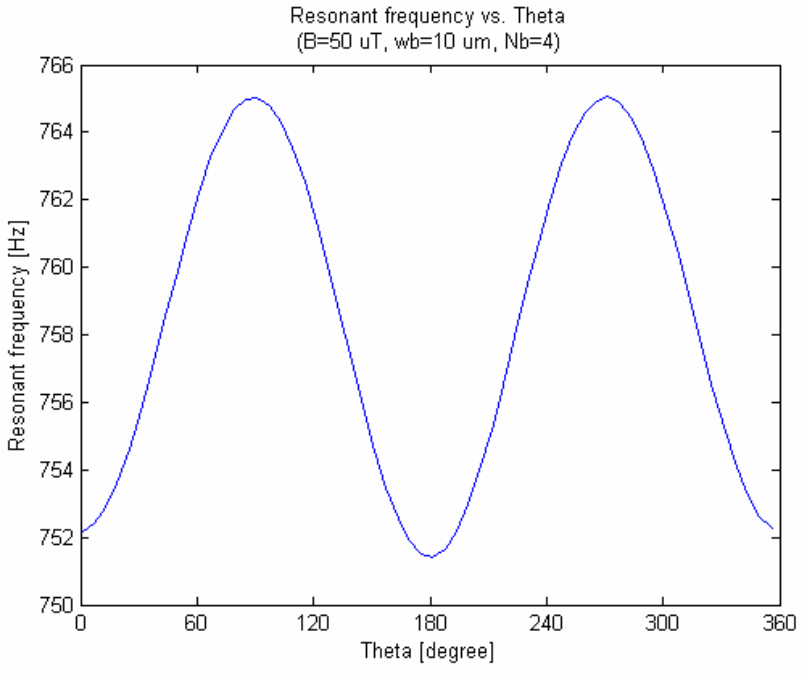

(a)

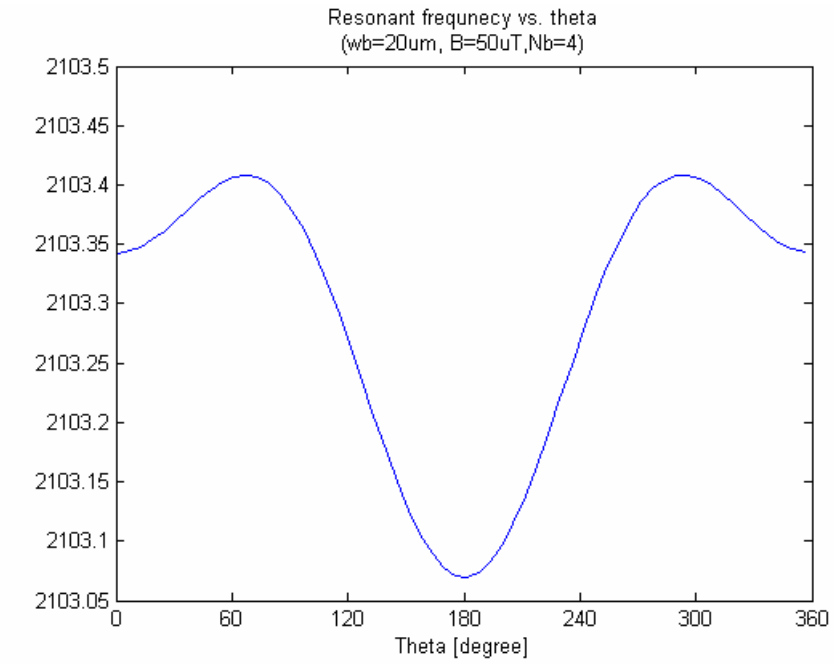

(b)

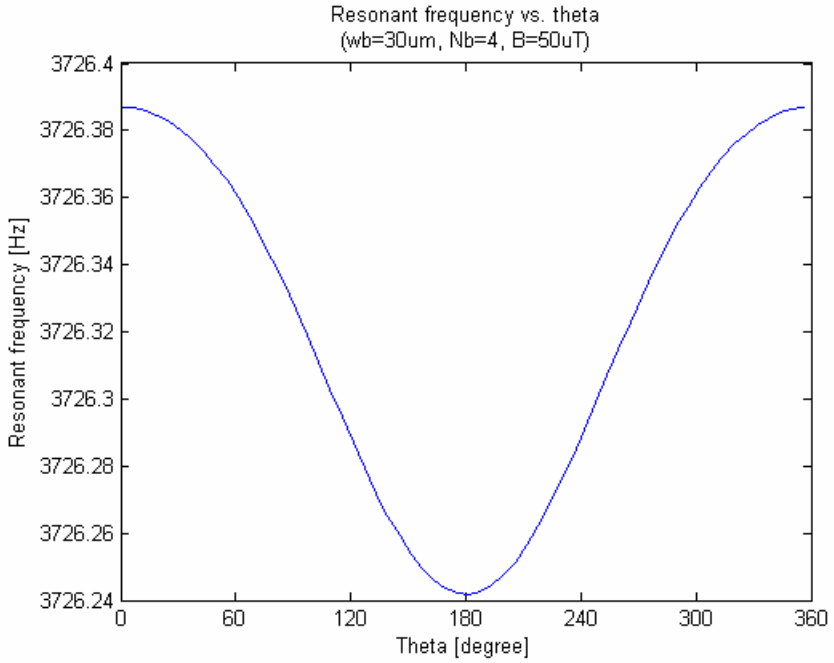

(c)

Figure 3. 34. Resonant frequency curves evaluated at 50 μT. (a) 10 μm beam width, (b) 20 μm beam width, and (c) 30 μm beam width.

When the external magnetic field of 0.975mT and 1.95 mT are used for the simulation, the all three cases show the larger magnitude of $k_{nl} \cdot \alpha^2$ compared to the $T_0 \cdot cos(\theta - \alpha)$. The resonant frequency curves follow the shape of the *sine squared* function (Figure 3. 35 (a-c)).

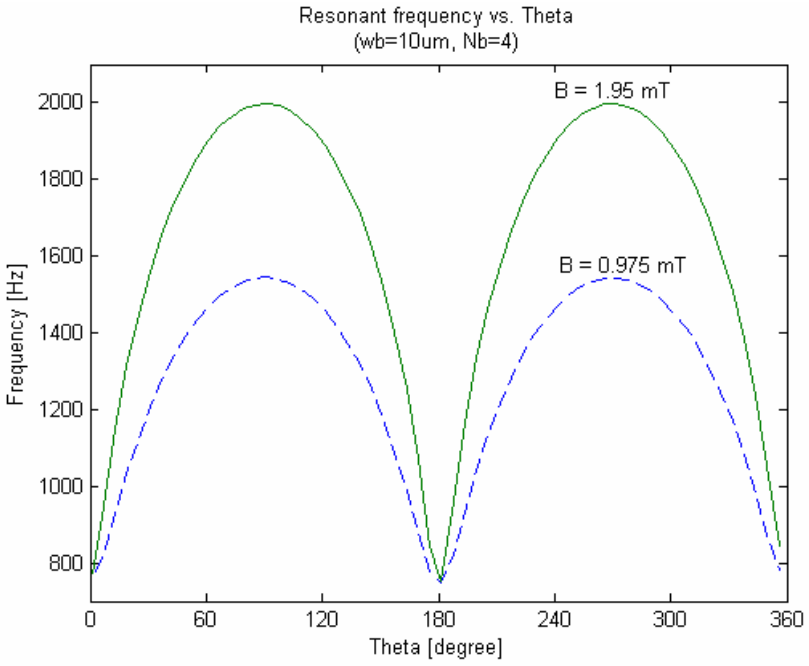

(a)

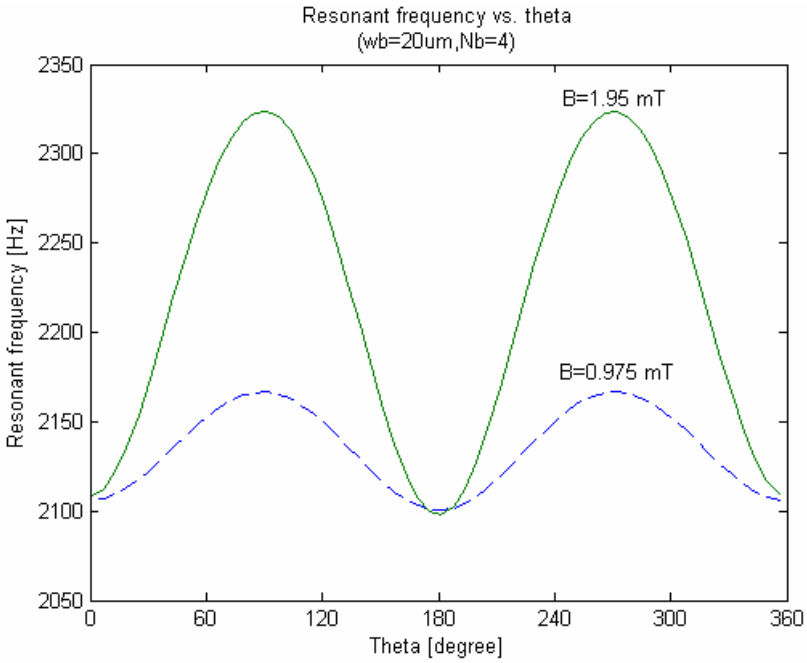

(b)

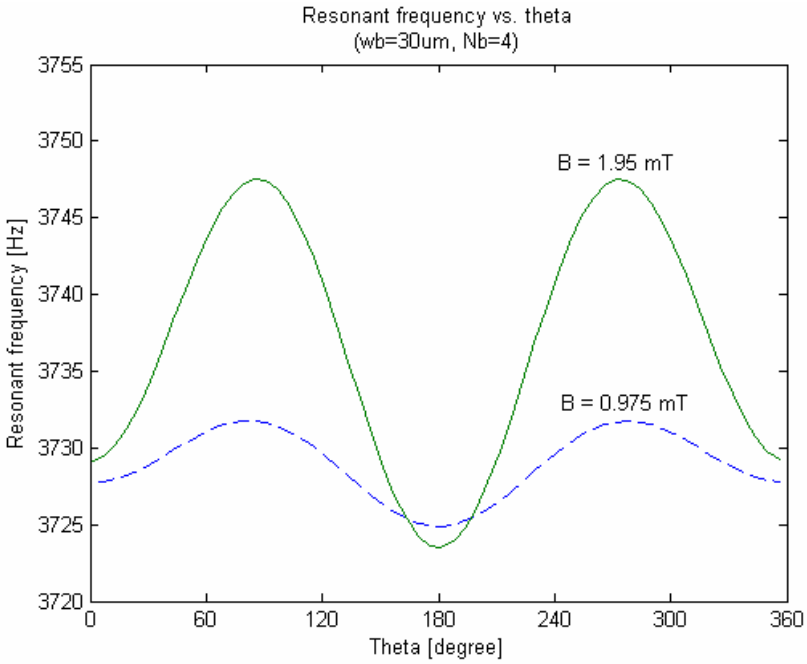

(c)

Figure 3. 35. Resonant frequency curves evaluated at 0.975 mT and 1.95 mT. (a) 10 μm beam width, (b) 20 μm beam width, and (c) 30 μm beam width.

Table 3. 6. A FEM simulation results with four beams structures. All other parameters are listed in Table 3. 1.

Beam width	k_l [10^{-6} Nm]	k_{nl} [10^{-2} Nm]	Resonant frequency *at* $\theta=0°$. f_c [Hz]	$\Delta f_c/(f_c \cdot$ degree) [10^{-3} Hz/(Hz·degree)]		
				50 μT	0.975 mT	1.95 mT
10 μm	73.3	83.8	758.73	0.10	11.44	17.63
20 μm	581.0	191.96	2103.2	0.0018	0.320	1.130
30 μm	1936.7	320.2	3884.06	0.00022	0.012	0.055

The simulation results with gray background in Table 3. 6 are corresponding to the case 1 of the section 3. 2. 1. in which the magnitude of the $k_{nl}\cdot\alpha^2$ is larger than that of the $T_0\cdot cos(\theta-\alpha)$ so that the resonant frequency curves are similar to the arbitrary *sine squared* function in shape (Figure 3. 34 (a), Figure 3. 35 (a-c)). The simulation results of the 20 μm in beam width evaluated at the external magnetic field of the 50 μT is corresponding to the case 2 of the section 3. 2. 1. in which the magnitude of the $k_{nl}\cdot\alpha^2$ is comparable to that of the $T_0\cdot cos(\theta-\alpha)$. The simulation results of the 30 μm in beam width evaluated at the external magnetic field of the 50 μT is corresponding to the case 3 of the section 3. 2. 1. in which the magnitude of the $k_{nl}\cdot\alpha^2$ is smaller than that of the $T_0\cdot cos(\theta-\alpha)$. The rate increase of the squared rotational angle (α^2) is greater then rate decrease of the k_{nl} as the beam width decreases. As a result, the product of $k_{nl}\cdot$and α^2 increase as the beam width decreases. Therefore, the normalized sensitivity increases at every external magnetic field tested as the beam width decreases (Table 3. 6). The FEM simulation using ANSYS is well matched with the characterization result using theory.

3.3.2 Beam width and number of beams characterization

In this section, the sensitivity is characterized in terms of both the variation of the beam width and the number of beams while the linear stiffness coefficient is remained same. The sensitivity is maximized at a given linear stiffness coefficient by increasing the nonlinearity of the resonator.

Three different geometries are used for this characterization in terms of the different combinations of the number of beams and the width of beam (Figure 3. 30). The structures are 20, 15.908, and 12.675 μm in beam width for 4, 8, and 16 beams, respectively. The width of beam is selected such that the linear stiffness coefficients are the same for all three structures. The simulated resonant frequencies are 2103.2, 2106.45 and 2106.89 Hz for four, eight, and sixteen beams, respectively.

ANSYS is used to simulate the amount of the rotation in angle as a result of the torque applied on the center disk. The torque-to-angle curves are plotted for three structures in Figure 3. 36. The curve for the sixteen beam structure shows higher nonlinearity, *i.e.*, small rotation at a given torque. They are re-plotted in Figure 3. 37 to find the numerical values of the torsional linear and nonlinear stiffness coefficients of k_l and k_{nl}. The simulation results and the parameters are summarized in Table 3. 7.

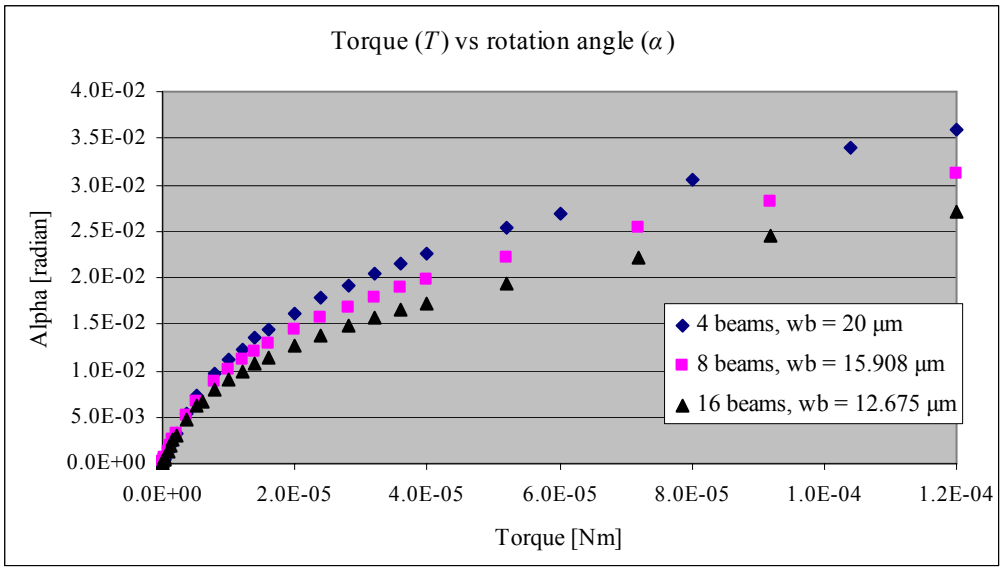

Figure 3. 36. A torque to rotational angle curves corresponding to the 20, 15.908, and 12.675 µm in beam width for the four, eight, and sixteen beam structures, respectively.

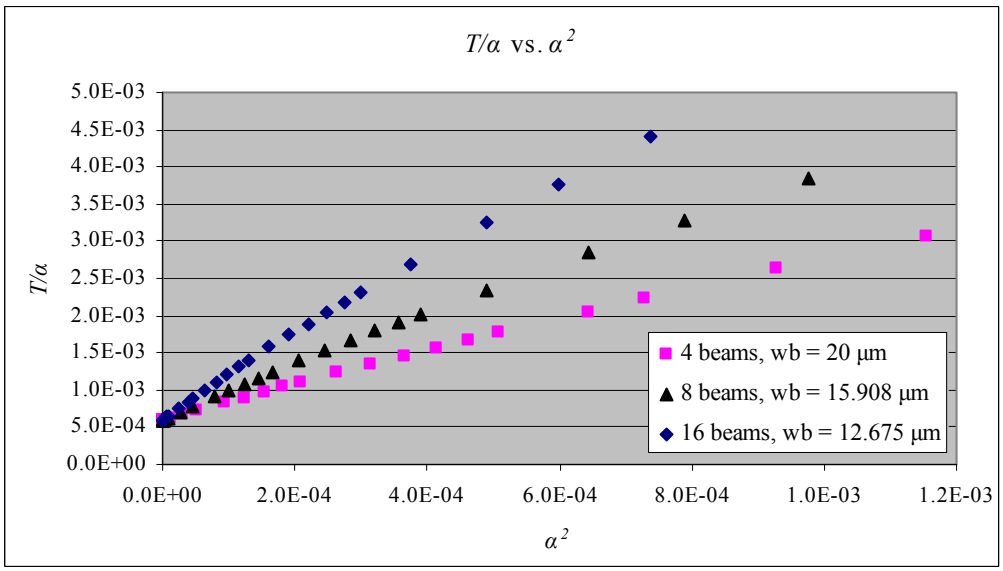

Figure 3. 37. T/α vs. α^2 curves for the three different beam widths. A k_l is the cross section of the straight line with y axis and k_{nl} is the slope of the straight line.

Table 3. 7. Characterization of the beam width and the number of beams using ANSYS.

Number of beams	Width of beam [μm]	k_l [10^{-6} Nm]	k_{nl} [10^{-2} Nm]	Resonant frequency *at* θ=0°. f_c [Hz]	Sensitivity $\Delta f_c/(f_c \cdot$ degree) [10^{-3} Hz/(Hz·degree)]		
					50 μT	0.975 mT	1.95 mT
4	20	581.0	192.0	2103.20	0.0018	0.320	1.130
8	15.908	586.0	333.2	2106.45	0.0024	0.5316	1.7466
16	12.675	594.0	517.6	2106.89	0.0031	0.7683	2.3612

As shown in Table 3. 7, the torsional linear stiffness coefficients, k_l, are set to be very close for the three designs by reducing the beam width for the designs with more beams. The four beam structure with 20 μm in the beam width shows lowest k_l while the sixteen beam structure with 12.675 μm in the beam width shows highest numerical value for the k_l. The resonant frequency of the four beam structure is lowest as is expected due to its lowest linear stiffness coefficient. The torsional nonlinear stiffness coefficient, k_{nl}, increases as more beams are used. The numerical value of α is inversely proportional to k_l (Equation 3. 15). Therefore, it decreases as more beams are used at a given torque in this simulation. Figure 3. 38 (a) shows that the four beam structure has the highest magnitude of α while the sixteen beam structure has lowest one at any θ. However, the sixteen beam structure shows the highest magnitude of the $k_{nl} \cdot \alpha^2$ while the four beam structure shows the lowest value at any θ since the magnitude of the k_{nl} is highest at the sixteen beam structure and eight, and four beam structure in that order (Figure 3. 38 (b)).

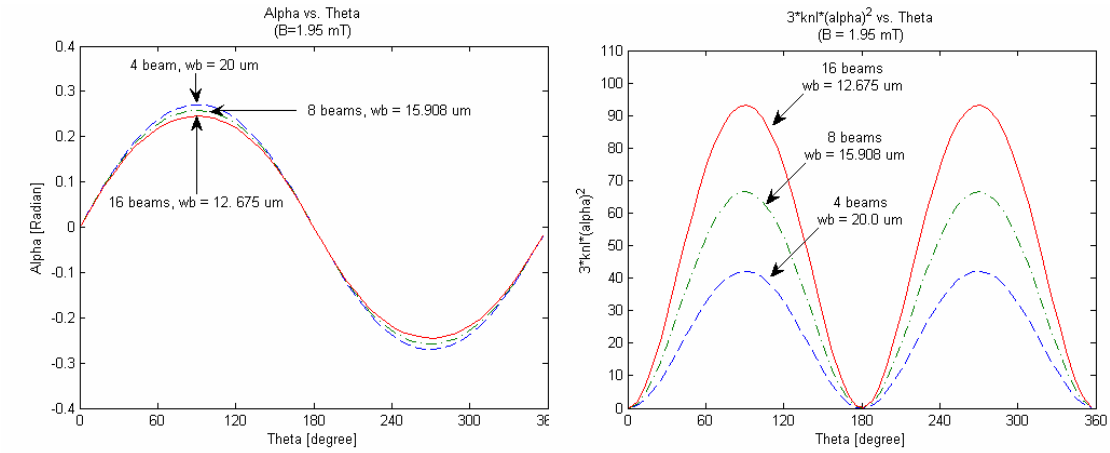

Figure 3. 38. The equilibrium angle and the torsional nonlinear stiffness coefficient comparison for the four, eight, and sixteen beam structures simulated at 1.95 mT. (a) Comparison of the equilibrium. (b) Comparison of the $k_{nl} \cdot \alpha^2$.

The resonant frequencies are evaluated at 50 μT, 0.975 mT, and 1.95 mT for three structures (Figure 3. 39 (a-c)). In this characterization, the same results are acquired using FEM simulation as is shown in the section 3. 2. 2. The normalized sensitivity increases by maximizing the nonlinearity at a given linear stiffness (Table 3. 7). Increasing the nonlinear stiffness coefficient at a given linear stiffness coefficient is achieved by using thinner beams as more beams are used. The sensitivity is maximized in this way while keeping the linear stiffness the same (Table 3. 7). A good agreement is made between characterization using theory and characterization using FEM simulation.

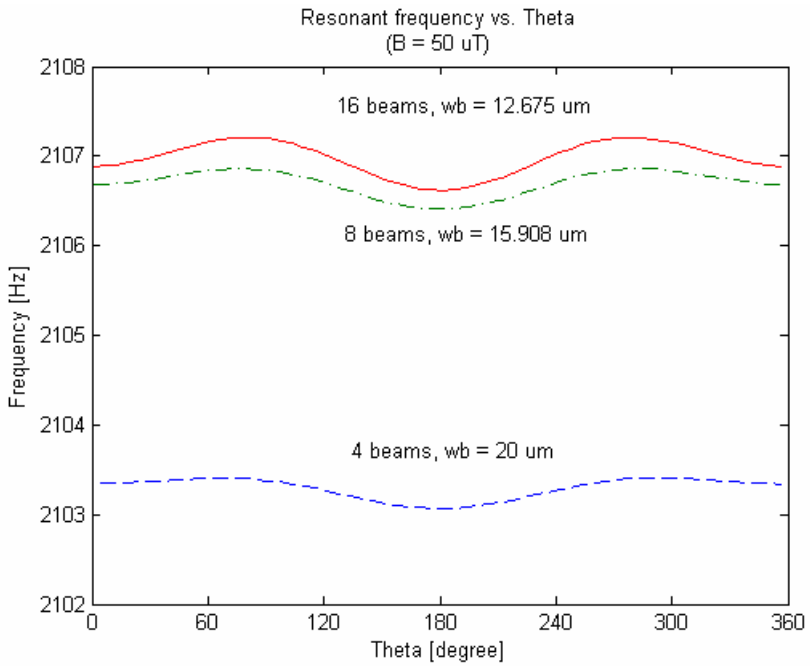
Resonant frequency vs. Theta
(B = 50 uT)
16 beams, wb = 12.675 um
8 beams, wb = 15.908 um
4 beams, wb = 20 um
Frequency [Hz]
Theta [degree]
2108
2107
2106
2105
2104
2103
2102
0
60
120
180
240
300
360

(a)

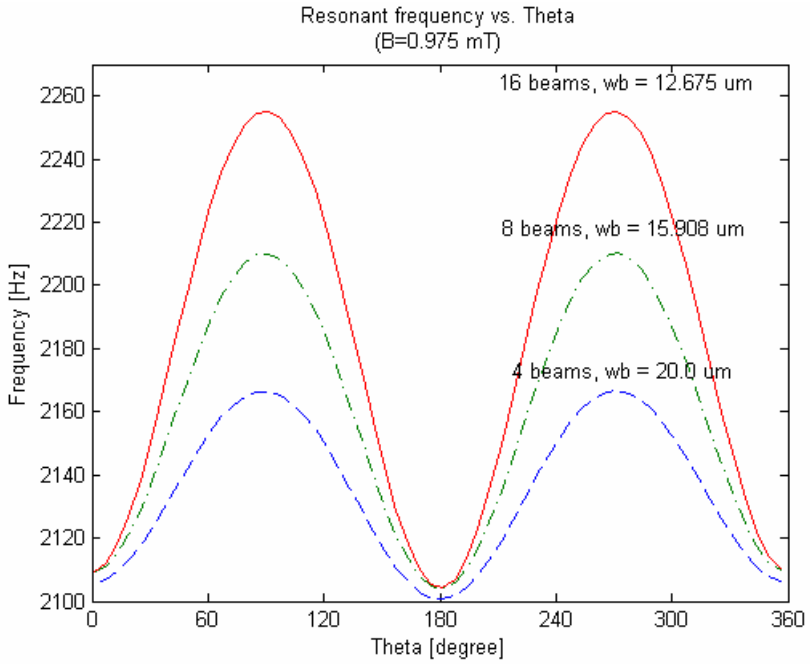
Resonant frequency vs. Theta
(B=0.975 mT)
16 beams, wb = 12.675 um
8 beams, wb = 15.908 um
4 beams, wb = 20.0 um
Frequency [Hz]
Theta [degree]
2260
2240
2220
2200
2180
2160
2140
2120
2100
0
60
120
180
240
300
360

(b)

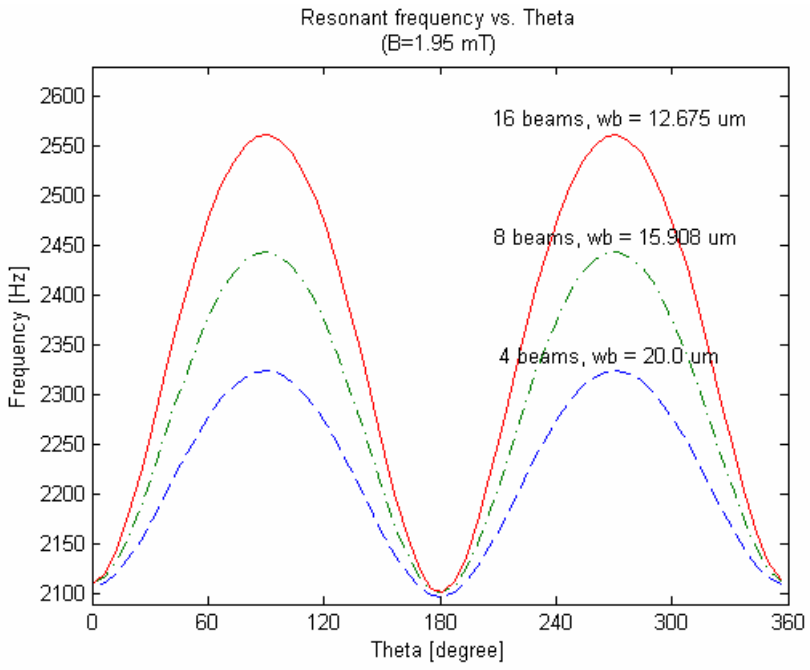

(c)

Figure 3. 39. Resonant frequency as a function of theta. (a) B = 50 μT, (b) B = 0.975 mT, and (c) B = 1.95 mT.

3.4 Comparison between theory and FEM simulation

Even though the characterization results from the theory and FEM simulations are well matched, there is a discrepancy in numerical values for linear and nonlinear stiffness coefficients. This mainly can be attributed from the fact that the nonlinear theory used in Section 3.2 does not consider a bending moment developed at the joint of beam and the center silicon disk. The bending moment can be taken into account by selecting proper boundary condition at the edges of beams. One example is to develop a torque at the center of beam and measure an angular rotation as shown in Figure 3. 40. However, this theory is valid when a rotation torque is replaced by force F1 and F2 while *d* approaches

zero at the center of the clamped-clamped beam (Figure3. 40) However, the torsional resonator that was fabricated and measured has slightly different geometry as shown in Figure 3. 41 in which torsional stiffness (k_θ) can be calculated more accurately by applying forces at the edge of the center disk since the center disk is a rigid body structure. This rigid body effect of center disk must be considered for calculation of torsional stiffness since portions of beams embedded in the center disk dose not undergo significant bending. The torsional resonator shown in Figure 3. 41 is simulated in two different ways by changing numerical value of *d*.

A linear stiffness coefficient of Figure 3. 40 is found to be [55],

$$k_\theta = \frac{T}{\theta} = \frac{2dF}{\theta\big|_{x=L/2}} = \frac{2dEI}{\left(\frac{(\frac{L}{2}+d)\cdot(\frac{L}{2}-d)\cdot d}{L} - \frac{(\frac{L}{2}+d)^2\cdot(L-d)-(\frac{L}{2}-d)^2\cdot(L+d)}{4L} + \frac{1}{2}d^2 \right)} \tag{3. 31}$$

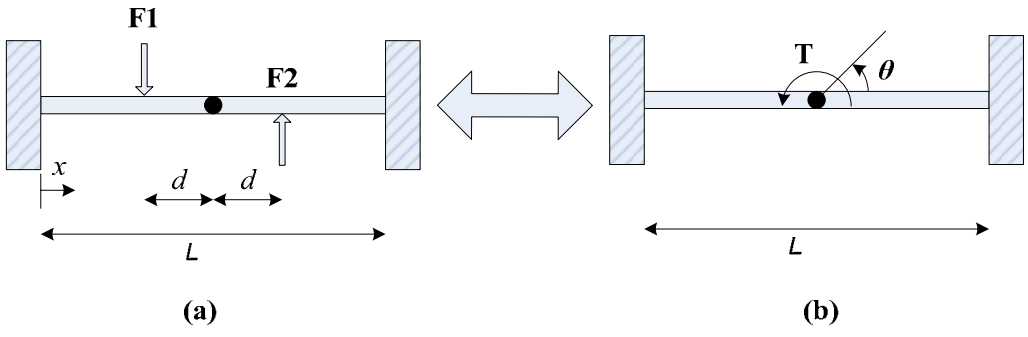

Figure 3. 40. Clamped-clamped beam structure with applied torque in the center [55]. (a) Torque is applied by F1 and F2, (b) Resultant torque and angular displacement.

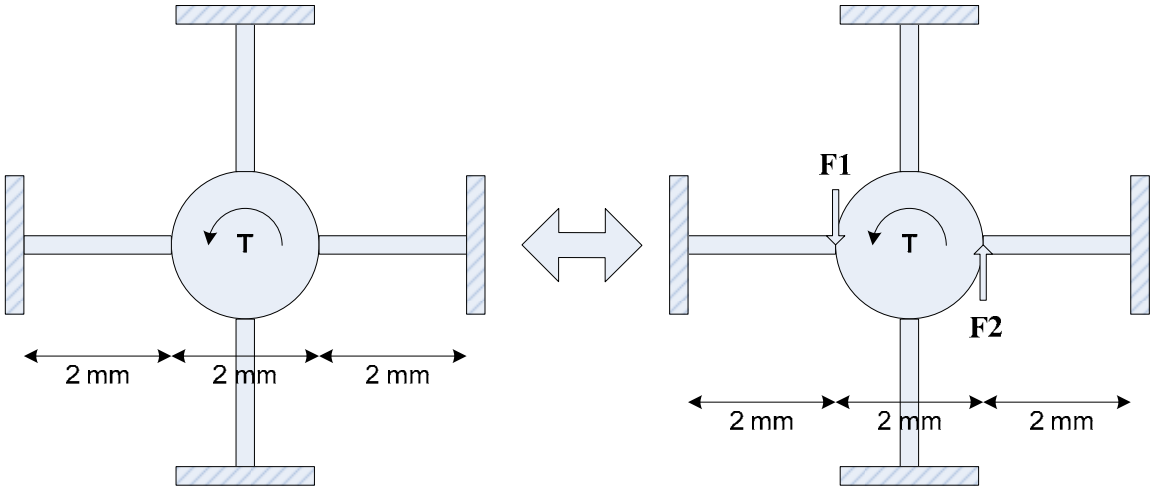

Figure 3. 41. Torsional resonator that has to be modeled.

The amount of bending moment that is generated from the forces depends on the distance of *d* (Figure 3. 40). The linear stiffness coefficients from Equation (3. 31) for *d*=0 (CASE B) and *d*=1 (CASE C) are simulated and compared with FEM simulation results in Table 3. 8. Moment developed at the joint of beam and disk is considered in CASE B and C while it is not considered in CASE A (theory used in Section 3. 2). The simulation results clearly show that a torsional stiffness calculated from the model in which moment at the end of beams are considered is more close to what was evaluated using ANSYS simulation (CASE D). Furthermore, the simulation results are improved when we consider rigid body effect of the center disk by applying force with finite value of *d* (1 mm) (CASE C) rather than with banishing value of *d* (CASE B). This implies that if moment and rigid body effect of center disk are modeled more accurately, then the

torsional stiffness calculated from theory will be well matched with FEM simulation results. Structural parameters used for simulation are listed in Table 3. 9.

Table 3. 8. Comparison of numerical values of k_l from nonlinear theory and clamped-clamped beam theory. Note that k_θ is corresponding k_l in this table.

CASE	A	B	C	D
Beam width	Theory in Section 3.2 [10^{-6}]	Equation 3. 31 [10^{-6}]	Equation 3. 31 [10^{-6}]	FEM results in Table 3.6 [10^{-6}]
10 μm	16.56	22	33	73.3
20 μm	132.13	176	264	581
30 μm	445.48	594	891	1936.7
		d = 0	d = 1 mm	

Table 3. 9. Structural parameters used to simulation.

w_b (beam width)	10 ~ 30 μm	d	1 mm
t (beam thickness)	200 μm	E (Young's modulus)	165 G
L (total beam length)	6 mm		

3.5 Optimum design for the maximum sensitivity

In this section, an optimum design is suggested based on the characterization of the previous sections and the fabrication constraints. The characterization on the beam width recommends having thinner beam width at a given number of beams. The characterization on the beam width and the number of beams recommends having more beams with thinner beam width at a given linear stiffness *i.e.*, given operating resonant

frequency. The constraints imposed by fabrications need to be considered also at the design stage. Aspect ratio of the silicon etching is one of the big constraints imposed by the Inductively Coupled Plasma (ICP) machine. The Bosch process enables a high aspect ratio structure up to 1:15 by alternating deposition and etching steps. However, aspect ration of 1:10 is recommended in this optimization to achieve uniform and good vertical profiles of the beam structure. A standard 2 inch silicon wafer has around 300 μm in thickness and can be easily thin down to the 100 μm using either silicon back side etching technique or polisher. Aspect ratio limitation of the etching process gives 10 μm in beam width for the 100 μm thick silicon wafer. It is stated that the linear stiffness should be minimized to increase the sensitivity of the resonator, thereby lowering the resonant frequency. If the resonant frequency is too low, the performance of the overall measurement system is reduced due to the low frequency noise from the circuitry components and the noise from the sensing coil component. Many mechanical and electrical noises surrounding the sensor are limited in the low frequency region. The sensing coil detects not only the resonance of the permanent magnet, but also the time varying magnetic field around it. For example, the 60 Hz ac electrical signal generates a time varying magnetic field and the sensing coil generates and passes an undesirable harmonics from it into the circuitry whose main function is amplifying and phase shifting. Therefore, the resonator is designed to operate higher than certain frequency. If the operating frequency is too high, then the sensitivity is not high enough to measure the low magnetic field such as the Earth's magnetic field. In this optimization, the operating frequency is selected to be around 1 kHz. The number of beams is determined from the parameters such as the beam width of 10 μm, the operating frequency of around 1 kHz,

the beam length of the 2 mm, and the thickness of the 100 μm. The number of beams is twelve and the resonant frequency is 972.1 Hz. The design sequences are described in Figure 3. 42. The parameters are summarized in Table 3. 10.

Table. 3. 10. Structure dimensions for optimum design.

Number of beams	12
Length of beams [mm]	2
Width of beams [μm]	10
Thickness of beams [μm]	100
Radius of center disk [mm]	1
Resonant frequency [Hz]	972.1

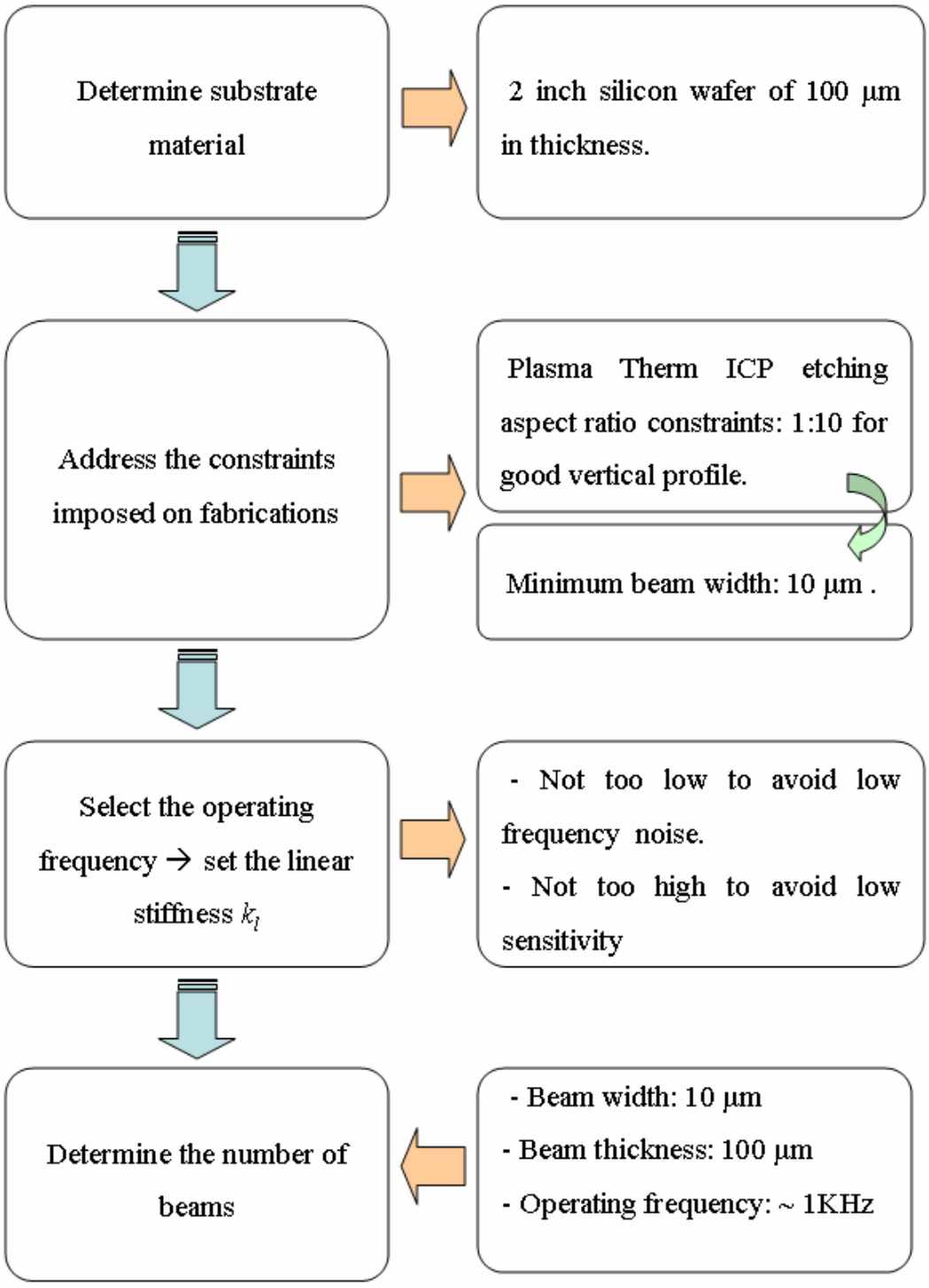

Figure 3. 42. Flowchart for optimum design.

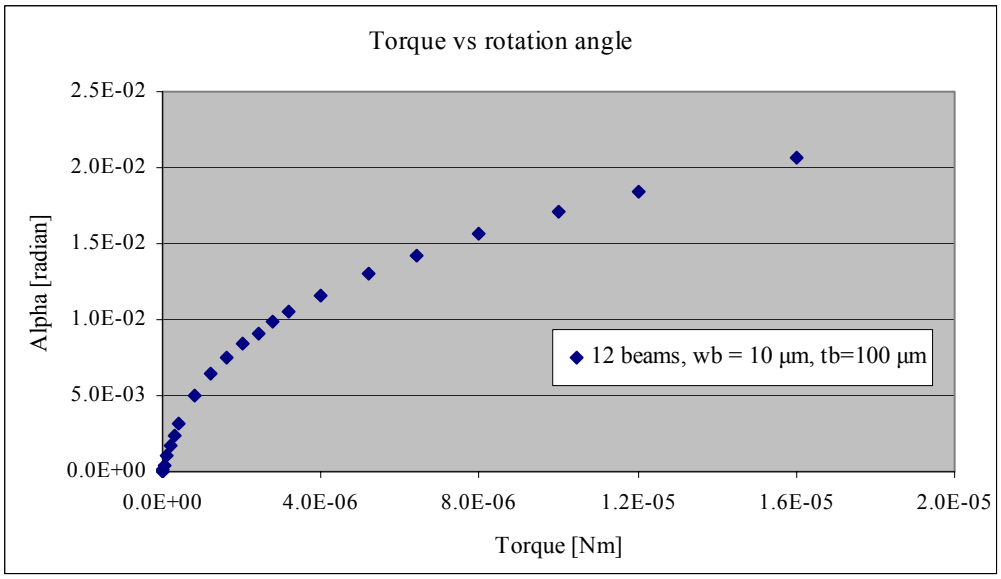

Figure 3. 43. A torque to rotational angle curve simulated using optimum design parameters.

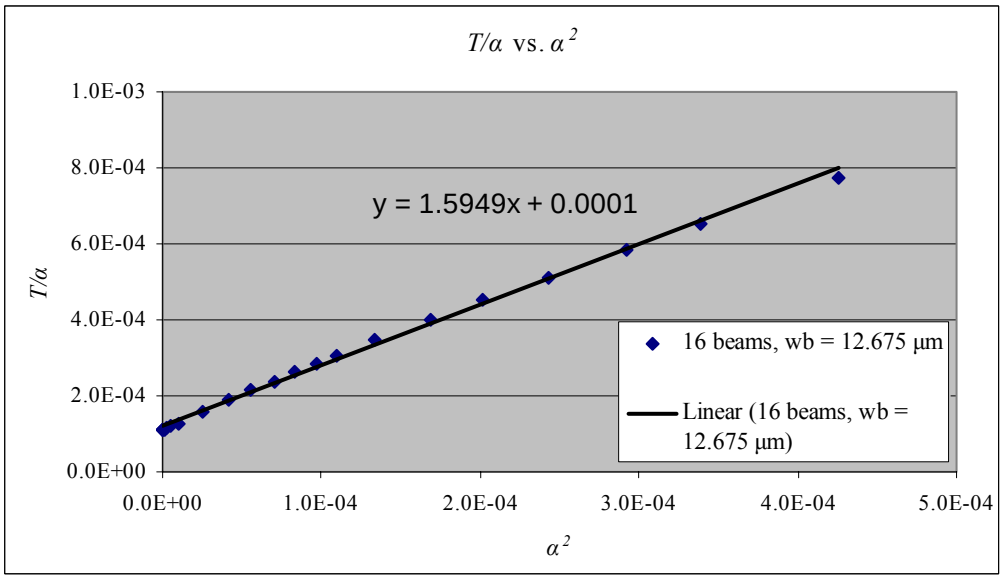

Figure 3. 44. *T/α vs.* α^2 curve. Note that a linear trendline is superimposed on the simulated data showing the k_l and k_{nl}.

ANSYS is used to simulate the amount of the rotation in angle as a result of the torque applied on the center disk. The torque-to-angle curves are plotted in Figure 3. 43. The numerical values of the torsional linear and nonlinear stiffness coefficients of k_l and k_{nl} is calculated in Figure 3. 44. A linear trendline is added on the simulation result to confirm the linear relations between T/α *vs*. α^2.

The optimized design simulated at the applied torque which is equivalent to the external magnetic fields of 50 μT, 0.975 mT, and 1.95 mT. The magnitudes of the $3k_{nl}\,\alpha^2$ are greater than those of the $T_0 \cdot cos(\theta-\alpha)$ for the all three external magnetic fields (Figure 3. 45 (a – c)). Therefore the shapes of the resonant frequency curves follow the shape of the *sine squared* function (Figure 3. 46 (a, b)).

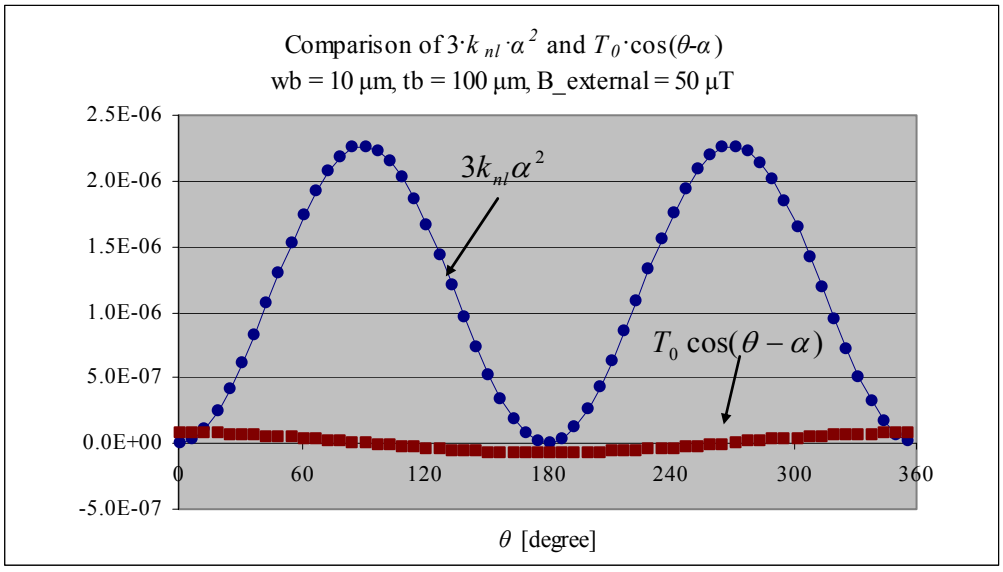

(a)

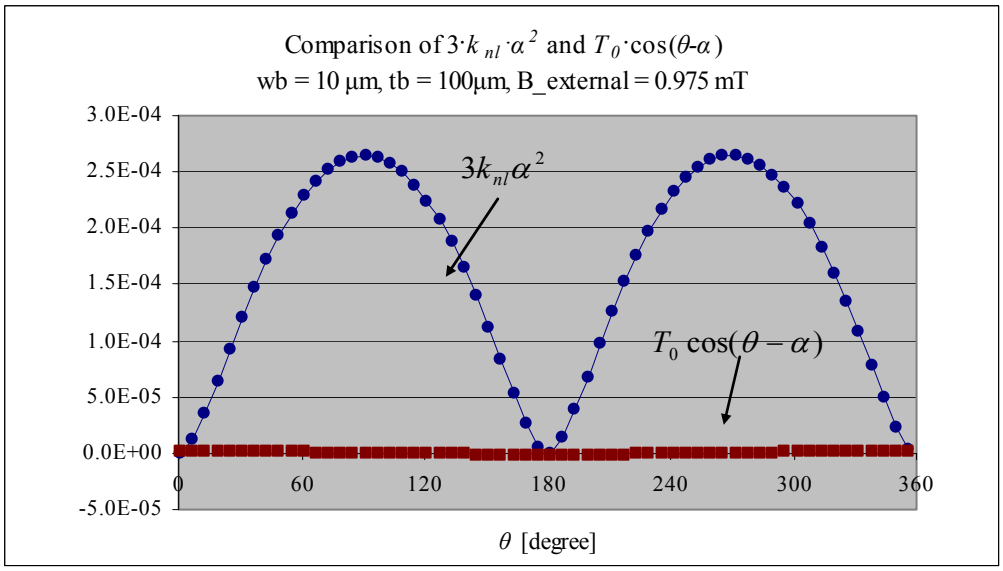

(b)

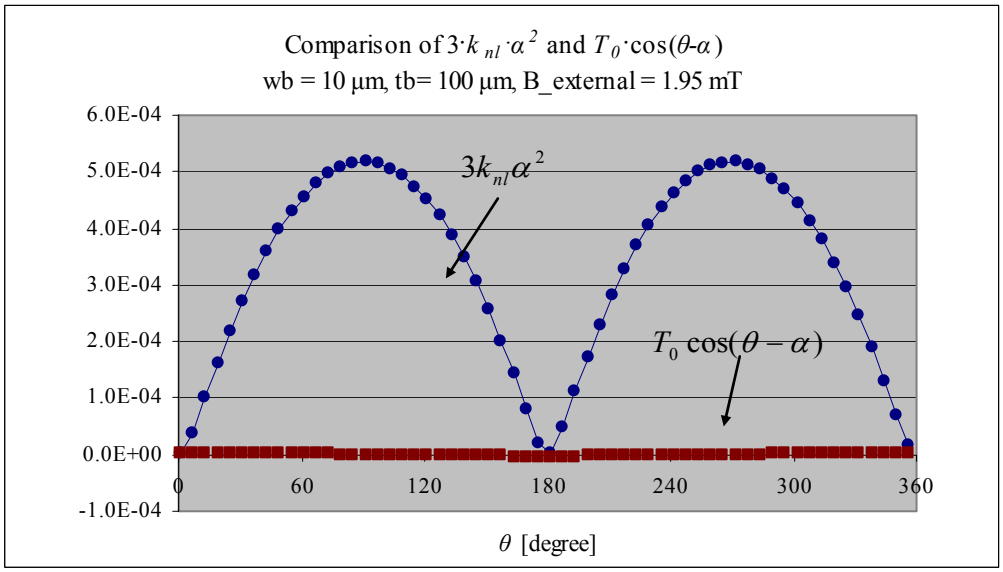

(c)

Figure 3. 45. A comparison of the $3k_{nl}\,\alpha^2$ and $T_0 \cdot cos(\theta - \alpha)$ in profile. (a) B = 50 μT, (b) B = 0.975 mT, and (c) B = 1.95 mT.

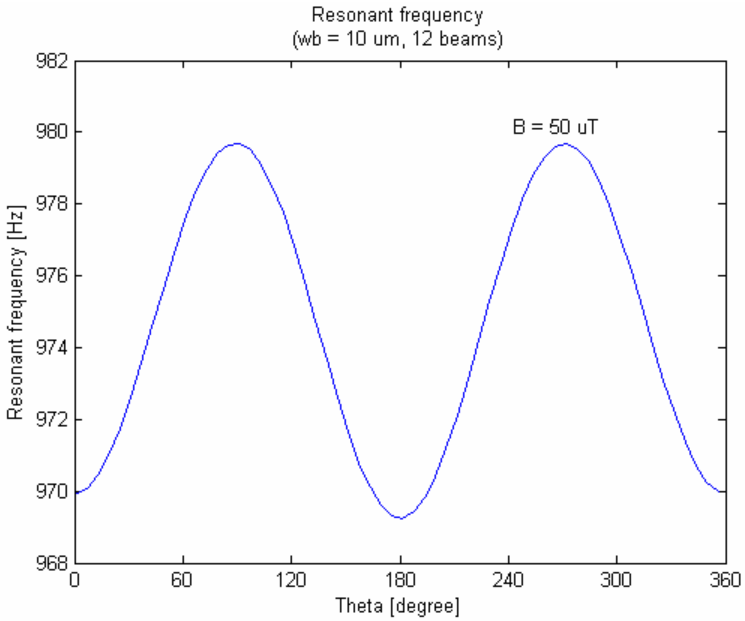

(a)

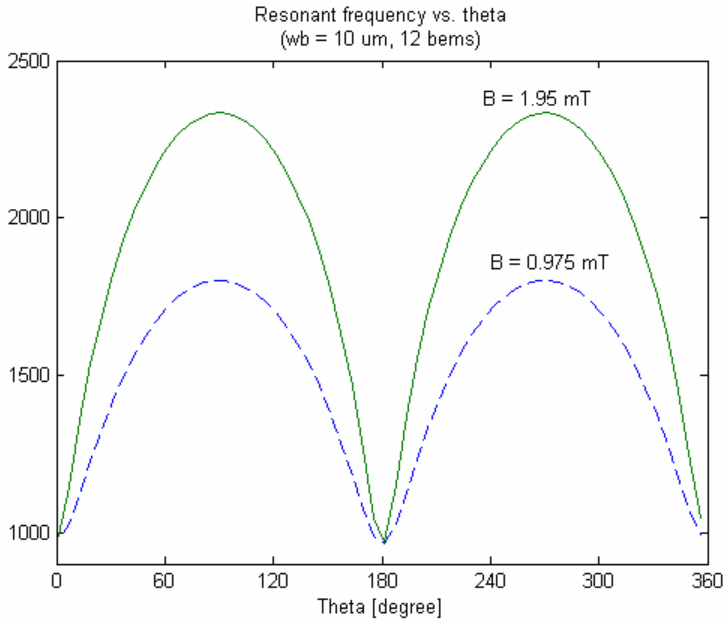

(b)

Figure 3. 46. Resonant frequency evaluated at (a) B = 50 μT, (b) B = 0.975 mT, and (c) B = 1.95 mT.

Table 3. 11. Simulation results for the optimized design.

Number of beams	Width of beam [μm]	k_l [10^{-6} Nm]	k_{nl} [10^{-2} Nm]	Resonant frequency *at* $\theta=0°$. f_c [Hz]	Sensitivity $\Delta f_c/(f_c \cdot$ degree) [10^{-3} Hz/(Hz·degree)]		
					50 μT	0.975 mT	1.95 mT
12	10	108	156.6	972.1	0.1197	9.3618	15.1540

The simulation results are summarized in Table 3. 11. The resonant frequency is 972. 1 Hz. The normalized sensitivities are 0.1197, 9.3618, and 15.1540 Hz/(Hz·degree) for 50 μmT, 0.975 mT, and 1.95 mT, respectively. The beam deflection shape at the 1.95 mT is shown in Figure 3. 47.

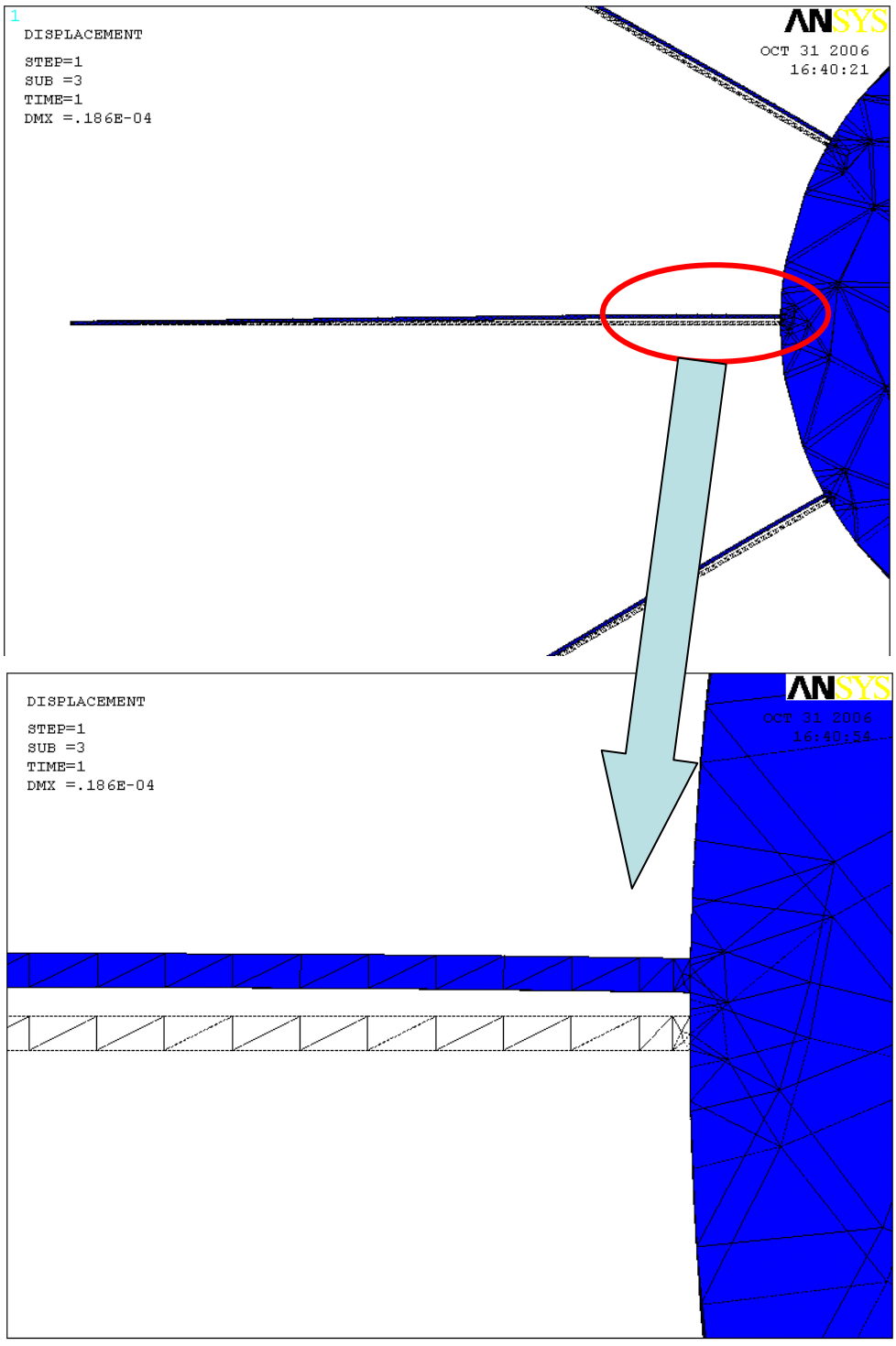

Figure 3. 47. The large deflected beam shapes simulated by ANSYS.

3.6 Conclusions

In this chapter a theoretical modeling for the mechanical resonator is developed. A nonlinear modeling is used to address the important nonlinear behavior of the resonator. The sensitivity of the resonator is simulated with several different beam widths at a given number of beams and characterized. The sensitivity of the resonator is simulated with several combinations of the beam widths and the numbers of beams at a given linear stiffness coefficient and characterized. Two methods of the characterization are used: 1) a numerical method, 2) a Finite Element Method. A numerical method is solving the nonlinear equation numerically while the FEM is simulating the nonlinear behavior of the resonator using ANSYS. Both methods produce the same characterization results. The sensitivity of the resonator increases as the beam width decreases at a given number of beams. The sensitivity of the resonator increases as the number of beams increase at a given linear stiffness which accompanies thinner beam width.

An optimum design is presented considering constraints on the fabrication and measurement efficiency. The aspect ratio of the beams is limited to 1:10 due to the capability of the silicon etching process. The beam width is minimized to maximize the sensitivity of the resonator. The resonant frequency of the resonator is set to be 972.1 Hz to avoid the problems such as low frequency noise of the measurement circuitry and the environmental harmonics picked up by the sensing coil. Base on those constraints, the number of beams are set to be twelve. The resonator is simulated at the external magnetic fields of 50 μT, 0.975 mT, and 1.95 mT using ANSYS.

CHAPTER 4

LOW POWER / LOW VOLTAGE RESONENT MAGNETIC FIELD SENSOR

A magnetic field sensor incorporating a micromachined silicon mechanical resonator and a permanent magnet is fabricated. The device is tested and characterized to determine the direction of the various external magnetic fields including Earth's magnetic field. Two different excitation and detection schemes are used to achieve low power consumption and a low voltage operation: 1) electrostatic excitation and magnetic detection, 2) electromagnetic excitation and electromagnetic detection (Table 4. 1). A complete magnetic sensing system is presented by implementing electronic circuitry performing positive feedback to make a self oscillating resonator.

Table 4. 1 Different excitation and detection schemes.

	Excitation method	Excitation component	Detection method	Detection component
Scheme 1	Electrostatic	Comb-drive	Magnetic	Hall-Effect sensor
Scheme 2	Electromagnetic	Coil	Electromagnetic	Coil

4.1 Electrostatically excited and magnetically sensed comb drive magnetic sensor

Electrostatic excitation and capacitive detection techniques are widely used for silicon resonators and inertial sensors because they consume very little power and can be implemented with other electronic components on the same silicon substrate. However, the crosstalk between excitation and detection is a considerable limitation for a capacitive detection. This crosstalk makes it difficult to isolate the sensed signal from the excitation signal. Several researchers have addressed this problem and suggested many different ways to avoid the unwanted communication between excitation and sensing ports often adding up the complexity of the electronic circuitry [56-59]. Also complex circuitry to read out extremely small capacitance variation may be required. In this section, a new method is presented to avoid the crosstalk between excitation and sensing ports by using a Hall-Effect sensor to detect the motion of the permanent magnet. Utilizing a Hall-Effect sensor as the detection component not only enables the detection scheme to be much simpler but also provides very effective isolation between sensing and detection ports.

4.1.1 Electrostatic actuation

Two configurations of electrostatic excitation are possible by implementing either a lateral comb drive structure or vertical comb drive structure. There are several drawbacks to the vertical driving of the micro-mechanical resonator [60]. The first one is that the electrostatic force with voltage control is nonlinear unless the amplitude of the vibration is limited to a small fraction of the capacitor gap (Figure 4. 1).

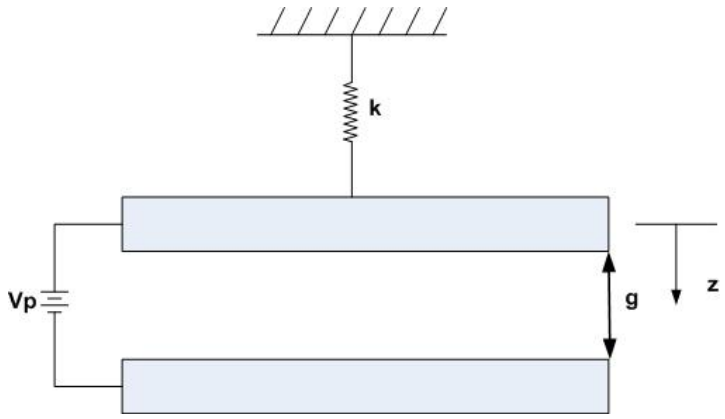

Figure 4. 1. Typical configuration for the vertical electrostatic excitation.

For an idealized parallel plate capacitor in Figure 4.1, the capacitance is given by,

$$C = \frac{\varepsilon A}{z} \tag{4. 1}$$

where ε is the permittivity, and A is the parallel plate area. The electrostatic force in the z direction is given by,

$$F_Z = \frac{\partial E}{\partial z} = \frac{1}{2} V_P{}^2 \frac{\partial C}{\partial z} = \frac{\varepsilon A V_P{}^2}{2g^2} \tag{4. 2}$$

where E is the stored energy in the capacitor, C is the capacitance, and V_P is the applied voltage. This equation clearly shows that the electrostatic force is a nonlinear function of the capacitor gap. To maintain linearity the vibration amplitude should be small compared to the capacitor gap. There also exists a pull-in voltage which is the maximum voltage that can be applied to the parallel plate without losing stability of the equilibrium

that exists between the electrostatic force pulling the plate down and the spring force pulling the plate up [61]. It is readily shown that the pull-in occurs at,

$$g_{PI} = \frac{2}{3} g_0 \tag{4. 3}$$

where g_0 is the gap at zero volts and zero spring extension [61]. And at this value of the gap, the pull-in voltage is given by,

$$V_{PI} = \sqrt{\frac{8k \cdot g_0^3}{27\varepsilon A}} \tag{4. 4}$$

where k is the spring constant, A is the area of the parallel plate, and ε is the permittivity of free space.

Secondly, the quality factor Q of the resonator is very low at atmospheric pressure because of squeeze film damping in the micron-sized capacitor gap [62, 63].

More than 10 years ago, Tang and Howe introduced a laterally driven comb drive actuator [64]. Since then extensive research has been carried out either to design an optimum lateral comb drive structure or to implement the electrostatic actuator using this structure since it offers a nearly constant force over a large range of displacements (Equation 4. 7) [65-67]. A key feature of the laterally driven comb drive is that $\partial C/\partial x$ is a constant (Equation 4. 6), independent of the displacement x, as long as x is less than the overlap between the comb fingers, l (Figure 4. 2). Lateral comb drives provide linear electromechanical transfer functions for large displacements, in contrast to the parallel plate vertical drives [64]. They are driven by superimposing a direct current (DC)-bias voltage V_p to the resonator and an AC excitation voltage which is applied to the one of the drive electrodes. The polarization voltage (V_p) has two purposes: the first one is to avoid having the microstructure moving at twice the frequency of the applied drive

voltage and the second one is to amplify the output current resulting from the microstructure motion (Equation 4. 8) [43].

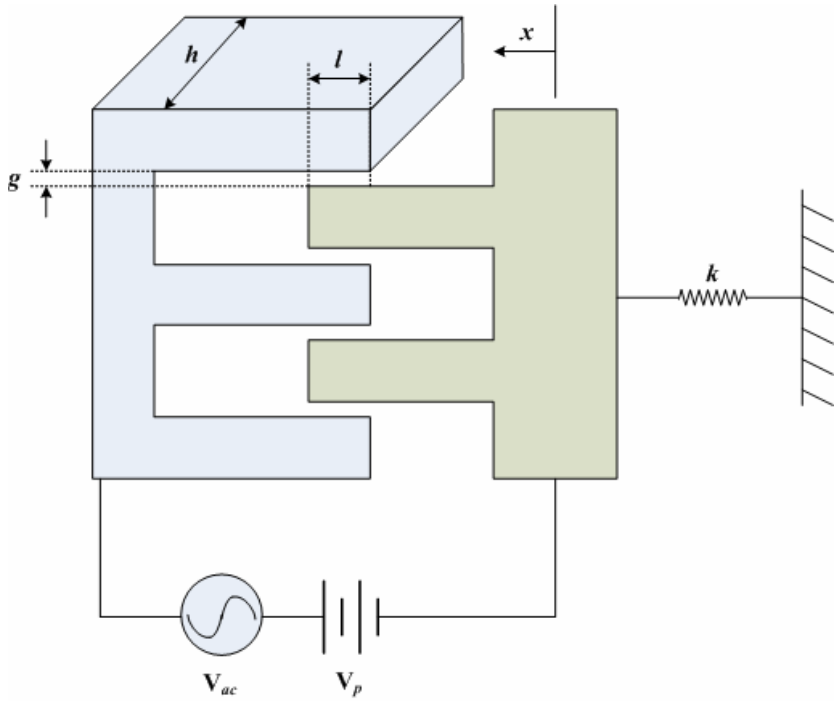

Figure 4. 2. Typical lateral comb drive configuration. Note that only excitation part is shown [57].

A capacitance of the typical lateral comb drive structure can be modeled as,

$$C(x) = \frac{\alpha \cdot N \cdot \varepsilon \cdot Area}{g} = \frac{\alpha \cdot N \cdot \varepsilon \cdot (l + x)h}{g} \tag{4. 5}$$

where N is the number of finger gaps, h is the film thickness, x is the displacement of the beam, and g is the gap between the electrode and the resonator fingers [44]. The constant

α models additional capacitance resulting from fringing electric fields. It is 1.2 for comb geometries [45]. For the interdigitated-comb drive resonator, the capacitance varies linearly with displacement. Thus, the change in capacitance per unit displacement, $\partial C / \partial x$, is a constant, given approximately by,

$$\frac{\partial C}{\partial x} = \frac{\alpha \cdot N \cdot \varepsilon \cdot h}{g} \tag{4. 6}$$

The force can be calculated from the Equation (4. 6) as,

$$F_x = \frac{\partial U}{\partial x} = \frac{1}{2} V^2 \frac{\partial C}{\partial x} \tag{4. 7}$$

where U is energy associated with applied voltage between comb drive gaps. To excite the resonator, a small AC signal is superimposed on the DC signal as shown in Figure 4. 2. The equation (4. 7), thus can be given as,

$$F_x = \frac{1}{2}(V_P + V_{ac})^2 \frac{\alpha \cdot N \cdot \varepsilon \cdot h}{g} = \frac{1}{2}(V_p^2 + 2V_p \cdot V_{ac} + V_{ac}^2)\frac{\alpha \cdot N \cdot \varepsilon \cdot h}{g} \tag{4. 8}$$

The second term of the Equation (4. 8) is only interested since it comes out of the applied excitation signal. The third term is negligible assuming small AC signal and first term contains only the DC component.

4.1.2 Design and Fabrication

A micromachined magnetic sensor consists of a mechanical resonator and a permanent magnet. The silicon disk needs to have a rectangular shaped trench to hold the permanent magnet securely (Figure 4. 3). The beams are designed to be strong enough to hold the permanent magnet and also to enable the lateral torsional vibration mode as the primary resonant one (Figure 4. 4). The designed structure is simulated using the ANSYS

finite element software to confirm the first resonant mode shape. Table 4. 2 summarizes the structural dimensions. More details about the permanent magnet are found in Table 4. 3.

Table 4. 2. Structural dimension for the silicon resonator.

Number of beam	3	Comb finger width	20 μm
Width of beam	20 μm	Comb finger gap	20 μm
Length of beam	2 mm	Magnet thickness	800 μm
thickness	200 μm	Magnet diameter	1.6 mm

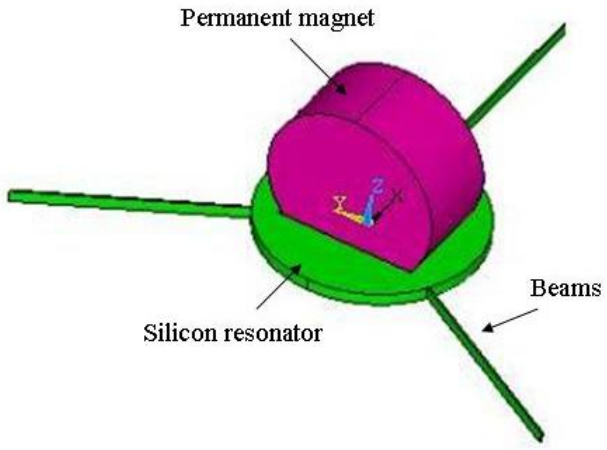

Figure 4. 3. Design of the silicon resonator which has the 3 beams to support the permanent magnet.

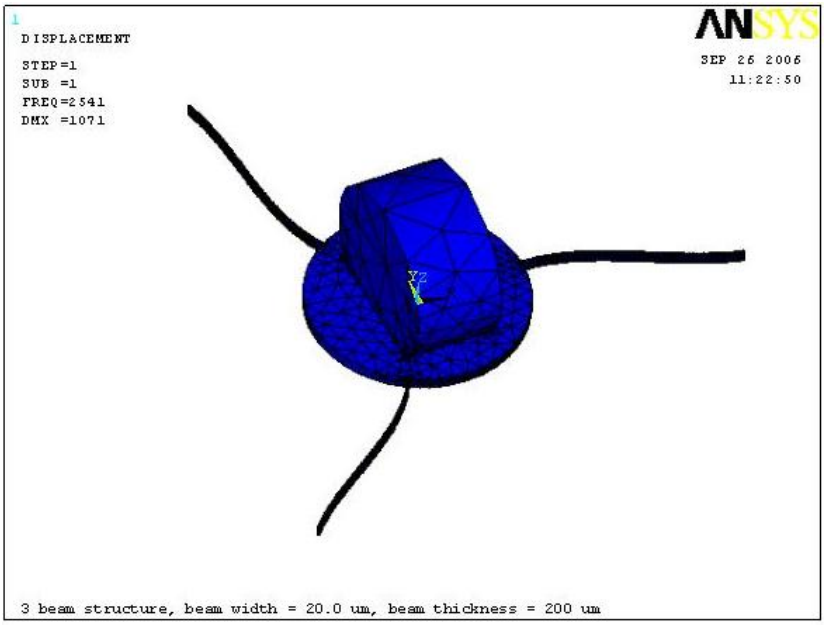

Figure 4. 4. A FEM simulation using ANSYS. The first resonant mode is a lateral torsional shape with the resonant frequency of 2541 Hz.

The fabrication of the comb drive magnetic sensor is based on bulk silicon micromachining. An intermediate silicon dioxide layer is used for electrical isolation of the driving ports and the sensing ports. The oxide layer of 0.7μm is thermally grown in the Lindberg furnace (Figure 4. 5 (A)).

Two wafers are bonded together using a silicon wafer fusion bonding technique (Figure 4. 5 (B)) [68, 69]. Wafer bonding is a key technology to create inexpensive thick film silicon-on-insulator (SOI) materials of high quality. The surfaces to be bonded have to be flat having an average roughness typically in the order of less than about 10 Å [70]. The surface preparation step involves cleaning the mirror-smooth, flat surfaces of the two wafers to from the hydrated surfaces. A particle on the surface results in a void between the bonding surfaces. Effects of hydrophobic and hydrophilic surfaces on the bonding

quality have been researched [71]. Following this preparation, the wafers are brought into the contact in a cleanroom by gently pressing the two surfaces together at one central point. The initial weak contact is created at this time by a surface attraction of the two hydrated surfaces. The bonding is strengthened by high temperature annealing typically at 1100°C for a couple of hours. Infrared imaging system is used to inspect the interface bonding states, i.e., the size and the density of the bonding defects such as voids (Figure 4. 6).

The adhesion of silicon beams to the substrate, known as "stiction", has been found and studied in 2D silicon surface micromachining [72, 73]. It has been referred as a major factor that influences the reliability of silicon surface micromachined devices [74]. Stiction problem can be traced to a very thin oxide layer that is often used as a sacrificial layer to form moving 3D structures. Strong capillary forces are developed in the fabrication process during the wet etch of the sacrificial layers, in this case SiO_2. The magnitude of these forces is in some cases sufficient to deform and collapse these structures to the substrate resulting in device failure [72]. The oxide underneath the movable structure is completely removed not only to avoid a stiction but also to prevent the electrostatic levitation (Figure 4. 5 (C), Figure 4. 7) [75].

The upper silicon wafer is etched by Inductively Coupled Plasma (ICP) to realize the movable resonant disc structure (containing a recess for the permanent magnet), support beams, and contact electrodes (Figure 4. 5 (D)). Both the bottom and the top side of the silicon wafer is etched using deep Reactive Ionic Etching (RIE) technology. A metal shadow mask created using the IR laser is used to generate the contact electrode using the E-beam evaporation (Figure 4. 5 (E), Figure 4. 8).

The permanent magnet is glued on the center of the moving structure using epoxy glue (Figure 4. 5 (F)). A commercially available permanent magnet is used. Properties of the permanent magnet are summarized in Table 4. 3. Contact electrodes on the silicon devices and pads on the handling glass substrate are connected using wire bonding (Figure 4. 5 (g)). Fabrication has the following characteristics: CMOS-compatible, low-cost, low-temperature and simple two-mask fabrication (Figure 4. 5).

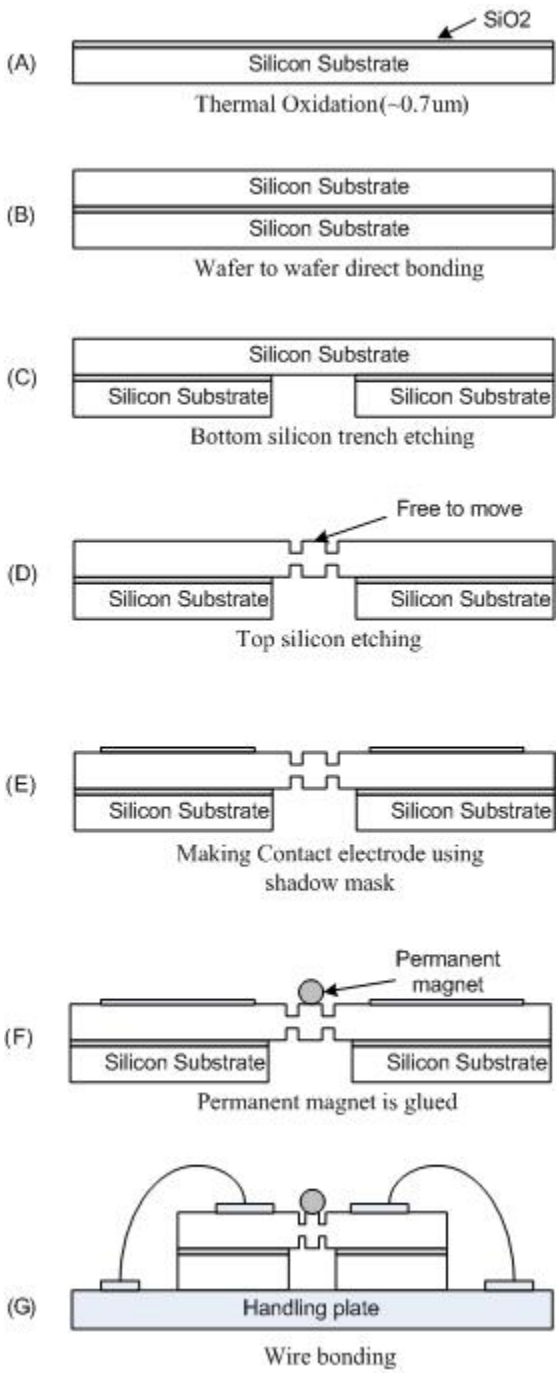

Figure 4. 5. Fabrication sequence to build the comb drive electrostatic resonator.

Table 4. 3. The properties of the permanent magnet [76].

Material	NdFeB (Grade N48)	Pull force	0.20 lb
Diameter	1.6 mm	Surface field	0.18 Tesla
Thickness	0.8 mm	$B_{r,max}$	1.42 Tesla
Coating material	Ni	$B_{H,max}$	3.82 G A/m
Magnetization direction	Axial (Poles on flat ends)	Weight	11.8 mg

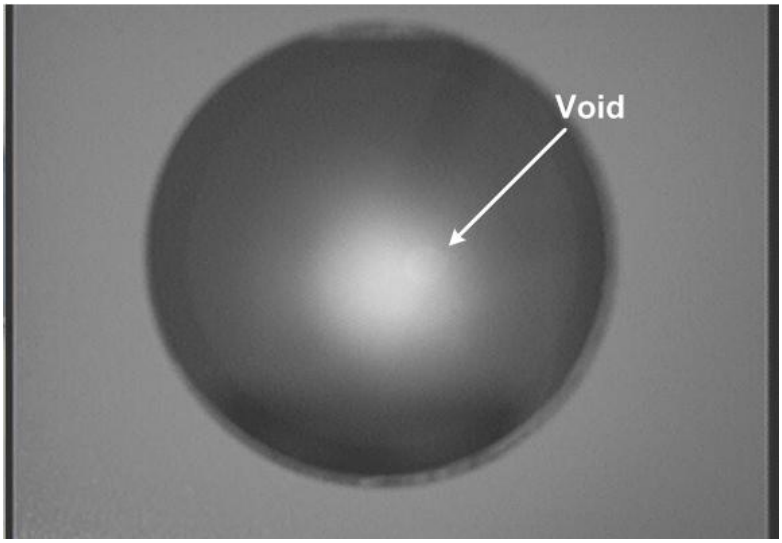

Figure 4. 6 Infrared image to inspect the wafer bonding quality.

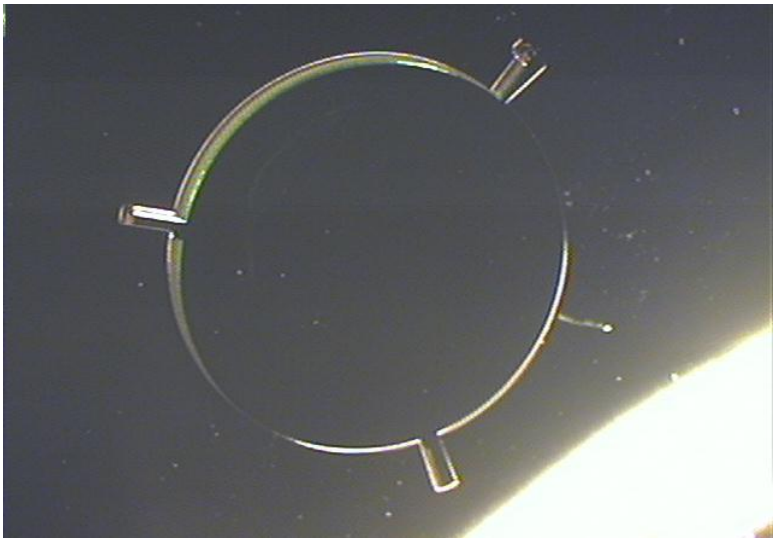

Figure 4. 7 Bottom trench is formed to prevent a “stiction” during the release.

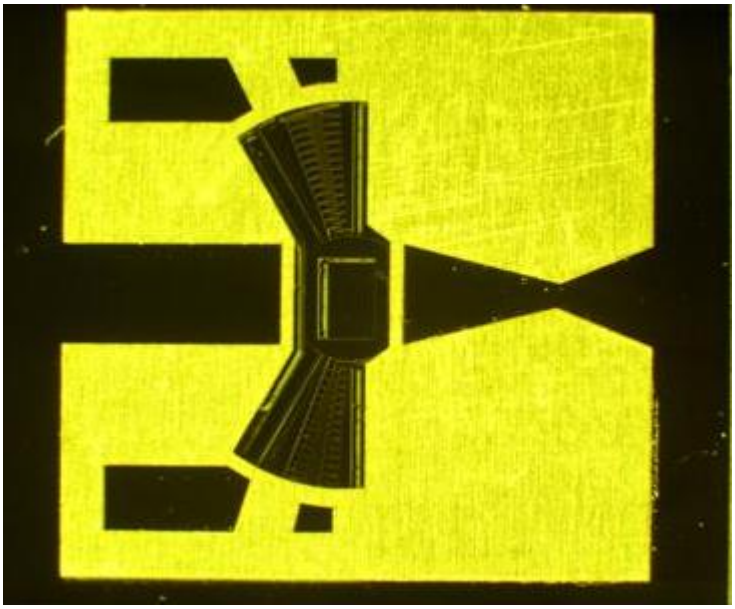

Figure 4. 8 Alignment of the metal shadow mask with the fabricated comb-drive silicon device. The metal shadow mask is manufactured using IR laser machining.

Scanning Electron Microscope (SEM) images of the fabricated silicon resonator are shown in Figures 4. 9 - 10. The comb finger structure has about 1:10 aspect ratio defined as the ratio of width to thickness. The gaps between comb fingers are carefully examined to make sure all the fingers are not connected to each other. A relatively high DC polarization voltage is applied between fingers therefore a high current might flow through if the fingers were to short-circuit. Figure 4. 11 shows the image of the complete device. The permanent magnet is well sitting in the center of the resonator disk. The measurement setup is discussed in the next section showing the electrical connection and the Hall-Effect sensor assembly.

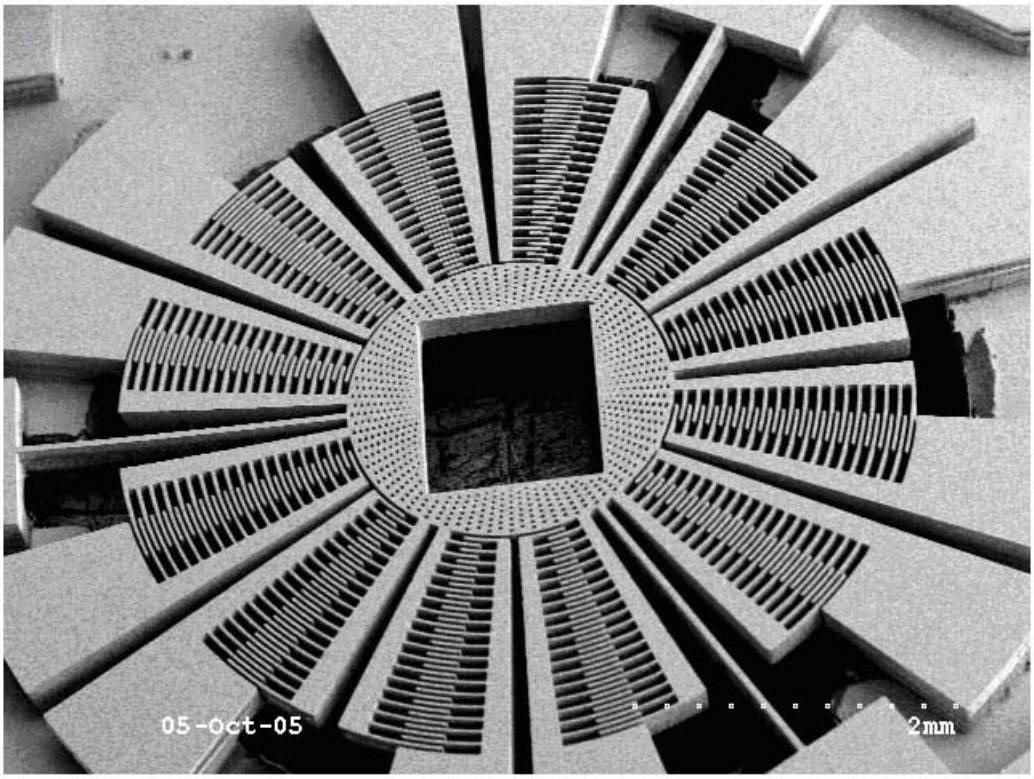

Figure 4. 9 A SEM image of the fabricated silicon resonator structure. There is a rectangular shaped trench in the center to hold a permanent magnet.

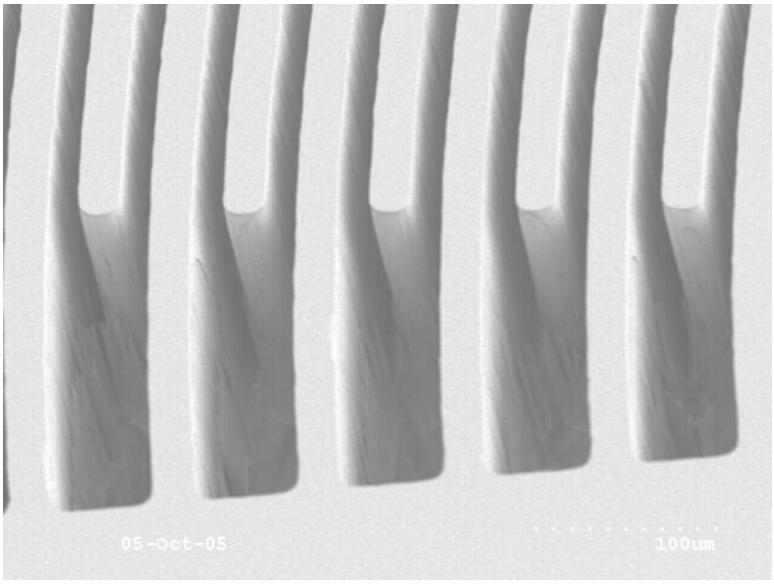

Figure 4. 10. A SEM image of the comb-drive structure. The width of the comb finger is 20 μm and the gap between fingers is 20 μm.

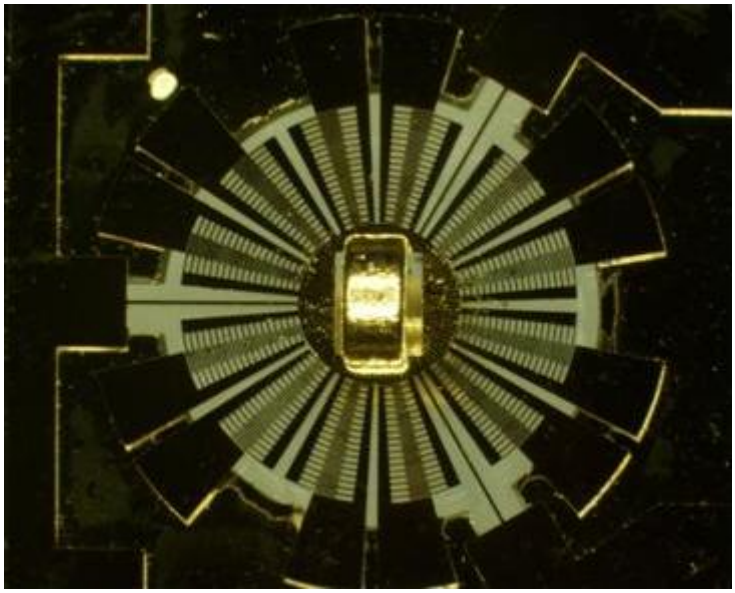

Figure 4. 11. A complete sensor picture. A permanent magnet is secured inside the trench.

4.1.3 Electromechanical model

The natural frequency of the fabricated comb drive resonator can be modeled using equation (4. 8) and Hooke's law:

$$F_x = \frac{1}{2}(V_p^2 + 2V_p \cdot V_{ac} + V_{ac}^2)\frac{\alpha \cdot N \cdot \varepsilon \cdot h}{g} = k_{\delta,l} \times x_{static} \tag{4. 9}$$

where $k_{\delta,l}$ is a lateral linear stiffness coefficient of the system and x_{static} is the static displacement of the comb drive when the mechanical torque is developed on the resonator. x_{static} is usually a very small value which is not easy to measure electronically. However at resonance, the static displacement is amplified by the quality factor, Q [77]:

$$x_{resonance} = x_{static} \cdot Q \tag{4. 10}$$

Therefore, $k_{\delta,l}$ can be expressed using equation (4. 9 - 10):

$$k_{\delta,l} = \frac{F_x}{x_{static}} = \frac{F_x}{x_{resonance}} Q \tag{4. 11}$$

The natural frequency of the resonator can be expressed using Equation (3. 26) and (4. 11):

$$f_c = \frac{1}{2\pi}\sqrt{\frac{k_l}{I}} = \frac{1}{2\pi}\sqrt{\frac{N \cdot k_{\delta,l} \cdot r_{si}^2}{I}} = \frac{1}{2\pi}\sqrt{\frac{N \cdot F_x \cdot r_{si}^2}{x_{resonance} \cdot I} Q} \tag{4. 12}$$

where N is the number of beams and I is the mass moment of inertia of the resonator which can be calculated using equation (3. 9).

4.1.4 Measurements

A fabricated resonator is assembled with a permanent magnet as shown in Figure 4. 11. The excitation ports are then connected to the power supply to provide both the AC

(V_{ac}) and DC (V_p) voltages (Figure 4. 12). A 50 V DC voltage is supplied along with 5 V_{pp} AC voltage to excite the resonator. The quality factor, Q, is calculated to be 950 from the measurement. F_x is calculated to be 2.89 μN using Equation (4. 9) and $k_{\delta,l}$ is 44.07 using the measured displacement at resonance of 20 μm. From the equation (4. 12), the resonant frequency is 1782.00 Hz.

A commercially available Hall-Effect sensor (Allegro 3503) is used to measure the resonant frequency of the fabricated silicon resonator on which a permanent magnet is glued. Figure 4. 12 shows a schematic of the overall measurement setup. The gap between the permanent magnet and the Hall-Effect sensor is about 100 μm which is close enough for the Hall-Effect sensor to detect the vibratory movement of the permanent magnet (Figures 4. 13 - 14).

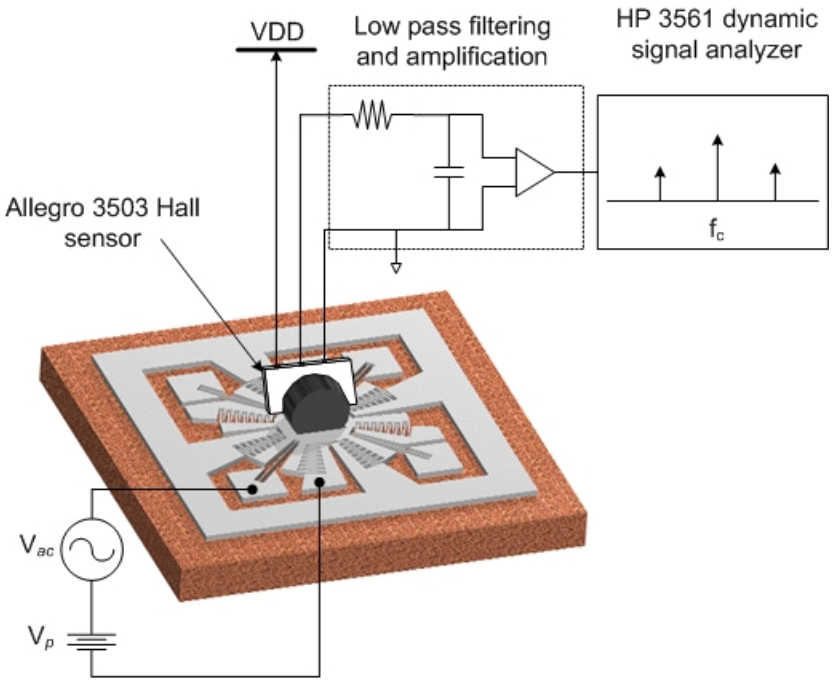

Figure 4. 12. Configuration of resonant frequency measurement using Hall sensor.

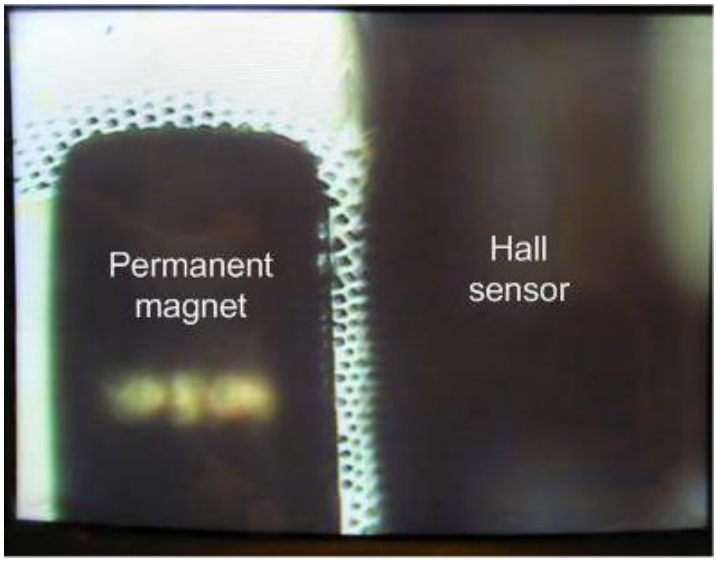

Figure 4. 13. Relative position of Hall-Effect sensor to the permanent magnet.

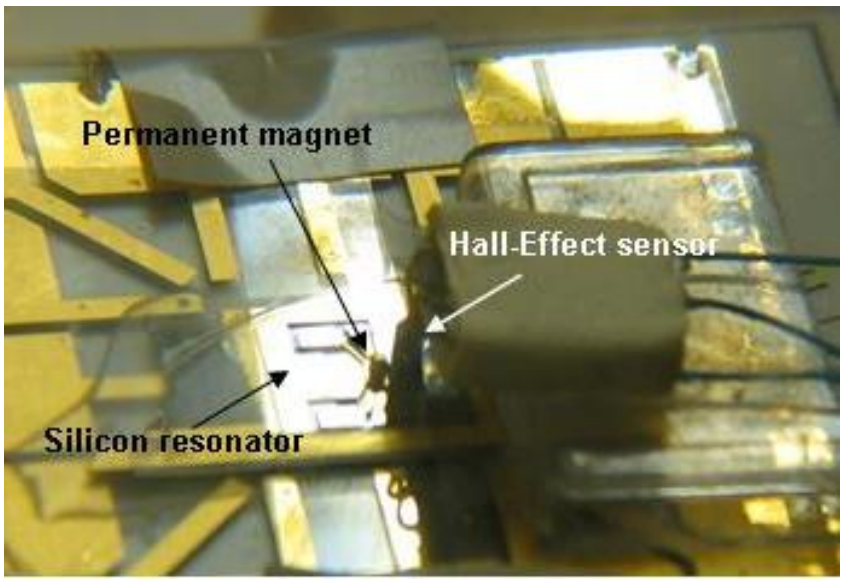

Figure 4. 14. The assembly of the Hall-Effect sensor with resonator.

The output signal from the Hall-Effect sensor is passed through a low pass filter to remove the high-frequency noise. The output signal of the Hall-Effect sensor is completely isolated from the excitation port, in other words, the Hall-Effect sensor only responds to the time-varying magnetic field generated by the movements of the permanent magnet not to the excitation signal of the input port. The resonant frequency is monitored using an HP 3561 dynamic signal analyzer.

A solenoid coil is built to provide a uniform external magnetic field (Figure 4. 15). The magnetic flux density inside the solenoid coil is measured at several DC current and plotted in Figure 4. 16.

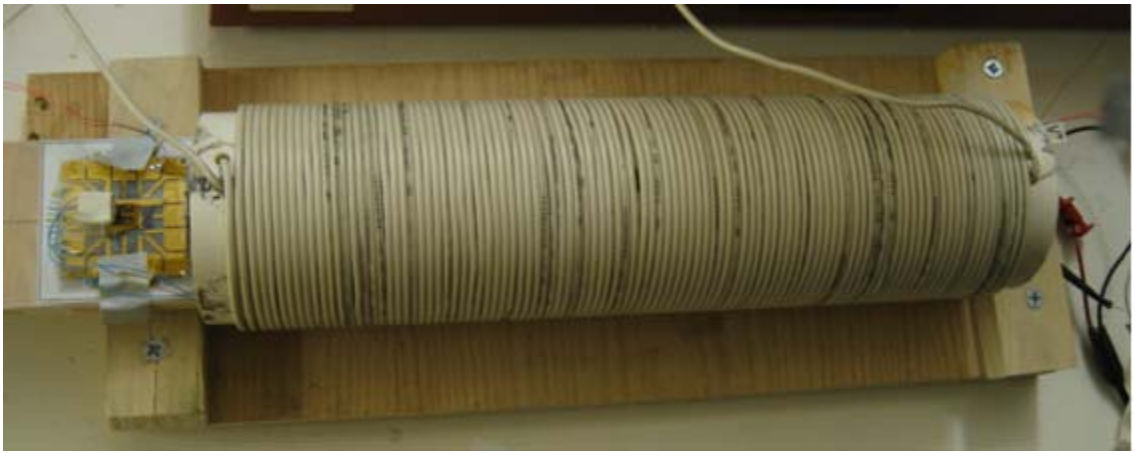

Figure 4. 15. A solenoid coil is used to provide uniform external magnetic field. The magnetic sensor is placed inside the solenoid coil and tested with various rotational angles.

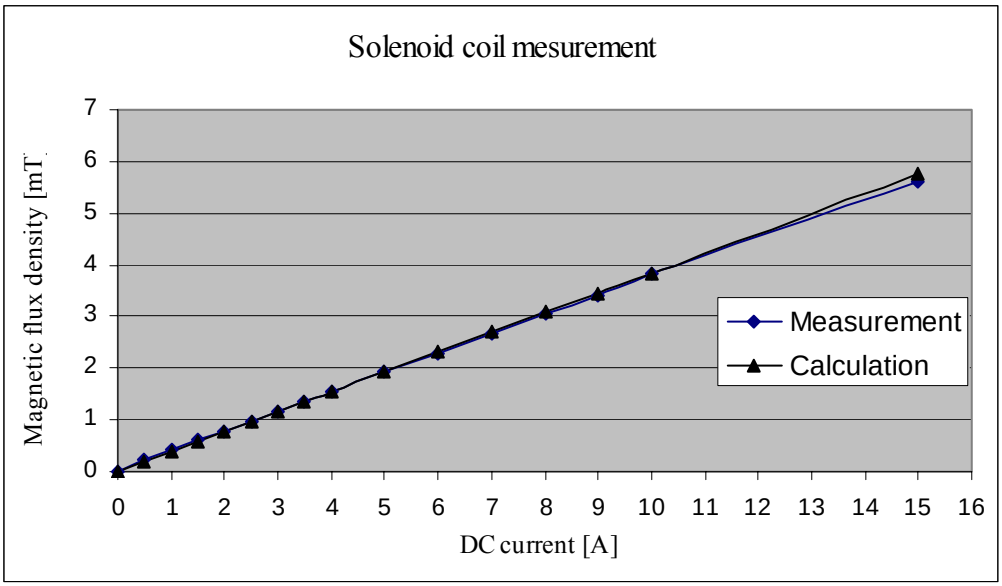

Figure 4. 16. Solenoid coil measurement.

The device is placed inside the solenoid coil and the resonant frequency is measured every 22.5 rotational degree. The output signals on the HP 3561 dynamic signal analyzer are clearly distinguishable whether the resonator is resonating or not (Figure 4. 17). The resonant frequency is plotted in Figure 4. 18. The sensitivity is normalized to the resonant frequency measured when the θ is zero (Table 4. 4). The normalized sensitivity calculated over 180° ~ 360° is higher than that calculated for 0° ~ 90°. All of the beams do not have exactly the same dimensions after fabrication even though they are designed to be the same. These unbalanced beams cause unequal amounts of rotation for the same magnitude torques (both clockwise and counter clockwise). Therefore, the resonant frequency curves are not perfectly symmetric about y

axis at 180 degree of the θ. A high DC voltage requirement of the electrostatic resonator is the one of the drawbacks for the possible mobile applications.

4.1.5 Conclusions

A comb drive torsional resonator is fabricated and tested to measure the direction of the external magnetic field. The resonator was driven electrostatically and sensed using Hall-Effect sensor. An electromechanical model was developed to analyze the actuation of the comb drive. The resonant frequency of 1782 Hz was calculated from this model. However, the measured resonant frequency is 2370 Hz. The discrepancy is mainly attributed to fabrication tolerance. For example, non-uniform beam width and slightly off positioned permanent magnet can result in a mass moment of inertia different from the calculation. Even though the fabricated comb drive resonator is demonstrated as a magnetic sensor measuring the direction of the external magnetic field, high DC voltage used is not compatible with most mobile devices, such as a wristwatch. To reduce the excitation voltage, the gap of the comb drive fingers needs to be narrowed. However, there is a minimum gap which is limited by fabrication. For example, the ICP silicon etching process in Georgia Tech cleanroom can create a uniform gap of 20 μm up to 200 μm in thickness. Therefore, electrostatic actuation is not preferred for a high aspect ratio mechanical resonator whose operation voltage is provided from conventional small battery, such as wristwatch battery.

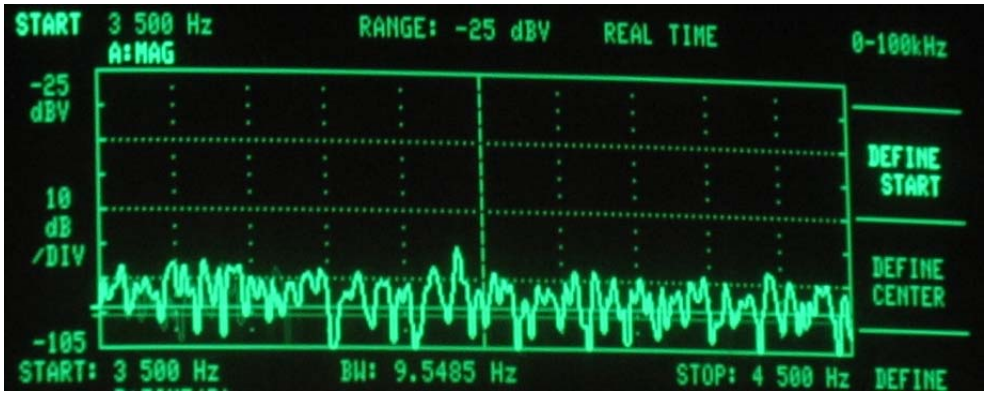

(a)

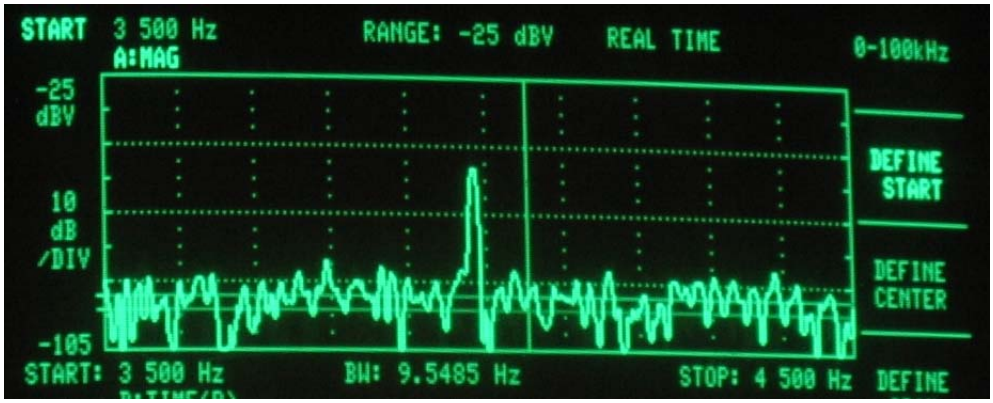

(b)

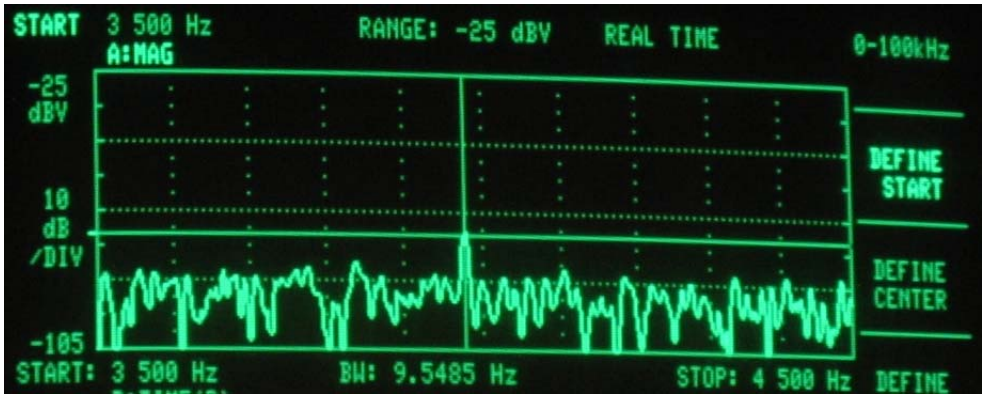

(c)

Figure 4. 17. Output signal on HP 3561 dynamic signal analyzer. (a) Before the resonance, (b) at resonance, and (c) after resonance.

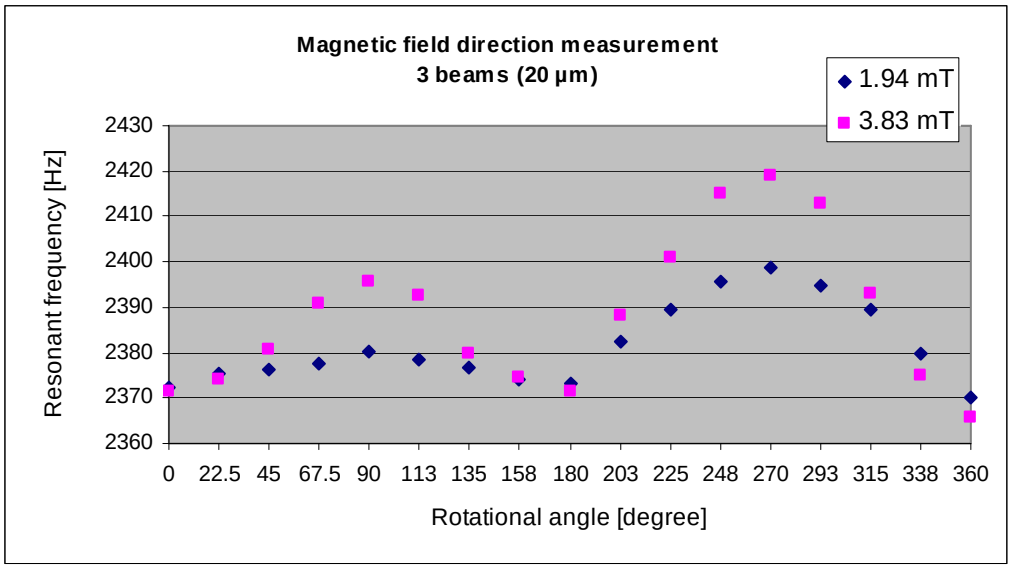

Figure 4. 18. A magnetic field direction measurement at the external magnetic field of 1.94 mT and 3.83 mT.

Table 4. 4. Comparison of the normalized sensitivities. The unit of the sensitivity is [mHz/(Hz·degree)].

	1.94 mT	3.83 mT
0° ~ 180°	0.038	0.114
180° ~ 360°	0.118	0.224

4.2 Magnetically excited and sensed micromachined resonant magnetic sensor

A micromachined resonant magnetic sensor was fabricated and tested with electromagnetic actuation and search-coil sensing which enables a low voltage actuation along with low power consumption.

4.2.1 Electromagnetically excited resonator

An electromagnetic actuator typically has low power consumption [5] and yet produces a large displacement [7, 78] of more than 50μm. Furthermore, the electromagnetic actuator enables low actuation voltage which is desirable in many applications such as an integrated circuits to reduce noise or eliminate the need for voltage converters [79]. The electromagnetic actuator has practical MEMS applications in magnetic sensors [80], optical switches [81, 82], RF switches [83], and micro-valves [84]. An example of the electromagnetic actuation is shown in Figure 4. 19. An electroplated polymer magnet is suspended over the integrated planar coil structure. A static deflection and resonant frequency was measured by flowing direct current (DC) and alternating current (AC) through the planar coil respectively [85].

Most of the magnetic actuators developed so far utilize soft magnetic materials [85]. However, hard magnetic materials such as permanent magnets are desirable for application of larger forces and deflections [85]. Magnetic actuation using permanent magnet has been reported either using hybrid assembled, commercially available permanent magnets [86-88], or using electroplated CoNiMnP permanent magnets[89].

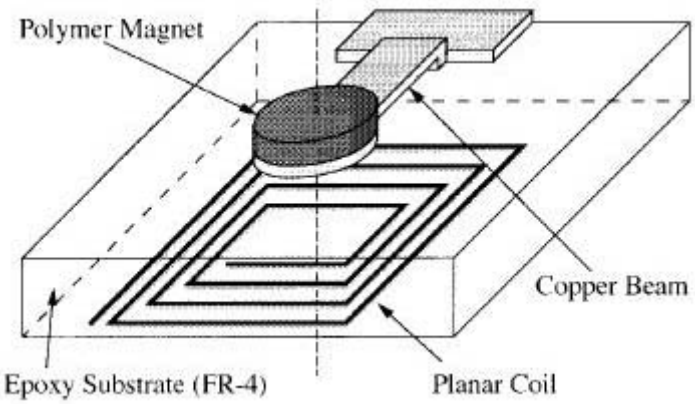

Figure 4. 19. Schematic view of the cantilever beam microactuator [85]. A polymer magnet magnetized in thickness direction is screen-printed onto the free end of a copper cantilever beam.

4.2.2 Design and FEM simulation

As is discussed in Chapter 3, the sensitivity of the resonant magnetic field sensor is determined by several parameters such as beam width, beam length, and thickness. To make the resonator vibrate with its lateral mode as the primary resonant mode, a high aspect ratio beam is designed, *i.e.*, the width of beam is relatively small compared to the height of the beam. The sensitivity of a laterally moving resonator is greatly changed by changing the width of the beam (Table 3. 3). The normalized sensitivities summarized in Table 3. 3 are represented in Figure 4. 20. Four different designs are used to characterize the relations of the sensitivity to the geometrical parameter, *i.e.*, beam width (Table 4. 5). ANSYS is used to determine the dimensions of the resonator so that it resonates with the expected resonant frequency (Figure 4. 21).

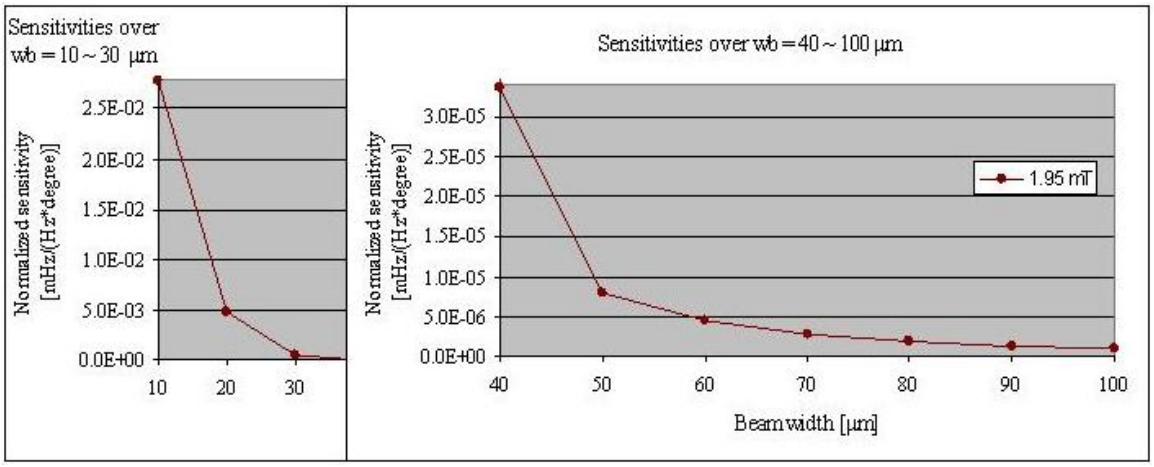

Figure 4. 20. Sensitivities over 10 to 100 μm in beam width for the four beams structures (more details are found in Table 3. 3).

Table 4. 5. Design parameters and simulation results.

	Design A	Design B	Design C	Design D
Number of beams	3	4	8	16
Width of the beam	21.2 μm	21.4 μm	19.6 μm	15.0 μm
Length of the beam	2 mm	2 mm	2 mm	2 mm
Thickness of the beam	200 μm	200 μm	200 μm	200 μm
Resonant frequency [Hz] (simulation)	2014.21	2352.9	2910.8	2737.43
Resonant frequency [Hz] (measurement)	2102	2492	2989	2802.5

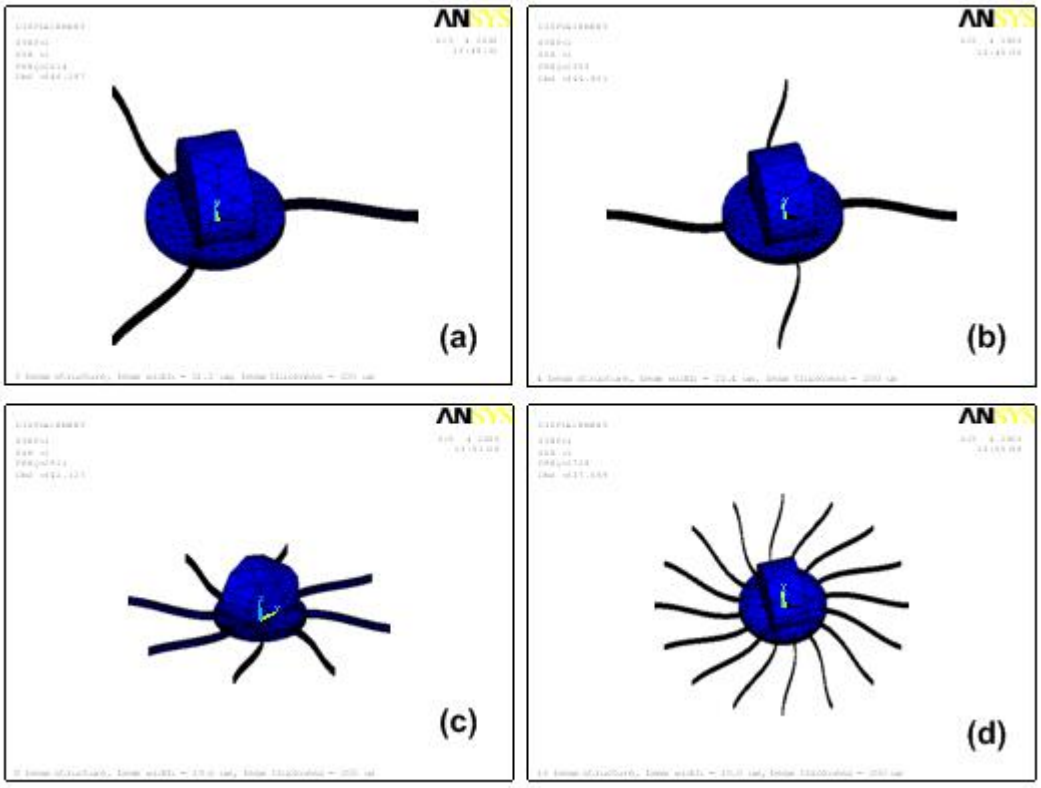

Figure 4. 21. ANSYS simulated design. (a) 3 beam, (b) 4 beam, (c) 8 beam, and (d) 16 beam structures.

4.2.3 Electromagnetic modeling

The natural frequency of the fabricated resonator can be modeled using magnetic toque and mechanical torque developed on the resonator:

$$T_{mechanical} = k_{\varphi}\, \varphi_{static} \tag{4. 13}$$

$$T_{magnetic} = (\vec{M} \times \vec{B}) \cdot V_{magnet} \tag{4. 14}$$

where V_{magnet} and M is the volume and magnetization of the magnet, respectively. B is the magnetic field generated from the excitation coil which can be approximated using Biot-Savart law (Figure 4. 22) [90] :

$$B_z \cong \frac{\mu_0 \cdot I \cdot r^2}{2\left(z^2 + r^2\right)^{3/2}} N \tag{4. 15}$$

where μ_0 is the permeability of free space, z is the distance from coil to a point on the axis of a circular loop of radius r that carries a direct current I, and N is the number of turns of the coil. In measurement setup, the distance from excitation coil to the permanent magnet is approximately 5 mm and the direction of B_z is perpendicular to the direction of M.

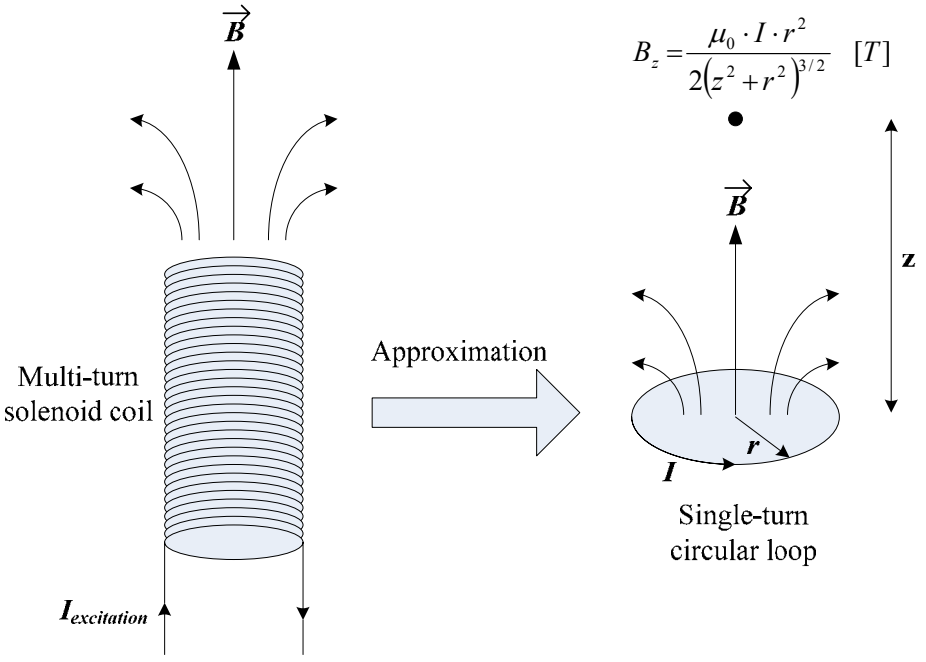

Figure 4. 22. Approximated model for an electromagnetic actuation.

When the resonator reaches its equilibrium position, the mechanical torque and magnetic torque are the same in magnitude. Since B_z and M are perpendicular, k_φ can be calculated as,

$$k_\varphi = \frac{T_{mechnical}}{\varphi_{static}} = \frac{T_{magnetic}}{\varphi_{static}} = \frac{MV_{magnet}B_z}{\varphi_{static}} \tag{4. 16}$$

and φ_{static} is the static rotation of the resonator at equilibrium. φ_{static} can be calculated from the measured Q (626.38) and $\varphi_{resonance}$, angle displacement at resonance:

$$\varphi_{static} = \frac{\varphi_{resonance}}{Q} \tag{4. 17}$$

where $\varphi_{resonance}$ is set to be 0.02 radian (1.146°).

The natural frequency of the resonator can be given as:

$$f_c = \frac{1}{2\pi}\sqrt{\frac{k_\varphi}{I}} = \frac{1}{2\pi}\sqrt{\frac{MV_{magnet}B_z}{\varphi_{resonance}\cdot I_{moment}}Q} \tag{4. 18}$$

Numerical values in Table 4. 5 are inserted above equations to calculate the resonance frequency:

$$I = \frac{V_{ext}}{R_{coil}} = \frac{0.2}{6.6} = 30.3\ mA \tag{4. 19}$$

$$B_z \cong \frac{4\pi\cdot(10^{-7})\cdot(0.0303)\cdot(0.0005^2)}{2\left(0.005^2+0.0005^2\right)^{3/2}}300 = 11.25\,\mu T \tag{4. 20}$$

$$k_\varphi = \frac{M\cdot V_{magnet}\cdot B_z}{\varphi_{resonance}}Q = \frac{1.51\cdot(10^{-3})\cdot(11.25)\cdot(10^{-6})}{0.02}626.38 = 532.03\cdot(10^{-6}) \tag{4. 21}$$

$$f_c = \frac{1}{2\pi}\sqrt{\frac{k_\varphi}{I}} = \frac{1}{2\pi}\sqrt{\frac{532.03\times10^{-6}}{3.285\times10^{-12}}} = 2025.44\ Hz \tag{4. 22}$$

Calculated k_φ (532×10^{-6}) is very close to the numerical value (581×10^{-6}) from the FEM simulation (Table 3. 6), demonstrating good approximation of the solenoid excitation coil with single turn circular loop using the Biot-Savart law. The calculated resonant frequency is 2025.44 Hz (Equation 4. 22) and the measured resonant frequency is 2492 Hz (Figure 4. 29). The discrepancy is mainly attributed to fabrication tolerance. For example, non-uniform beam width and slightly off positioned permanent magnet can result in a mass moment of inertia different from the calculation.

4.2.4 Fabrication and assembly

Fabrication of the mechanical resonator is similar to that of the comb-drive structure except that a comb-drive structure and an electrical isolation layer are not required any more. Therefore, the Wafer fusion bonding process is not used for this fabrication process. The processing time is reduced and fewer materials are consumed as compared to the electrostatically excited comb-drive devices since only one single wafer is used without wafer bonding process. One or two photo lithography processes are used depending on whether the back side of the silicon is etched or not.

Fabrication starts with silicon etching to form a beam structure and the movable resonant disc structure which contains the recess for the permanent magnet (Figure 4. 23 (A)). The magnet is glued on the center of the resonator (Figure 4. 23 (B)) followed by the excitation and detection coil assembly (Figure 4. 23 (C)). A magnet wire is wound by hand to make both the excitation and detection coils (Figure 4. 24).

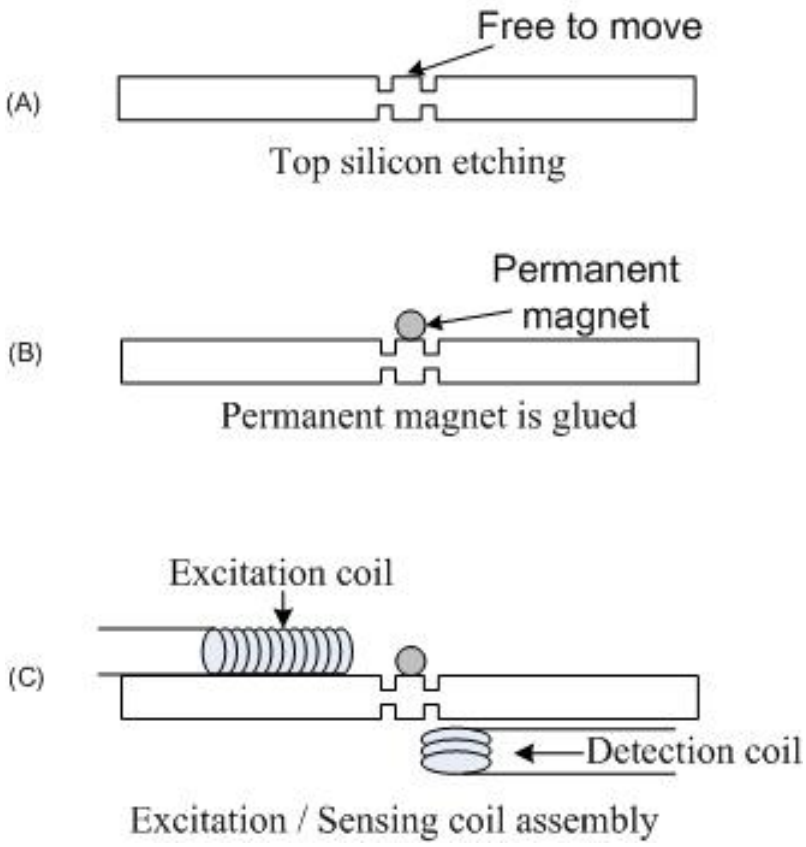

Figure 4. 23. Fabrication sequences of the mechanical resonator structure.

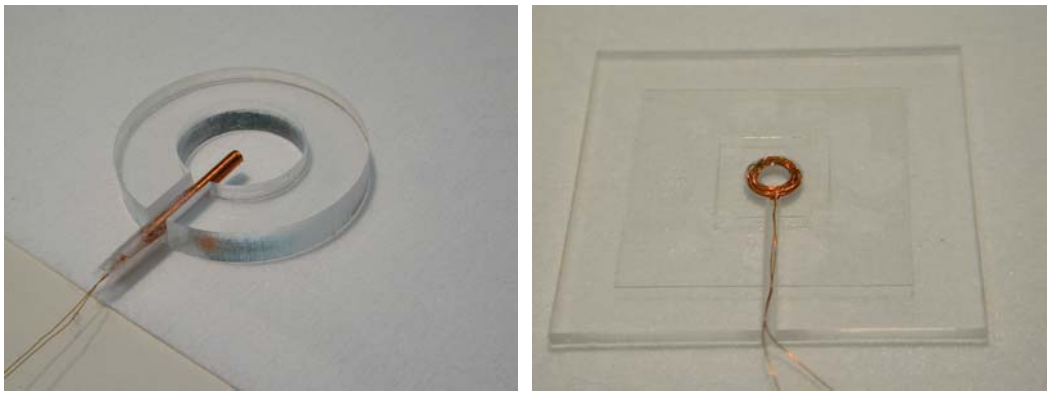

(a) Excitation coil (b) Sensing coil

Figure 4. 24. Excitation and sensing coils.

Both the excitation and sensing coils are secured onto the acryl plate not to move during the measurement. The dimensions of the coils are shown in Table 4. 6. Figure 4. 25 shows the images of the fabricated devices which have three, four, eight, and sixteen beams, respectively.

Table. 4. 6. Parameters of the excitation and sensing coils.

	Excitation coil	Detection coil
Number of turns	300	30
Resistance [Ω]	6.6	2.5
Inductance [μH]	16.5	5
Length [mm]	20.28	2
Diameter [mm]	1.0	7

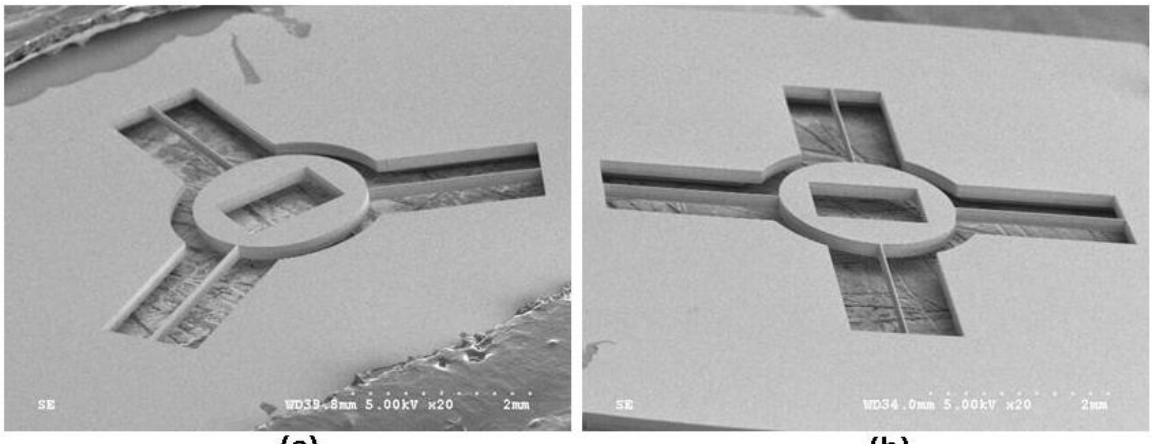

(a) (b)

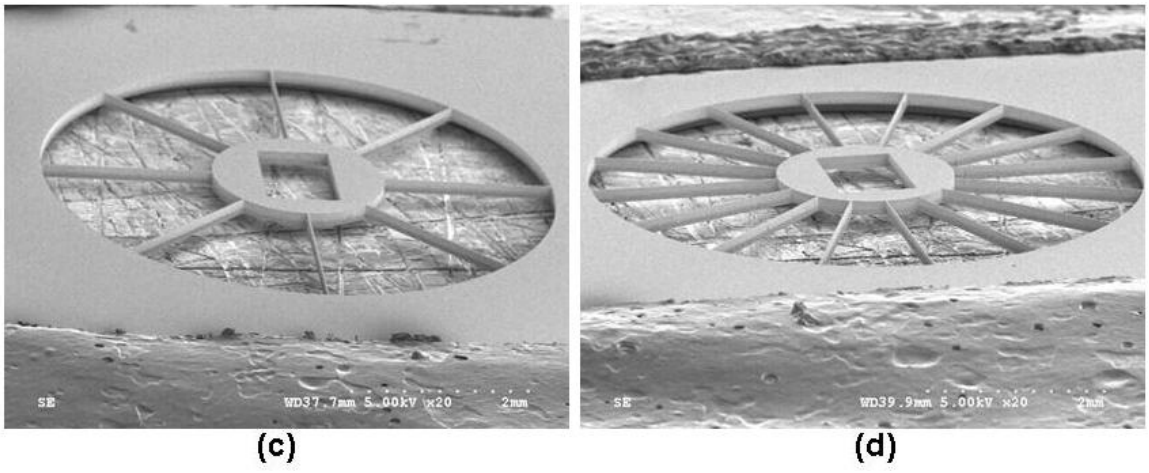

Figure 4. 25. The SEM images of the fabricated resonators. (a) 3 beam structure, (b) 4 beam structure, (c) 8 beam structure, and (d) 16 beam structure.

4.2.5 Open loop measurements

The fabricated devices are measured in two different ways: 1) open loop configuration (Section 4. 2), 2) closed loop configuration (Chapter 5). A position of the detection coil relative to the excitation coil and the permanent magnet is important to avoid the crosstalk between those coils and to maximize the signal output from the detection coil (Figure 4. 26). A magnitude of the excitation signals need to be small for the small oscillation but high enough for the excitation. The self resonating sensing systems are enabled using a positive closed loop feedback configuration (Chapter 5). The sensor is measured at several different external magnetic field at each rotation angle of 30 degree. A measurement configuration is shown in Figure 4. 26. The excitation coil is connected directly to the function generator which provides time varying sinusoidal or

square wave signal. The output signal is monitored through the HP 3561A dynamic signal analyzer in which the spectrum analysis is performed from 125 μHz to 100 kHz.

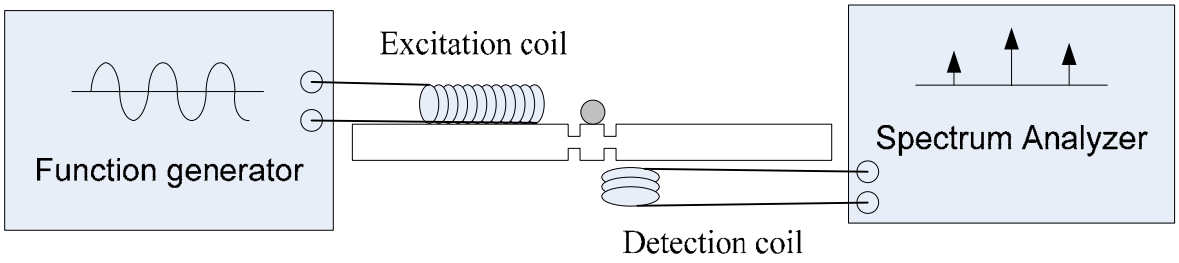

Figure 4. 26. Open loop measurement configurations. A sweeping signal is provided by the function generator to the excitation coil and the resonant frequency is monitored using spectrum analyzer (HP 3561A Dynamic signal analyzer).

A detection coil is placed under the permanent magnet to maximize a response from the oscillatory movement of the permanent magnet while minimizing coupling with the excitation coil (Figure 4. 27). The detection coil is placed well below the beam structure so that it is not disturb the movement of the beams. The input and output ports of the resonator are physically isolated from each other. The excitation coil is placed in plane with the permanent magnet (Figure 4. 28).

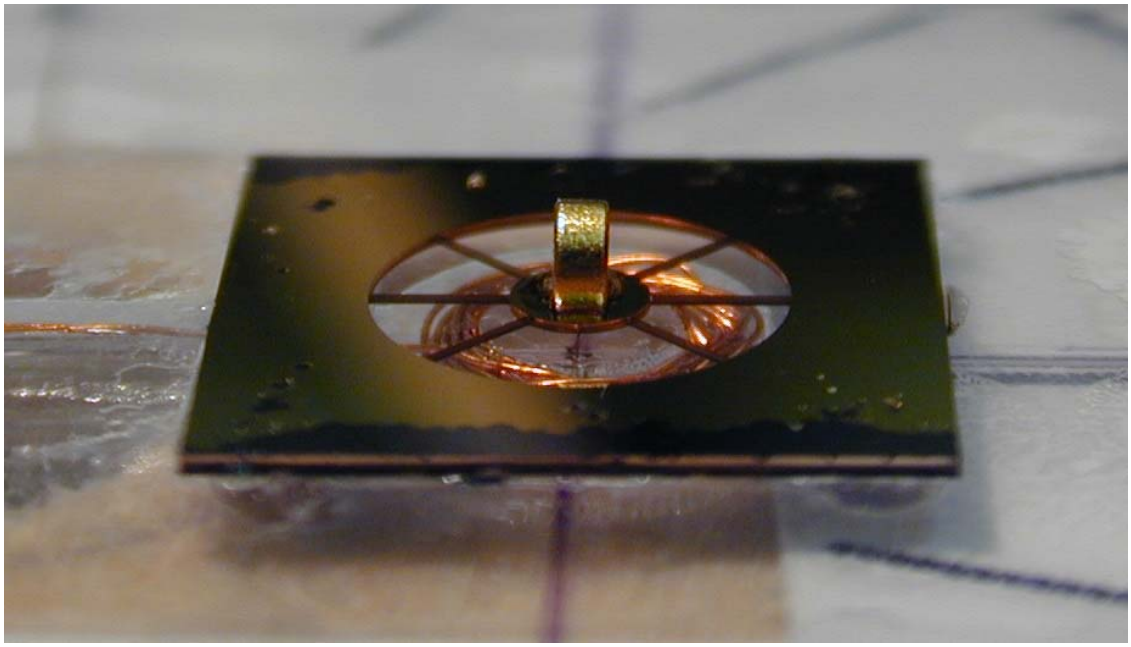

Figure 4. 27. The detection coil is placed under the permanent magnet.

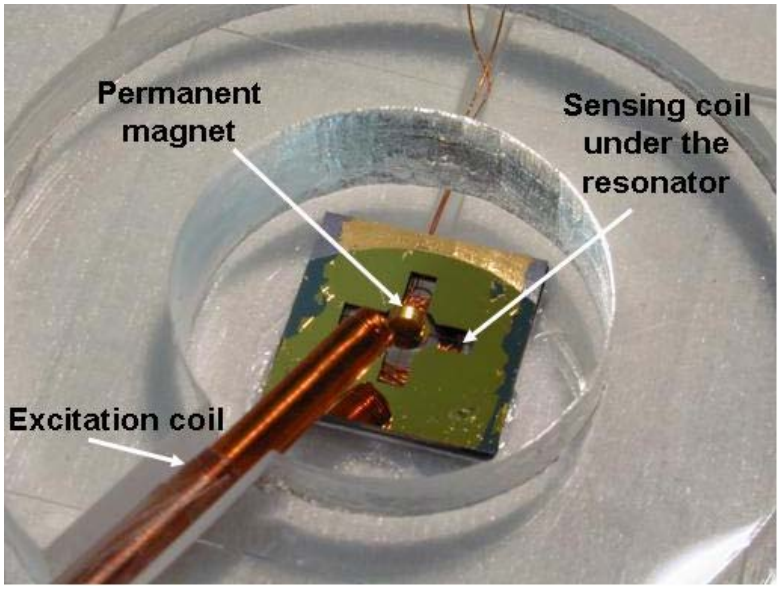

Figure 4. 28. Complete open loop measurement system. The excitation coil is placed in plane with magnet while the detection coil is located under the magnet to minimize the crosstalk between those two coils.

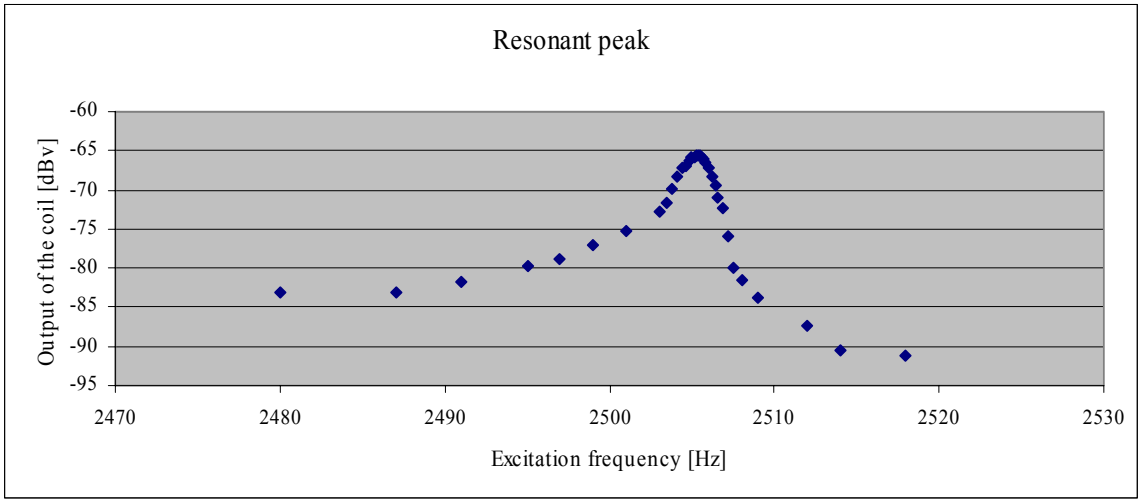

Figure 4. 29. Resonant peak of the resonator. The *Q* factor of the resonator is calculated to be 626.38.

The measurement is performed inside the solenoid coil in which a uniform external magnetic field is generated. The device is measured at every 30 degrees rotation (Figure 4. 30 – 4. 33). External magnetic field of the 0.975 mT and the 1.95 mT is uniformly generated inside solenoid coil by applying suitable DC current. The normalized sensitivity is calculated and shown in Table 4. 7.

Table 4. 7. Normalized sensitivities [mHz/(Hz·degree)].

	0.975 mT		1.95 mT	
Number of beam	0° ~ 180°	180° ~ 360°	0° ~ 180°	180° ~ 360°
3	0.880	0.680	2.23	2.02
4	0.068	0.112	0.325	0.357
8	0.070	0.027	0.231	0.147
16	0.128	0.089	0.401	0.289

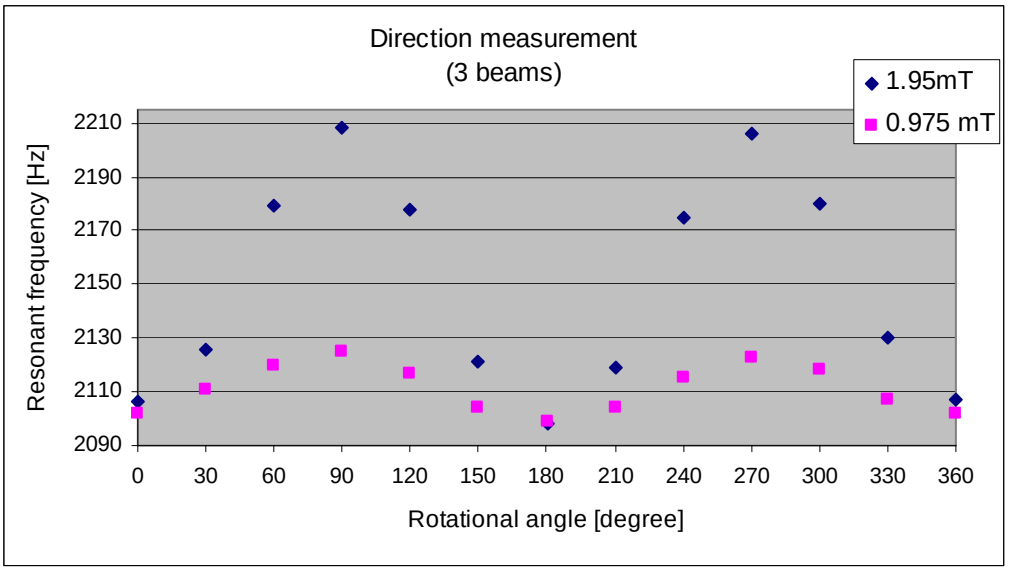

Figure 4. 30. Measurement result for the 3 beam structure. The resonant frequency is 2102 Hz at $\theta = 0°$.

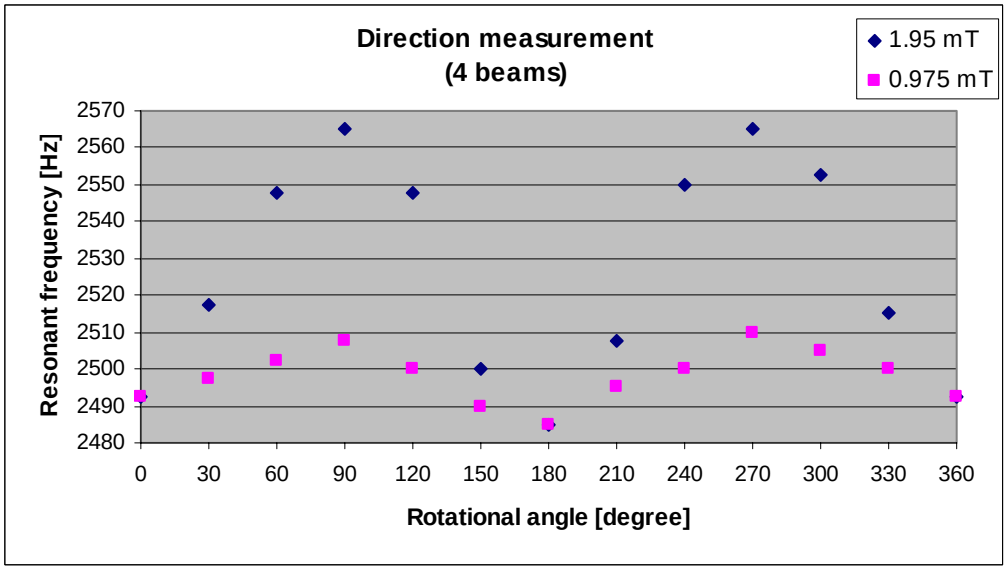

Figure 4. 31. Measurement result for the 4 beam structure. The resonant frequency is 2492 Hz at $\theta = 0°$.

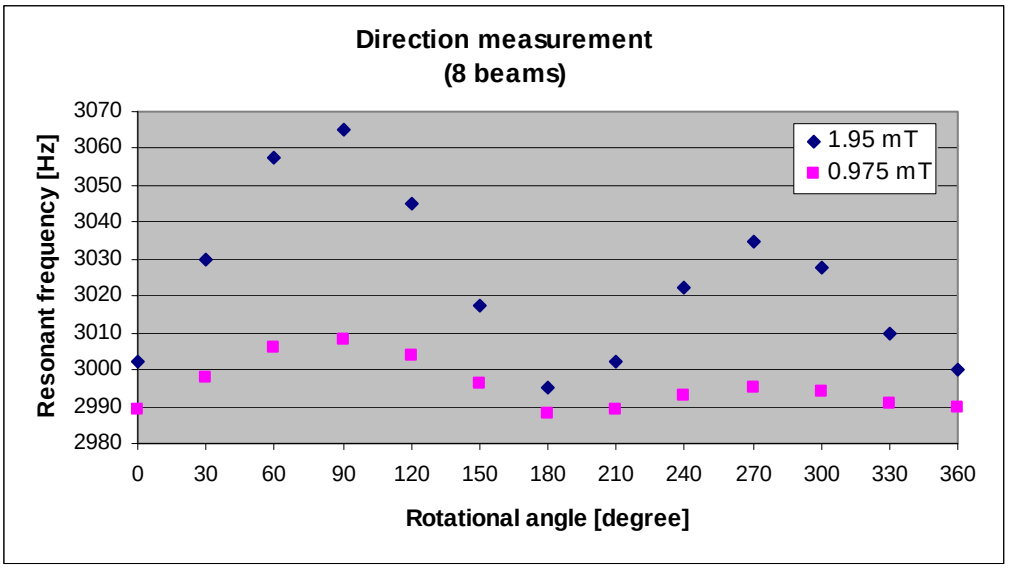

Figure 4. 32. Measurement result for the 8 beam structure. The resonant frequency is 2989 Hz at $\theta = 0°$.

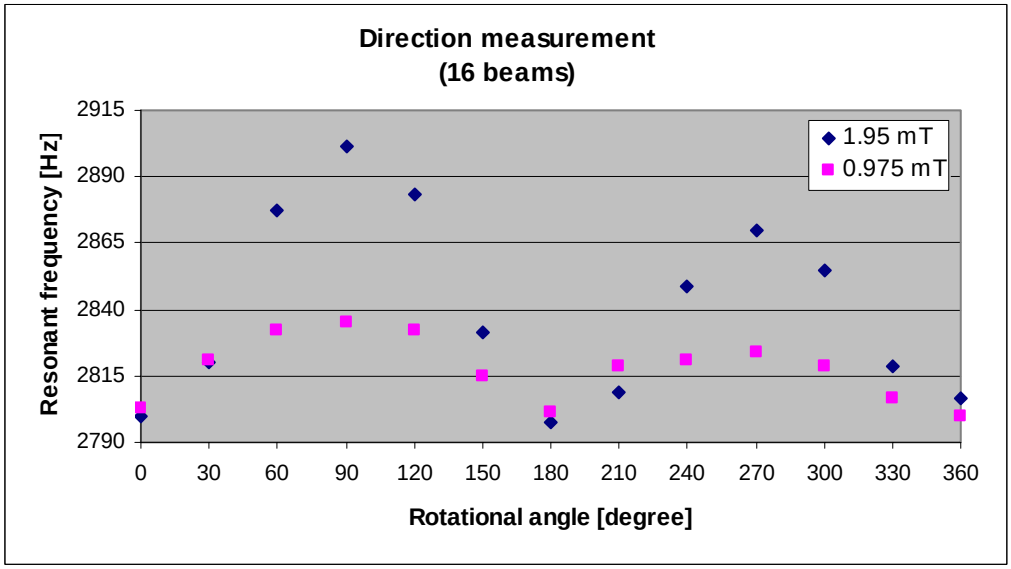

Figure 4. 33. Measurement result for the 16 beam structure. The resonant frequency is 2802.5 Hz at $\theta = 0°$.

4.2.6 Comparison between FEM simulations and measurements

Measurement results are compared with predictions from the FEM simulations. Structural dimension used for FEM simulation obtained from the fabricated mechanical resonator. Predictions from FEM simulations are not exactly matched with measurement results as shown in Table 4. 8. However, FEM simulations are still useful to predict sensing performance and optimum designs. For example, FEM simulation predicts that 3 beams with 21.2 μm produce better sensing performance than 16 beams with 15 μm and the measurement results are the same (Table 4. 8). The discrepancy is mainly attributed to fabrication tolerance. For example, non-uniform beam width and slightly off positioned permanent magnet can result in a mass moment of inertia different from the calculation. Assembly of permanent magnet is another source of discrepancy since FEM simulation does not consider any effect of glue which is used for assembly of permanent magnet with resonator on stiffness change.

Table 4. 8. Comparison of normalized sensitivities between FEM and measurements.

Number of beam	beam width [μm]	FEM simulation (ANSYS)				Measurement			
						0.975 mT		1.95 mT	
		k_1 [10^{-6}]	k_{nl} [10^{-2}]	0.975 mT	1.95 mT	0 ~ 180º	180 ~ 360º	0 ~ 180º	180 ~ 360º
3	21.2	519	168	0.421	1.407	0.880	0.680	2.23	2.02
4	21.4	712	221.3	0.225	0.799	0.068	0.112	0.325	0.357
8	19.6	1100	399.4	0.114	0.420	0.070	0.027	0.231	0.147
16	15	977	571.3	0.222	0.793	0.128	0.089	0.401	0.289

4.2.7 Beam width characterization

The devices are characterized as a beam width is changed. Thinner beam is expected to give higher sensitivity since it is more compliant to the externally applied torque. Two different beam widths are selected for the 3 beam and 4 beam structures respectively. ANSYS simulations are performed to confirm the proper resonant modes of the designs (Figure 4. 34). The thinner beam structure shows the lower resonant frequency as is expected. The simulation results and the structural dimension are summarized in Table 4. 9.

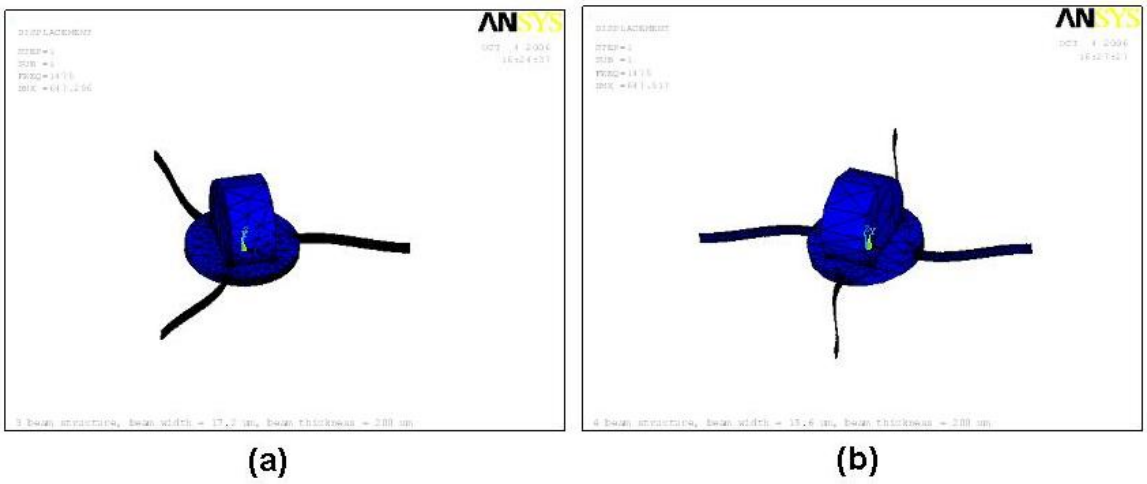

Figure 4. 34. ANSYS modal analysis. (a) 3 beam structure and (b) 4 beam structure.

Table 4. 9. Resonant frequency simulated by ANSYS. All of the devices have the same thickness of 200 μm and beam length of 2 mm.

Number of the beams	Device number	Width of the beam [μm]	Resonant frequency [Hz] (simulated)	Resonant frequency [Hz] (measured)
3	009	17.2	1475.1	1580
	017	21.2	2014.2	2102
4	018	15.6	1475.3	1498
	007	21.4	2352.9	2492.5

The measurement results confirm that thicker beam structures give higher resonant frequencies (Table 4. 10). The external magnetic field of 0.975 mT and 1.95 mT are used for these measurements.

For the three beam structures, the beam widths of the measured device are 17.2 and 21.2 μm. For the four beam structures, the beam widths of the measured device are 15.6 and 21.4 μm. The resonant frequency is measured every 30 rotational degree at the external magnetic fields of 0.975 mT and 1.95 mT, respectively. The sensitivity is decreasing as the beam width is increasing when other structural parameters are maintained the same (Figures 4. 35 - 36).

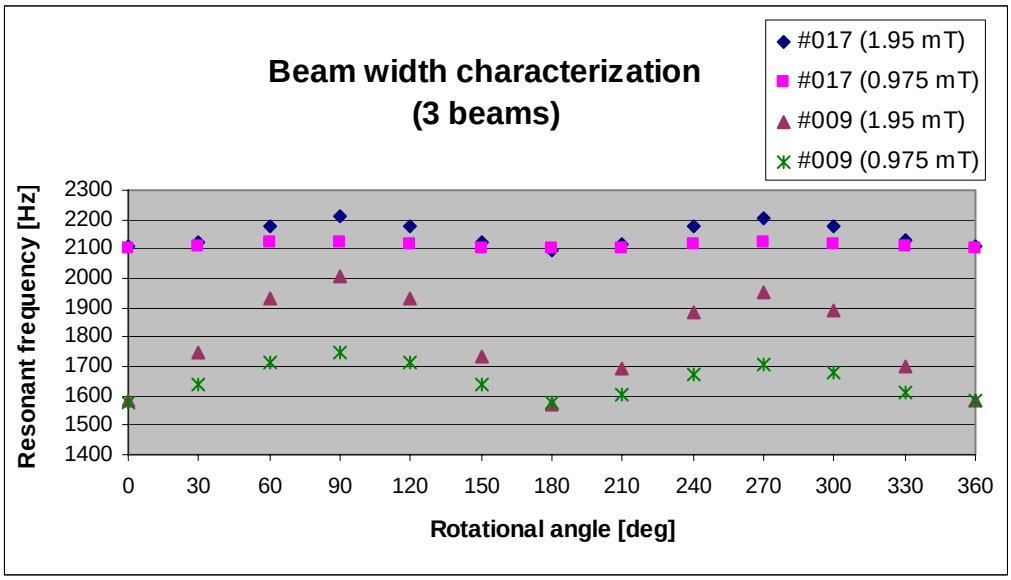

Figure 4. 35. Measurement results of the 3 beam structure.

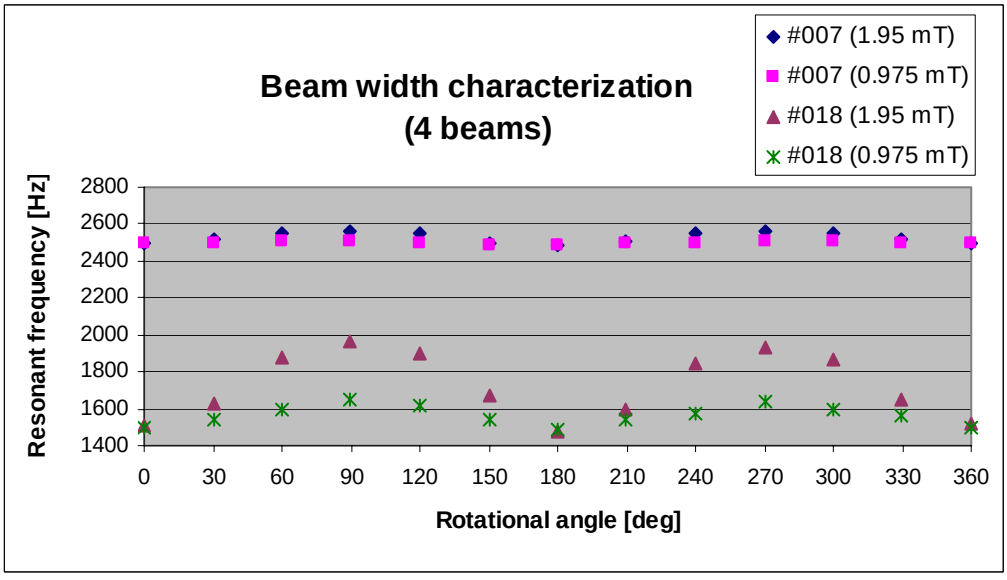

Figure 4. 36. Measurement results of the 4 beam structure.

Table 4. 10. Normalized sensitivities [mHz/(Hz·degree)].

Number of beams	Beam width [μm]	0.975 mT		1.95 mT	
		0° ~ 180°	180° ~ 360°	0° ~ 180°	180° ~ 360°
3	17.2	1.169	0.870	2.969	2.617
	21.2	0.122	0.111	0.538	0.522
4	15.6	1.142	1.068	3.319	3.07
	21.4	0.067	0.078	0.323	0.323

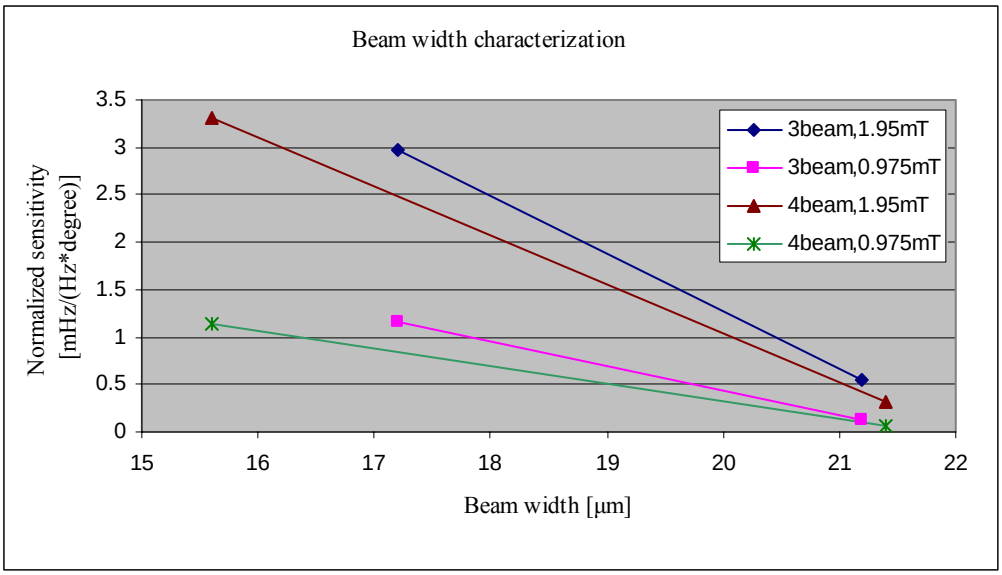

Figure 4. 37. A characterization of the beam width. Sensitivity decreases as the beam width increases for both 3 and 4 beam structures.

The normalized sensitivities are summarized in Table 4. 10. Due to the unbalanced beam width after fabrication, the measurement results show that the resonant frequency curves are not perfectly symmetric about y axis at 180 degree of the θ. Sensitivity decreases as the beam width increases both three and four beam structures (Figure 4. 37).

4.2.8 Conclusions

Resonant mechanical resonators without comb drive structure was designed and fabricated. There were four different designs in terms of numbers of beams: 3, 4, 8, and 16. The resonator was driven and sensed electromagnetically using coils to achieve low power consumption and low actuation voltage. An electromagnetic model was developed to discuss the electromagnetic actuation analytically. Sensitivity decreases as the beam width increases when no other structural parameters are changed.

CHAPTER 5

COMPLETE MAGNETIC SENSING SYSTEM WITH MAGNETIC FEEDBACK CLOSED LOOP

The micromachined resonator assembled with permanent magnet and excitation/detection coils is embedded in the magnetic feedback loop to complete the magnetic sensing system. The electronic circuitry is built to provide the positive feedback loop. The devices are characterized in terms of the number of beams and the width of the beam.

5.1 Overall system view

A resonator is often embedded in the positive feedback loop to form a self resonant oscillator system [44, 50, 91-94]. A typical configuration of the self oscillating resonator is shown in Figure 5. 1. In this configuration, the resonator is forced to oscillate at its resonant frequency without externally applied driving signal. This type of configuration is useful in many resonant sensing applications if the resonance frequency is the output signal of interest. The resonator embedded in the positive closed loop tracks the changes in the resonant frequency and oscillates at its new resonant frequency. The condition for positive feedback is that a portion of the output is combined in phase with the input.

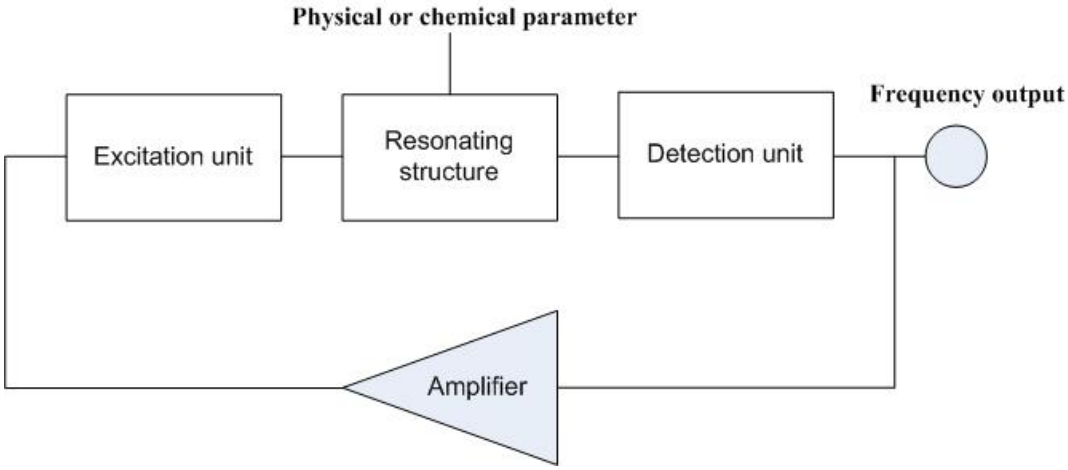

Figure 5. 1. A feedback loop configuration of resonant sensor with frequency output [95].

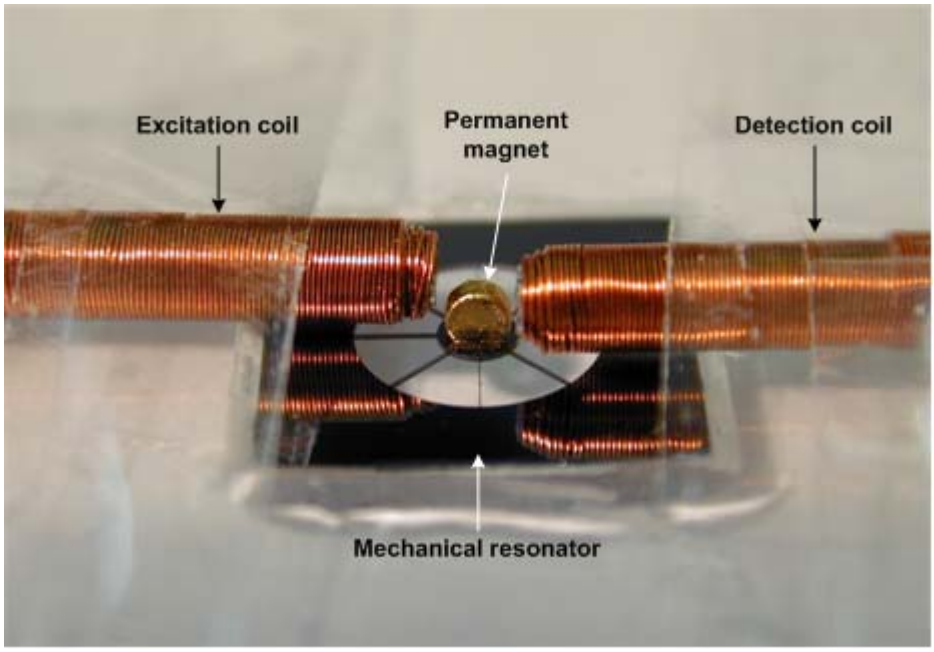

Figure 5. 2. The mechanical resonator assembled with excitation and detection coils. A permanent magnet is adhered onto the center disk of the resonator.

The Neodymium-iron-boron (NdFeB) permanent magnet is adhered to the mechanical resonator, and the excitation and detection coils are assembled with the resonator (Figure 5. 2). Electrical properties of these coils are summarized in Table 5. 1. In this configuration, the excitation and detection coils are placed in the same plane, thereby maximizing the magnetic flux linkage between the permanent magnet and the detection coil. The crosstalk between two coils is negligible in the positive closed loop configuration. Excitation coil generates a time varying magnetic field around the permanent magnet. The resonator oscillates if the natural frequency of the resonator is matched with the frequency of the time varying magnetic field generated from the excitation coil. The permanent magnet adhered to the oscillating resonator generates another time varying magnetic field. The detection coil produces the induced voltage from this time varying magnetic field generated by the oscillating permanent magnet.

The output of the detection coil is connected to the input of the positive closed loop circuit (Figure 5. 3). The output signal is amplified at the first stage of the circuit and then passed through a phase shifter and Schmitt trigger. The phase shifter adjusts the phase of the closed loop such that the output signal is fed into the excitation circuitry in phase. Both the resonant signal and noise signal which is coming out of the detection coil are amplified at this stage. This noise signal can cause malfunction of the circuitry by producing a signal with unstable frequency. The purposes of the Schmitt trigger are improving noise immunity and limiting the peak-to-peak magnitude of the excitation signal for the small oscillation of the resonator. A frequency counter is connected at the end of the circuitry to read the resonant frequency of the resonator. The mechanical

resonator works as a frequency determining element in a self oscillating amplifying feedback loop.

Table 5. 1. Properties of excitation and sensing coils.

	Excitation coil	Sensing coil
Number of turns	300	300
R [Ω]	8.5	7.24
L [μH]	45.2	37.2

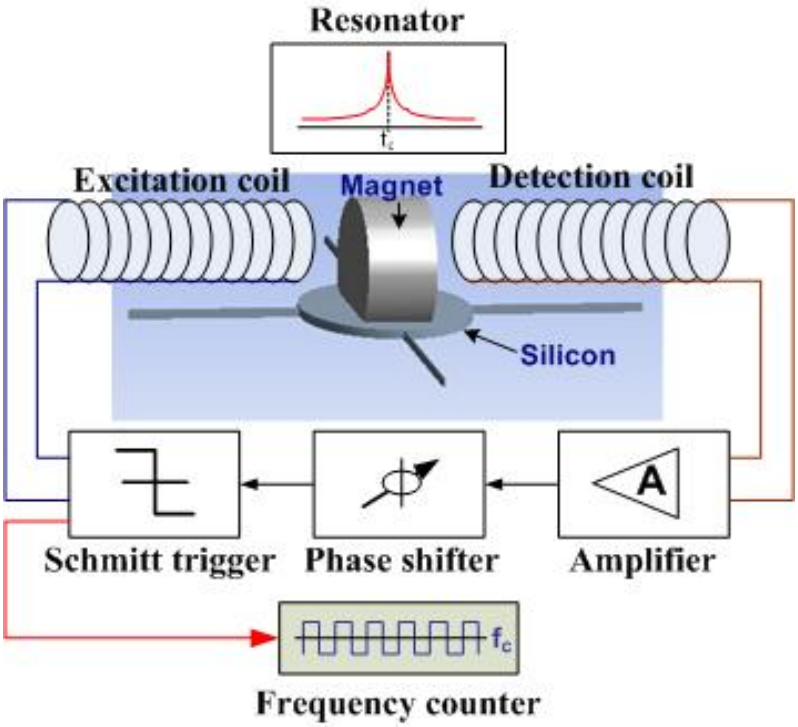

Figure 5. 3. Complete magnetic sensing systems.

All automatic measurement system is implemented using an analog wall clock (Figure 5. 4). The second hand of the watch makes full rotation continuously with the angular speed of 1 revolution per minute (RPM). The Helmholtz coils are placed on the wall clock such that the rotational axis of the magnetic resonant sensor is placed in the center between two Helmholtz coils (Figure 5. 5 (a), (b)). The sensor is placed on the center of the second hand of the wall clock. While the sensor rotates the frequency counter measures the frequency and stores it into the spreadsheet every second. An external magnetic field is applied through the Helmholtz coils.

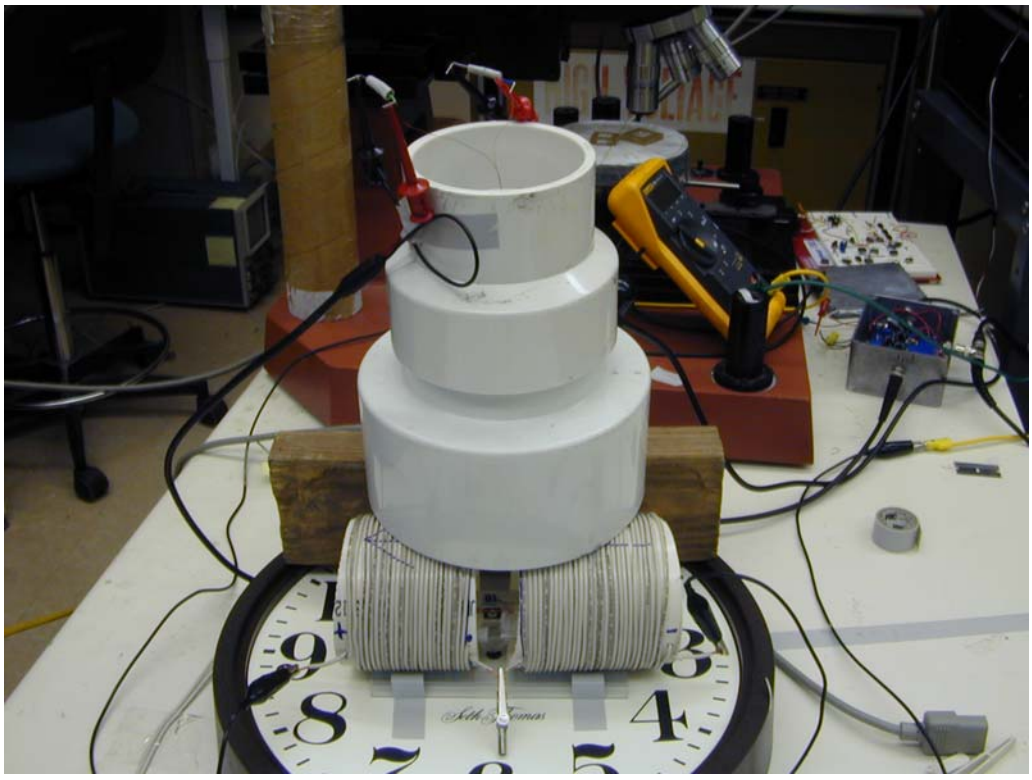

Figure 5. 4. Overall measurement systems.

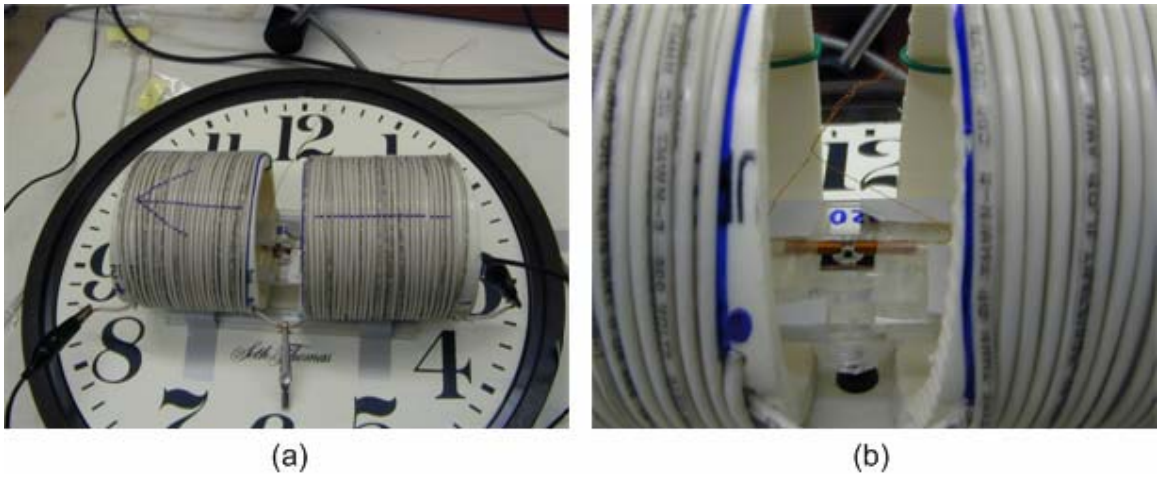

Figure 5. 5. Automated measurement systems. (a) A wall clock is utilized to build an automated rotating set up. (b) Magnetic sensor is placed on the second hand on the wall clock between Helmholtz coils. A magnified view of the sensor inside Helmholtz coils.

5.2 Positive feedback circuitry

The circuitry is composed of amplification, phase shifting, Schmitt triggering, passive voltage divider, and voltage follower functions in that order. Amplification is implemented two stage cascade op amp configurations (Figure 5. 6).

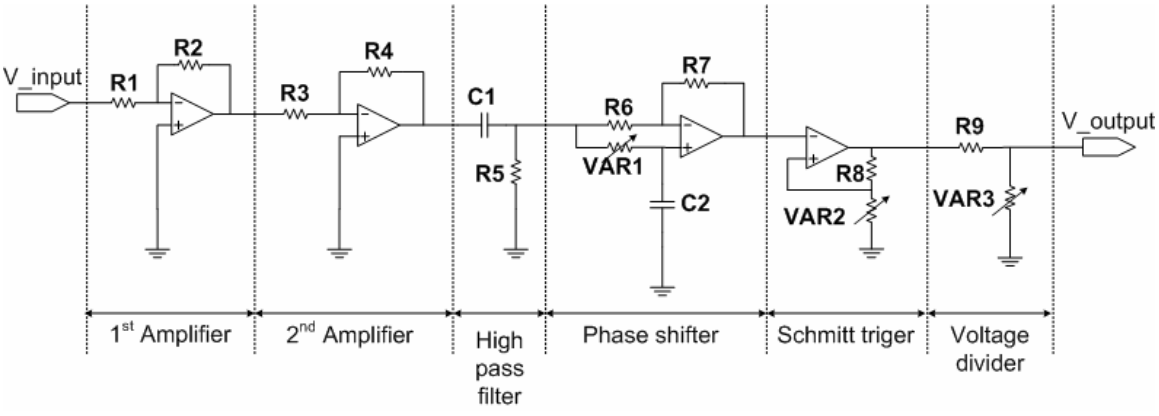

Figure 5. 6. An overview of the positive feedback circuitry.

The phase shifter shown in Figure 5. 7 produces a signal at the output V_{out} which is equal to the input V_{in} with a phase shift φ given by the following formula,

$$|\varphi| = 2\tan^{-1}(\omega C_1 R_3) \qquad (5.\ 1)$$

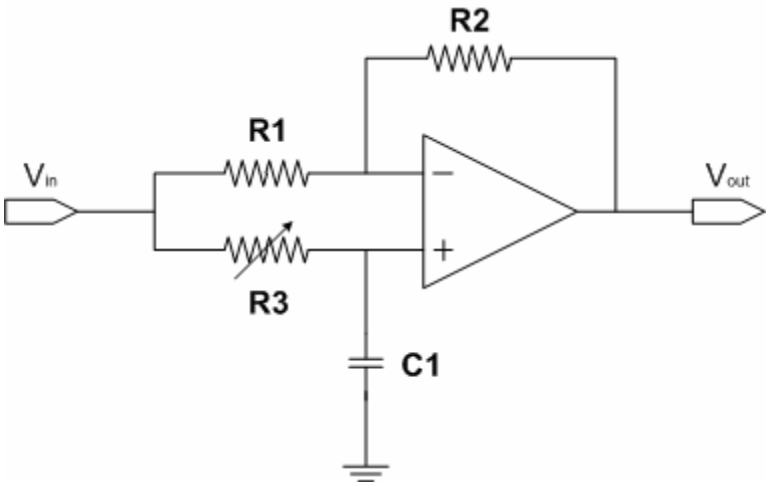

Figure 5. 7. A phase shifter circuit. Note that R2 is set to be equal to R1 to provide unit gain.

The Schmitt trigger is a comparator application which switches the output negative when the input passes upward through a positive reference voltage (Figure 5. 8). It then uses negative feedback to prevent switching back to the other state until the input passes through a lower threshold voltage, thus stabilizing the switching against rapid triggering by noise as it passes the trigger point.

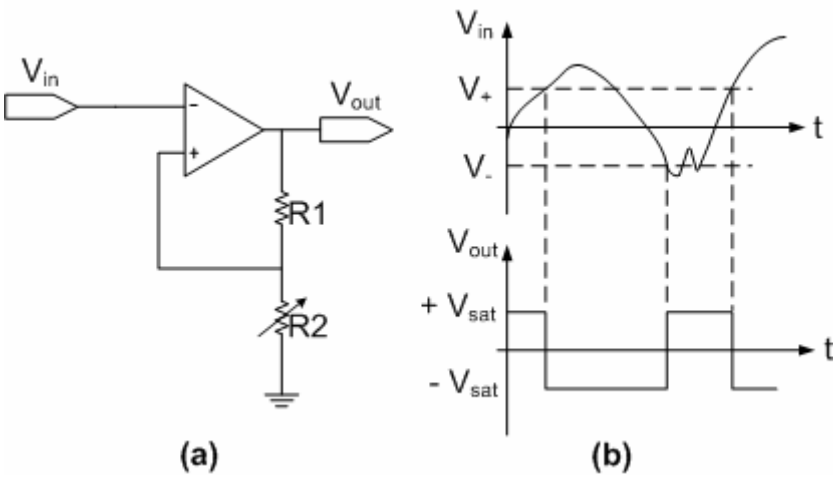

Figure 5. 8. (a) A typical Schmitt trigger circuit, (b) An example of analog to digital conversion with hysterisis.

A voltage follower is often used at the end of the circuit to connect to the load (Figure 5. 9). The effective isolation of the output from the signal source is the one of the advantages of using a voltage follower since the input impedance of the op amp is very high. Thereby it draws very little power from the signal source, avoiding "loading" effects. The voltage follower with an ideal op amp gives simply,

$$V_{out} = V_{in} \tag{5. 2}$$

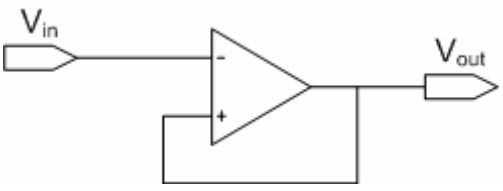

Figure. 5. 9. A typical configuration of the voltage follower. V_{out} is equal to V_{in} with ideal OP amp.

Table 5. 2. Components used for positive feedback circuitry.

R1	100 Ω	R8	1 KΩ
R2	10 KΩ	R9	1 KΩ
R3	100 Ω	VAR1	1 ~ 1000 Ω
R4	10 KΩ	VAR2	1 ~ 1000 Ω
R5	1.48 KΩ	C1	1 μF
R6	1 KΩ	C2	1 μF
R7	1 KΩ	OP AMP	TLV2461CP, OP490

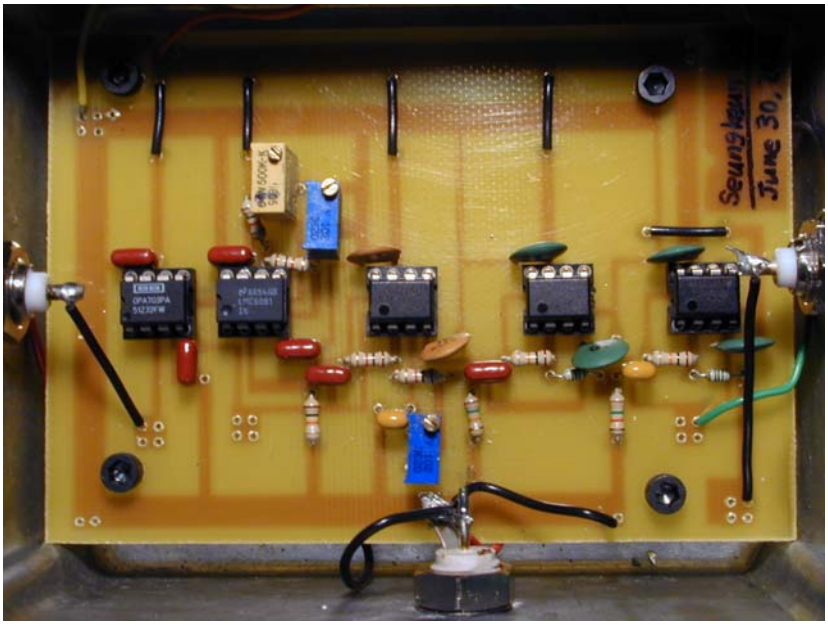

Figure 5. 10. The completed circuitry assembled onto the PCB board. The PCB board is fabricated with standard lithography and etching process on to the blank PCB board. Note that a voltage follower is added at the end of the circuitry to provide effective isolation of the inductor load, *i.e.*, excitation coil from the signal conditioning circuitry.

All the circuit components (Table 5. 2) are integrated on the PCB board to minimize electrical noises (Figure 5. 10).

5.3 Power consumption

Complete magnetic sensing system consumed 138 μW power including 0.24 μW for the actuation (Figure 5. 11). Supplied voltage and current were measured from the power supply directly and multiplied to calculate the power consumption of complete magnetic sensing system.

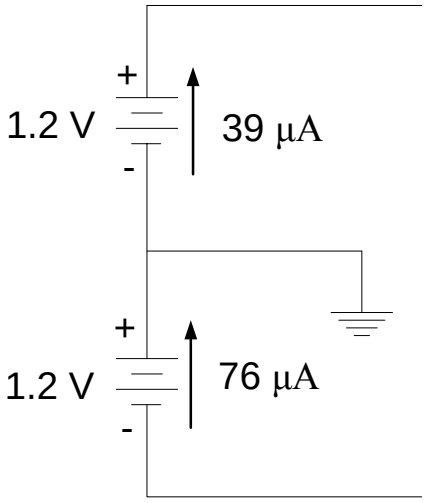

Figure 5. 11. Measurement of power consumption of complete magnetic sensing system.

Power consumption for the excitation is calculated using following Equations (Figure 5. 12),

$$V_{ext,pp} = 4.0 \text{ mVpp} \tag{5. 3}$$

$$V_{ext,max} = 2.0 \text{ mV} \tag{5. 4}$$

$$V_{ext,rms} = \frac{v_{ext,\max}}{\sqrt{2}} = \frac{0.002}{\sqrt{2}} \tag{5. 5}$$

$$I_{excitation,rms} = \frac{V_{ext,rms}}{R_{coil}} = \frac{0.002}{8.5\sqrt{2}} = 166.4\,\mu A \tag{5. 6}$$

$$P_{excitation} = I^2_{excitation,rms} \cdot R_{coil} = (166.4\,\mu)^2 \cdot 8.5 = 0.24\,\mu W \tag{5.7}$$

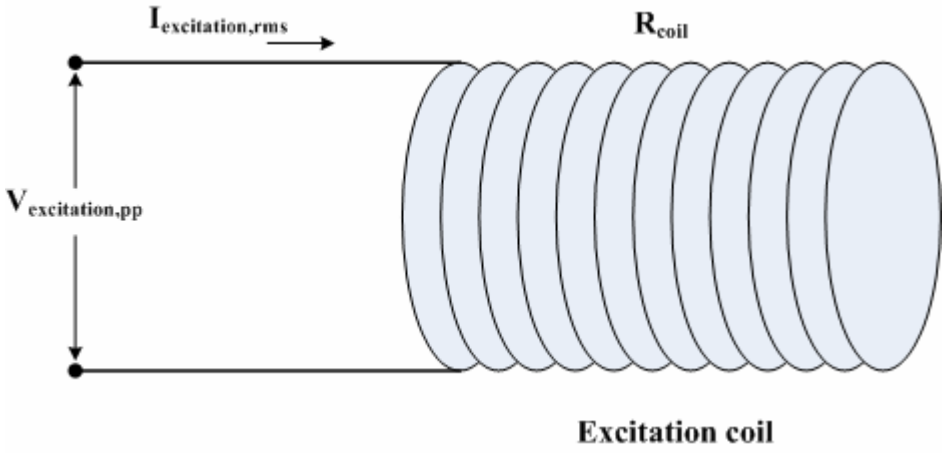

Figure 5. 12. Measurement of excitation power consumption. Electrical properties are listed in Table 5. 1.

5.4 Beam width and number of beams characterization

Mechanical dimensional parameters of the resonator, such as resonator thickness, beam length, beam width, and number of beams, are related with the sensitivity. To maximize the nonlinearity of the resonator with small oscillations, the width of beam needs to be small so that it generates more stress at a given rotational torque. However, if the width of beam is too small then the resonator might be easily broken either during the mounting of the permanent magnet or during the operation due to the vibration of the permanent magnet. This problem can be solved either by making the beam thicker or increasing the number beams. Characterization of this relationship between the width of the beam and the number of the beams to the sensitivity would give an idea for the optimum combination of those parameters.

To characterize the magnetic sensor, 3 different designs are compared (Figure 5. 13). The resonant frequency is measured every 30 rotational degree at the external magnetic fields of the Earth's magnetic field, 0.195 mT, and 0.39 mT (Figure 5. 14 – 5. 16).

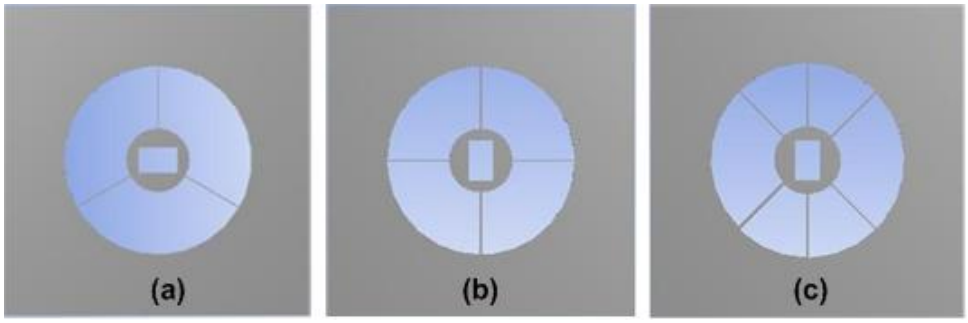

Figure 5. 13. Three different designs. (a) 3 beam structure with 18.5 μm in beam width, (b) 4 beam structure with 14.6 μm in beam width, and (c) 6 beam structure with 13.1 μm in beam width.

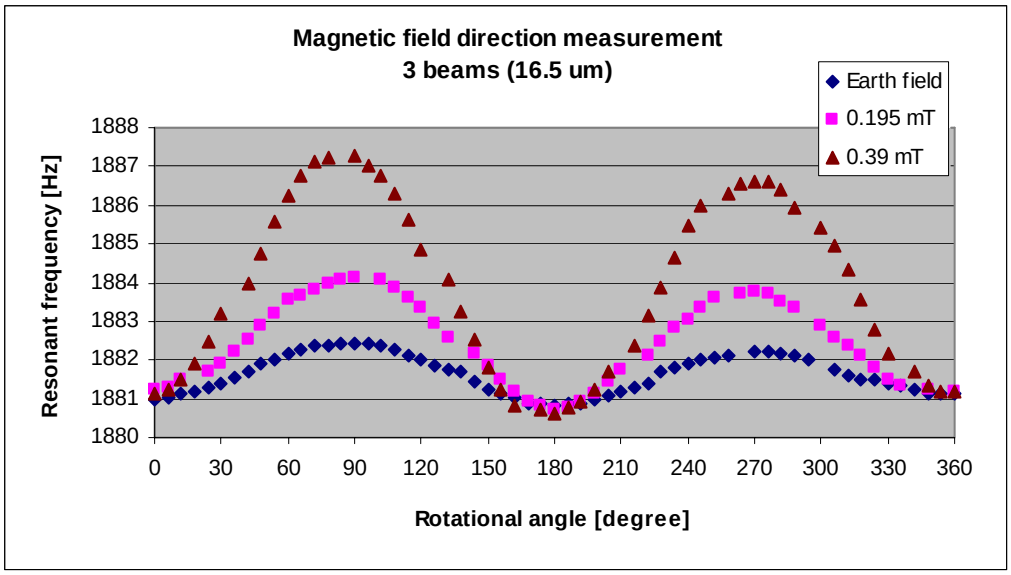

Figure 5. 14. Measurement results of the 3 beam structure.

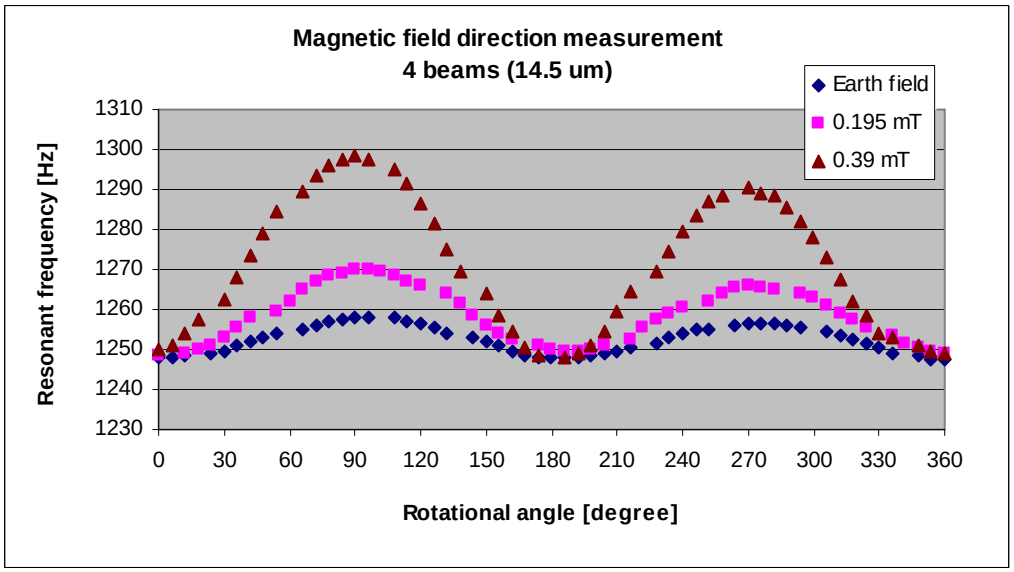

Figure 5. 15. Measurement results of the 4 beam structure.

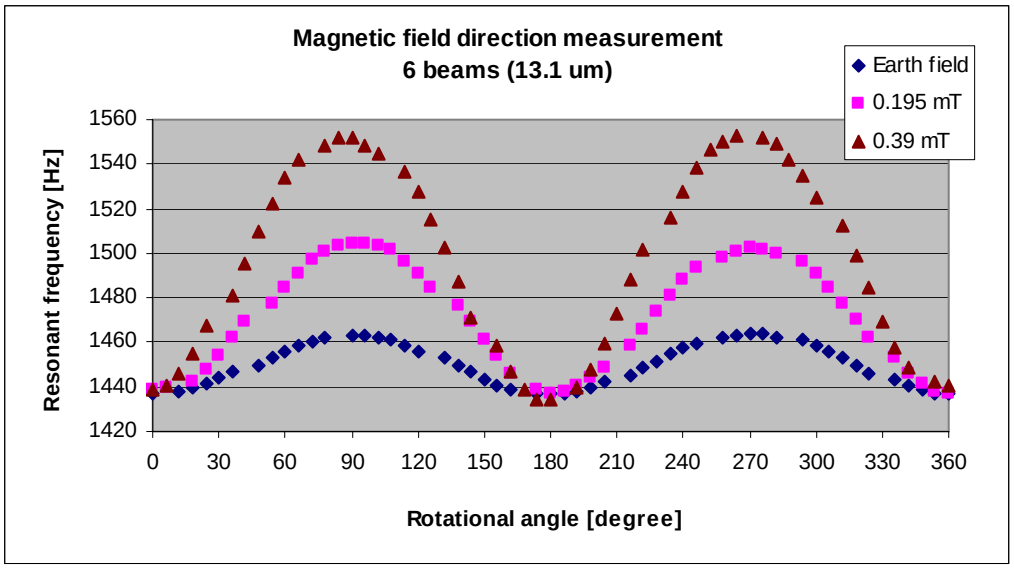

Figure 5. 16. Measurement results of the 6 beam structure.

Table. 5. 3. Comparison of the normalized sensitivity [mHz / (Hz·degree)]

N_b	w_b [μm]	Resonant frequency [Hz]	Normalized sensitivity [mHz / (Hz·degree)]		
			Earth field	0.195 mT	0.39 mT
3	18.5	1881	0.009	0.017	0.036
4	14.6	1248.25	0.086	0.192	0.431
6	13.1	1437.45	0.196	0.509	0.876

The sensitivity is normalized to its resonant frequency at $\theta = 0°$ (Table 5. 3). If the same number of beams is used, then the structure with narrow beams shows the lower resonant frequency and the higher sensitivity. However, the six beam structure shows the higher normalized sensitivity than four beam structure for every external magnetic field although the four beam structure shows the lower resonant frequency (1248.25 Hz for

four beam structure *vs*. 1437.45 Hz for six beam structure). This implies that the sensitivity increases as the beam width decreases while more beams are used to maintain the linear stiffness of the system.

5.5 Conclusions

This chapter presents a complete magnetic sensing *system* that consumes less than 200 microwatts of power in continuous operation, and is capable of sensing the Earth's magnetic field. The system is composed of a micromachined silicon resonator combined with a permanent magnet, excitation and sensing coils, and a magnetic feedback loop for the completion of the system. A total system power consumption of 138 μW and a resonator actuation voltage of $4mV_{pp}$ from the ±1.2V power supply have been demonstrated with measurement of the direction of the Earth's magnetic field. Sensitivities of 0.009, 0.086, and 0.196 [mHz/(Hz·degree)] for the Earth's magnetic field were measured for 3, 4, and 6 beam structures, respectively.

The resonance frequency is automated for data-acquisition for every second with a device revolution of 1 rpm. A driving voltage of $4mV_{pp}$ and a power consumption of 0.24 μW are measured for the excitation of the resonant sensor.

Both three and four beam structures show higher performance as the beam width decreases. Although the frequencies were not exactly matched, the six beam structure showed higher normalized performance at all the measured external magnetic fields as expected, demonstrating the beneficial effects of nonlinear maximization which is discussed in Chapter 3.

CHAPTER 6

CONCLUSIONS

MEMS-based mechanically-resonant sensors, in which the sensor resonant frequency shifts in response to the measurand, are widely utilized. Such sensors are typically operated in their linear resonant regime. However, substantial improvements in resonant sensor performance (functionally defined as change in resonant frequency per unit measurand change) was obtained by designing the sensors to operate far into their nonlinear regime [96]. This effect is illustrated through the use of a magnetically-torqued, rotationally-resonant MEMS platform. Platform structural parameters such as beam width and number of beams are parametrically varied subject to the constraint of constant small-deflection resonant frequency. Nonlinear performance improvement characterization is performed both analytically as well as with FEM simulation using ANSYS, and confirmed with measurement results.

Nonlinear effects in resonating structures was exploited to achieve high sensing performance. A disc type resonant magnetic sensor, which contains a permanent magnet and is supported by multiple microbeams, has been characterized for the nonlinear effects on sensitivity as a function of beam width and the number of beams using analytical model as well as numerical analysis. As beam width decreases, the numerical values of linear (k_l) and nonlinear (k_{nl}) spring coefficients decrease. However, k_{nl} decreases far more slowly than k_l. Therefore, the normalized performance increases as the beam width decreases for a fixed number of beams. Alternatively, when the linear stiffness is held

constant, sensor performance is maximized by increasing the nonlinearity of the resonator. Maximum sensitivity would therefore be achieved by having an infinite number of beams of vanishingly small width. However, the minimum beam width is limited due to aspect-ratio-based fabrication limitations.

Resonators of differing beam width and number, but the same nominal k_1, are fabricated and characterized at various external magnetic fields. The test structure consists of a mechanically-resonant silicon platform supported by varying numbers and geometries of silicon beams and bearing a permanent magnet. This structure has been previously demonstrated as a magnetic sensor [97]. Although the three-beam and four-beam structures were reasonably well-matched, fabrication discrepancies led to the k_1 of the six-beam structures not being exactly matched. Both three and four beam structures show higher performance as the beam width decreases. Although the frequencies were not exactly matched, the six beam structure showed higher normalized performance at all the measured external magnetic fields as expected, demonstrating the beneficial effects of nonlinear maximization.

A total system power consumption of 138 μW and a resonator actuation voltage of 4mVpp from the ±1.2V power supply were demonstrated with capability of sensing the direction of the Earth's magnetic field. The system is composed of a micromachined silicon resonator combined with a permanent magnet, excitation and sensing coils, and a magnetic feedback loop. Sensitivities of 0.009, 0.086, and 0.196 [mHz/(Hz·degree)] for the Earth's magnetic field were measured for 3, 4, and 6 beam structures, respectively. The resonance frequency is automated for data-acquisition for every second with a device

revolution of 1 rpm. A driving voltage of 4 mV_{pp} and a power consumption of 0.24 μW are measured for the excitation of the resonant sensor.

Nonlinear performance improvement characterization performed both analytically as well as with FEM simulation was confirmed with measurement result from the magnetically-torqued and rotationally-resonant MEMS platform. Characterization results provide a useful way to enhance sensing performance of the resonant-based sensors by maximizing structural nonlinearity

REFERENCES

[1] J. E. Lenz, "A review of magnetic sensors," *Proceedings of the IEEE*, vol. 78, pp. 973-989, 1990.

[2] J. Lenz and S. Edelstein, "Magnetic sensors and their applications," *Sensors Journal, IEEE*, vol. 6, pp. 631-649, 2006.

[3] J. W. Judy, H. Yang, N. Myung, P. Irazoqui-Pastor, M. Schwartz, K. Nobe, and K. Yang, "Ferromagnetic Micromechanical Magnetometers," presented at Late News, Technical Digest of Solid-State Sensor and Actuator Workshop, Hilton Head Island, 2000.

[4] R. S. Popovic, *Hall Effect Devices*, 2nd ed. Bristol, U.K.: Institute of Physics, 2004.

[5] H. H. Yang, N. V. Myung, J. Yee, D. Y. Park, B. Y. Yoo, M. Schwartz, K. Nobe, and J. W. Judy, "Ferromagnetic micromechanical magnetometer," Munich, 2002.

[6] Z. Kadar, "Integrated Resonant Magnetic Field Sensor," vol. Ph.D. Delft, Netherlands: Delft University of Technology, 1997.

[7] J. W. Judy and R. S. Muller, "Magnetic microactuation of torsional polysilicon structures," *Sensors and Actuators, A: Physical*, vol. 53, pp. 392-397, 1996.

[8] R. Sunier, T. Vancura, Y. Li, K. U. Kirstein, H. Baltes, and O. Brand, "Resonant Magnetic Field Sensor With Frequency Output," *Microelectromechanical Systems, Journal of*, vol. 15, pp. 1098-1107, 2006.

[9] V. Zieren, "Integrated silicon multicollector magnetotransistor," vol. Ph.D. Delft: Delft, 1983.

[10] M. J. Caruso and T. B. Sensors, "A New Perspective on Magnetic Field Sensing," in *Sensors*, December 1998.

[11] A. Baschirotto, E. Dallago, P. Malcovati, M. Marchesi, and G. Venchi, "A Fluxgate Magnetic Sensor: From PCB to Micro-Integrated Technology," *Instrumentation and Measurement, IEEE Transactions on*, vol. 56, pp. 25-31, 2007.

[12] M. Marchesi, A. Baschirotto, F. Borghetti, E. Dallago, P. Malcovati, E. Melissano, P. Siciliano, and G. Venchi, "Fluxgate magnetic sensor and front-end circuitry in an integrated microsystem," *Sensors and Actuators A (Physical)*, vol. 132, pp. 90-7, 2006.

[13] E. M. Billingsley and S. W. Billingsley, "Fluxgate Magnetometers," presented at Proceedings of SPIE - The International Society for Optical Engineering, Orlando, FL, United States, 2003.

[14] B. Eyre, K. S. J. Pister, and W. Kaiser, "Resonant mechanical magnetic sensor in standard CMOS," *IEEE Electron Device Letters*, vol. 19, pp. 496-8, 1998.

[15] S. M. Sze, *Semiconductor Sensors*: John Wiley & Son, Inc, 1994.

[16] M. Epstein and R. B. Schulz, "Magnetic-field pickup for low-frequency radio-interference measuring sets," *Institute of Radio Engineers Transactions on Electron Devices*, vol. ED-8, pp. 70-77, 1961.

[17] H. Blanchard, "Hall sensors with integrated magnetic flux concentrators," vol. Ph.D. Lausanne, Switzerland: EPFL, 1999.

[18] Z. B. Randjelovic, M. Kayal, R. Popovic, and H. Blanchard, "Highly sensitive Hall magnetic sensor microsystem in CMOS technology," *Solid-State Circuits, IEEE Journal of*, vol. 37, pp. 151-159, 2002.
[19] M. Schneider, R. Castagnetti, M. G. Allen, and H. Baltes, "Integrated flux concentrator improves CMOS magnetotransistors," 1995.
[20] H. Blanchard, F. de Montmollin, J. Hubin, and S. Popovic, "Highly sensitive Hall sensor in CMOS technology," Sendai, Japan, 2000.
[21] P. M. Drljaca, F. Vincent, P. A. Besse, and R. S. Popovic, "Design of planar magnetic concentrators for high sensitivity Hall devices," Munich, Germany, 2002.
[22] S. Kawahito, Y. Sasaki, H. Sato, C. Sang On, T. Nakamura, and Y. Tadokoro, "Miniature fluxgate sensing element for high-performance integrated silicon magnetic sensors," *Sensors and Materials*, vol. 5, pp. 241-51, 1994.
[23] W. Gopel, J. Hesse, and J. N. Zemel, *Sensors - A Comprehensive Survey*, vol. 5: VCH, 1989.
[24] P. Ripka, "Review of fluxgate sensors," *Sensors and Actuators, A: Physical*, vol. 33, pp. 129-141, 1992.
[25] T. M. Liakopoulos and C. H. Ahn, "A micro-fluxgate magnetic sensor using micromachined planar solenoid coils," *Sensors and Actuators A (Physical)*, vol. A77, pp. 66-72, 1999.
[26] R. Gottfried-Gottfried, W. Budde, R. Jahne, H. Kuck, B. Sauer, S. Ulbricht, and U. Wende, "A miniaturized magnetic-field sensor system consisting of a planar fluxgate sensor and a CMOS readout circuitry," *Sensors and Actuators, A: Physical*, vol. 54, pp. 443-447, 1996.
[27] O. Dezuari, E. Belloy, S. E. Gilbert, and M. A. M. Gijs, "New hybrid technology for planar fluxgate sensor fabrication," *Magnetics, IEEE Transactions on*, vol. 35, pp. 2111-2117, 1999.
[28] L. Perez, C. Aroca, P. Sanchez, E. Lopez, and M. C. Sanchez, "Planer fluxgate sensor with an electrodeposited amorphous core," *Sensors and Actuators A (Physical)*, vol. A109, pp. 208-11, 2004.
[29] S. Kawahito, C. Maier, M. Schneiher, M. Zimmermann, and H. Baltes, "A 2D CMOS microfluxgate sensor system for digital detection of weak magnetic fields," *Solid-State Circuits, IEEE Journal of*, vol. 34, pp. 1843-1851, 1999.
[30] L. Chiesi, P. Kejik, B. Janossy, and R. S. Popovic, "CMOS planar 2D micro-fluxgate sensor," *Sensors and Actuators, A: Physical*, vol. 82, pp. 174-180, 2000.
[31] J. S. Hwang, H. S. Park, D. S. Shim, K. W. Na, W. Y. Choi, and S. O. Choi, "Electronic compass using two-axis micro fluxgate sensing element," 2003.
[32] P. M. Drljaca, P. Kejik, F. Vincent, D. Piguet, F. Gueissaz, and R. S. Popovic, "Single core fully integrated CMOS micro-fluxgate magnetometer," Prague, Czech Republic, 2004.
[33] R. S. Popovic, P. M. Drljaca, and C. Schott, "Bridging the gap between AMR, GMR, and Hall magnetic sensors," 2002.
[34] A. Platif, J. Kubik, M. Vopalensky, and P. Ripka, "Precise AMR magnetometer for compass," 2003.
[35] P. Ripka, "New directions in fluxgate sensors," Balatonfured, Hungary, 2000.

[36] E. Donzier, O. Lefort, S. Spirkovitch, and F. Baillieu, "Integrated magnetic field sensor," Karlsruhe, West Germany, 1991.
[37] P. Kejik, L. Chiesi, B. Janossy, and R. S. Popovic, "New compact 2D planar fluxgate sensor with amorphous metal core," *Sensors and Actuators, A: Physical*, vol. 81, pp. 180-183, 2000.
[38] "http://www.semiconductors.philips.com/cgi-bin/pldb/pip/kmz52.html."
[39] http://www.magneticsensors.com/datasheets/hmc1051-1052.pdf.
[40] T. C. Leichle, M. Von Arx, S. Reiman, I. Zana, Y. Wenjing, and M. G. Allen, "A low-power resonant micromachined compass," *Journal of Micromechanics and Microengineering*, vol. 14, pp. 462-70, 2004.
[41] T. C. Leichle, "A micromachined resonant magnetic field sensor," in *Electrical and computer engineering*, vol. M.S. Atlanta: Georgia Institute of Technology, 2002.
[42] A. A. Seshia, W. Z. Low, S. A. Bhave, R. T. How, and S. Montaguevol, "Micromechanical Pierce Oscillator for Resonant Sensing Application," *Technical Proceedings of the 2002 International Conference on Modeling and Simulation of Microsystems*, pp. 162-165, 2002.
[43] M. W. Putty, S. C. Chang, R. T. Howe, A. L. Robinson, and K. D. Wise, "One-Port Active Polysilicon Resonant Microstructures," presented at *IEEE Proceedings of Micro Electro Mechanical Systems. An Investigation of Micro Structures, Sensors, Actuators, Machines and Robots*, 1999.
[44] C. T. C. Nguyen, "Micromechanical resonators for oscillators and filters," presented at Ultrasonics Symposium, 1995. Proceedings., 1995 IEEE 1995.
[45] G. K. Fedder, "Simulation of Microelectromechanical Systems," in *EECS*, vol. Ph.D. Berkeley: University of California at Berkeley, 1994.
[46] C. T. C. Nguyen and R. T. Howe, "CMOS micromechanical resonator oscillator," presented at Electron Devices Meeting, 1993. Technical Digest., International 1993.
[47] C. T. C. Nguyen and R. T. Howe, "An integrated CMOS micromechanical resonator high-Q oscillator," *Solid-State Circuits, IEEE Journal of*, vol. 34, pp. 440-455, 1999.
[48] S. Lee, M. U. Demirci, and C. T. C. Nguyen, "A 10-MHz micromechanical resonator Pierce reference oscillator for communications," Munich, Germany, 2001.
[49] C. Won-Youl, H. Jun-Sik, and C. Sang-On, "The microfluxgate magnetic sensor having closed magnetic path," *Sensors Journal, IEEE*, vol. 4, pp. 768-771, 2004.
[50] J. H. Seo and O. Brand, "Self-Magnetic Excitation for In-Plane Mode Resonant Microsensor," 2006.
[51] G. Genta, *Vibration of structures and machines: practical aspects*, 3rd ed. New York: Springer-Verlag, 1990.
[52] W. C. Young, *Roark's formulas for stress and strain*, 6th ed: McGraw-Hill, 1989.
[53] S. P. Timoshenko and J. M. Gere, *Mechanics of materials* 3rd ed. Boston: PWS-KENT, 1990.
[54] Frisch-Fay, *Flexible Bars*. Washington: Butterworths, 1962.

[55] J. H. Seo and O. Brand, " HIGH Q-FACTOR IN-PLANE MODE RESONANT MICROSENSOR PLATFORM FOR GASEOUS/LIQUID ENVIRONMENT," *IEEE Journal of MEMS*, pp. In press, 2007.
[56] T. Corman, K. Noren, P. Enoksson, J. Melin, and G. Stemme, ""Burst" technology with feedback-loop control for capacitive detection and electrostatic excitation of resonant silicon sensors," *Electron Devices, IEEE Transactions on*, vol. 47, pp. 2228-2235, 2000.
[57] P. S. Riehl, "Microsystems for electrostatic sensing," in *Electrical Engineering and Computer Sciences*, vol. Ph.D. Berkeley: University of California, Berkeley, 2002, pp. 110.
[58] J. C. Lotters, J. G. Bomer, A. J. Verloop, E. A. Droog, W. Olthuis, P. H. Veltink, and P. Bergveld, "Design, fabrication and characterization of a highly symmetrical capacitive triaxial accelerometer ", Chicago, IL, USA, 1998.
[59] C. Linder, E. Zimmermann, and N. F. de Rooij, "Capacitive polysilicon resonator with MOS detection circuit," Karlsruhe, West Germany, 1991.
[60] W. C. Tang, "Electrostatic comb drive for resonant sensor and actuator applications," in *EECE*, vol. Ph.D. Berkeley: University of California at Berkeley, 1990.
[61] S. D. Senturia, *Microsystem design*: Kluwer Academic Publishers, 2001.
[62] M. A. Schmidt, R. T. Howe, S. D. Senturia, and J. H. Haritonidis, "Design and calibration of a microfabricated floating-element shear-stress sensor," *Electron Devices, IEEE Transactions on*, vol. 35, pp. 750-757, 1988.
[63] M. A. Schmidt, "Microsensors for the measurement of shear forces in turbulent boundary layers," in *EECS*, vol. Ph.D. Cambridge: Massachusetts Institute of Technology, 1988.
[64] W. C. Tang, C. Tu, H. Nguyen, and R. T. Howe, "Laterally driven polysilicon resonant microstructures," *Sensors and Actuators*, vol. 20, pp. 25-32, 1989.
[65] Y. Wenjing, S. Mukherjee, and N. C. MacDonald, "Optimal shape design of an electrostatic comb drive in microelectromechanical systems," *Microelectromechanical Systems, Journal of*, vol. 7, pp. 16-26, 1998.
[66] J. D. Grade, H. Jerman, and T. W. Kenny, "Design of large deflection electrostatic actuators," *Microelectromechanical Systems, Journal of*, vol. 12, pp. 335-343, 2003.
[67] T. Hirano, T. Furuhata, K. J. Gabriel, and H. Fujita, "Design, fabrication, and operation of submicron gap comb-drive microactuators," *Microelectromechanical Systems, Journal of*, vol. 1, pp. 52-59, 1992.
[68] M. A. Schmidt, "Wafer-to-wafer bonding for microstructure formation," *Proceedings of the IEEE*, vol. 86, pp. 1575-1585, 1998.
[69] Z. Xuan Xiong and J. P. Raskin, "Low-temperature wafer bonding: a study of void formation and influence on bonding strength," *Microelectromechanical Systems, Journal of*, vol. 14, pp. 368-382, 2005.
[70] U. M. Gosele, M. Reiche, and Q. Y. Tong, "Wafer bonding: an overview," 1995.
[71] S. Bengtsson, "Semiconductor wafer bonding. A review of interfacial properties and applications," *Journal of Electronic Materials*, vol. 21, pp. 841-862, 1992.

[72] C. H. Mastragelo and C. H. Hsu, "Mechanical stability and adhesion of microstructures under capillary forces-Part I: basic theory," *Journal of Microelectromechanical Systems*, vol. 2, pp. 33-43, 1993.
[73] C. H. Mastrangelo and C. H. Hsu, "Mechanical stability and adhesion of microstructures under capillary forces-Part II: experiments," *Journal of Microelectromechanical Systems*, vol. 2, pp. 44-55, 1993.
[74] Z. Xiang, W. Dongmin, N. Fang, and S. Cheng, "Stiction problems in releasing of 3D microstructures and its solution," *Sensors and Actuators A (Physical)*, vol. 128, pp. 109-15, 2006.
[75] A. P. Lee, C. F. McConaghy, P. A. Krulevitch, E. W. Campbell, G. E. Sommargren, and J. C. Trevino, "Electrostatic comb drive for vertical actuation," Austin, TX, USA, 1997.
[76] K. J. Magnetics: http://www.kjmagnetics.com/proddetail.asp/prod=D101.
[77] A. P. French, *Vibrations and Waves*: Norton & Company, 1971.
[78] I. J. Busch-Vishniac, "The case for magnetically driven microactuators," *Sensors and Actuators A (Physical)*, vol. A33, pp. 207-20, 1992.
[79] W. P. Taylor, O. Brand, and M. G. Allen, "Fully integrated magnetically actuated micromachined relays," *Microelectromechanical Systems, Journal of*, vol. 7, pp. 181-191, 1998.
[80] E. W. Hill, A. F. Nor, J. K. Birtwistle, and M. R. Parker, "A giant magnetoresistive magnetometer," Iasi, Romania, 1997.
[81] L. Houlet, P. Helin, T. Bourouina, G. Reyne, E. Diffour-Gergam, and H. Fujita, "Movable vertical mirror arrays for optical microswitch matrixes and their electromagnetic actuation," *Selected Topics in Quantum Electronics, IEEE Journal of*, vol. 8, pp. 58-63, 2002.
[82] H. H. Gatzen, E. Obermeier, T. Kohlmeier, T. Budde, N. Ha Duong, B. Mukhopadhyay, and M. Farr, "An electromagnetically actuated bi-stable MEMS optical microswitch," 2003.
[83] I.-J. Cho, T. Song, S.-H. Baek, and E. Yoon, "A low-voltage push-pull SPDT RF MEMS switch operated by combination of electromagnetic actuation and electrostatic hold," Miami Beach, FL, United States, 2005.
[84] M. Capanu, J. G. I. Boyd, and P. J. Hesketh, "Design, fabrication, and testing of a bistable electromagnetically actuated microvalve," *Microelectromechanical Systems, Journal of*, vol. 9, pp. 181-189, 2000.
[85] L. K. Lagorce, O. Brand, and M. G. Allen, "Magnetic microactuators based on polymer magnets," *Microelectromechanical Systems, Journal of*, vol. 8, pp. 2-9, 1999.
[86] B. Wagner and W. Benecke, "Microfabricated actuator with moving permanent magnet," Nara, Jpn, 1991.
[87] B. Wagner, M. Kruetzer, and W. Beneceke, "Permanent magnet micromotors on silicon substrates," *Journal of Microelectromechanical Systems*, vol. 2, pp. 23-29, 1993.
[88] Y. Shinozawa, T. Abe, and T. Kondo, "Proportional microvalve using a bi-stable magnetic actuator," Nagoya, Jpn, 1997.

[89] T. M. Liakopoulos, W. Zhang, and C. H. Ahn, "Electroplated thick CoNiMnP permanent magnet arrays for micromachined magnetic device applications," San Diego, CA, USA, 1996.
[90] D. K. Cheng, *Field and Wave Electromagnetics*, Second ed: Addison-Wesley, 1992.
[91] R. Sunier, Y. Li, K. U. Kirstein, T. Vancura, H. Baltes, and O. Brand, "Resonant magnetic field sensor with frequency output," 2005.
[92] H. B. Oliver Brand, "Micromachined Resonant Sensors - an Overview," *Sensors Update*, vol. 4, pp. 3-51, 1998.
[93] J. H. Seo and O. Brand, "Novel high Q-factor resonant microsensor platform for chemical and biological applications," 2005.
[94] Y. Li, C. Vancura, C. Hagleitner, J. Lichtenberg, O. Brand, and H. Baltes, "Very high Q-factor in water achieved by monolithic, resonant cantilever sensor with fully integrated feedback," 2003.
[95] G. Stemme, "Resonant silicon sensors," *Journal of Micromechanics and Microengineering*, vol. 1, pp. 113-25, 1991.
[96] S. Choi, S.-H. Kim, Y.-K. Yoon, and M. G. Allen, "Exploitation of nonlinear effects for enhancement of the sensing performance of resonant sensors," presented at Transducers 2007, Lyon, France, 2007.
[97] S. Choi, S.-H. Kim, Y.-K. Yoon, and M. G. Allen, "A magnetically excited and sensed MEMS-based resonant compass," *IEEE Transactions on Magnetics*, vol. 42, pp. 3506-8, 2006.